Moist Zonally-Symmetric Models and their Applications to West African Monsoons

by

Xinyu Zheng

B.S. in Atmospheric Physics, Beijing University (1985)
M.S. in Meteorology, Chinese Academy of Sciences (1988)

Submitted to the Department of Earth, Atmospheric and Planetary Sciences
in partial fulfillment of the requirements for the degree of

Doctor of Philosophy in Meteorology

at the

MASSACHUSETTS INSTITUTE OF TECHNOLOGY

June 1997

Author . . . .
Department of Earth, Atmospheric and Planetary Sciences
March 1, 1997

Certified by . . . .
R. Alan Plumb
Professor of Meteorology
Thesis Supervisor

Certified by . . . .
Elfatih A.B. Eltahir
Assistant Professor of Hydrology
Thesis Supervisor

Accepted by . . . .

Tom H. Jordan
Department Head

Moist Zonally-Symmetric Models and their Applications to West African Monsoons

by

Xinyu Zheng

Abstract

In this thesis, we have developed several zonally-symmetric models with explicit hydrological cycles to investigate important physical processes involving "monsoon-like" circulations, based on the assumption that actual monsoons can be simplified as two-dimensional thermally-direct circulations. First, we examine the response of moist zonally-symmetric atmospheres to specified subtropical surface temperature perturbations. This is an extension of the work by Plumb and Hou (1992) to the case with moisture-dynamics feedback. We find that the inclusion of the explicit hydrological cycle does not influence the threshold behavior of the onset of thermally-direct circulations, pointed out by Plumb and Hou (1992). We also find that the steady state theory can be applied to transient surface temperature perturbations with seasonal time scales. Then, as an application, we study the sensitivity of West African monsoons to vegetation perturbations, under the condition of perpetual summer solar insolation. The numerical experiments demonstrate that West African monsoons and therefore rainfall depend critically on the location of the vegetation perturbations. While the magnitude of local rainfall is sensitive to changes in local vegetation, the location of the InTer-Convergence Zone (ITCZ) is not sensitive to changes in the vegetation northward or southward from the location of ITCZ in the control experiment. However, the location of the ITCZ is sensitive to changes of the vegetation distribution in the immediate vicinity of the location of the ITCZ in the control experiment. The study indicates that changes in vegetative cover along the border between the Sahara desert and West Africa (desertification) have a minor impact on the simulated monsoon circulation. On the other hand, the tropical African deforestation may cause the collapse of the monsoon circulation for the worst case scenario and have a dramatic impact on the West African regional rainfall. The ever-growing tropical deforestation is then likely to be another contributor to the African drought besides the well-documented sub-Saharan desertification. Finally, we examine the role of tropical Atlantic Sea Surface Temperature (SST) in the dynamics of monsoon interannual variability. We present a case study for the wettest (1994) and driest (1992) years of the 1990s so far. The observations suggest that the warm spring SST

anomaly in 1994 may be responsible for the abundant West African rainfall in 1994. This hypothesis is then explored using our numerical model. It is found that spring (April-June) SST anomalies are indeed capable of producing the observed rainfall anomaly pattern. The positive rainfall anomaly over the ocean in spring eventually propagates onto the land and persists two to three months even after the SST anomaly vanishes. The interactions between ocean, land and atmosphere are proven to be crucial for the rainfall anomaly propagation. The positive feedback between rainfall and soil moisture is responsible for sustaining the rainfall anomaly.

Thesis Supervisor: R. Alan Plumb
Title: Professor of Meteorology

Thesis Supervisor: Elfatih A.B. Eltahir
Title: Assistant Professor of Hydrology

Acknowledgments

Many people have been instrumental to the completion of this work and to my well-being during the course of the work. My thanks to all of them wholeheartedly. This set of acknowledgements only consists of a partial listing of those I would like to thank. For those I do not mention, please accept my apologies.

My thesis advisor, Alan Plumb, has provided sound guidance and support throughout. He introduced me the theories of zonally-symmetric monsoon circulations. He also allowed me to pursue my own scientific interests, make my own mistakes and develop my ability to do independent research. He shared his interests in tropical meteorology and monsoons with me. He always gave me insightful guidance when I needed. For all of those, thanks Alan. I am also indebted to my thesis co-advisor, Elfatih Eltahir, who drew my interest to West African monsoons. His passion and constant feedback were very inspirational. He also exposed me to observations, which bettered the understanding of my model results. Without his help, this thesis would not be possible. My committee member, Kerry Emanuel, not only made his convective code available but also gave me a lot of detailed technical consultation when I started building the models. Some of the "tricks" he taught me were really useful. He also impressed me very much with his philosophy of doing science. That is, one cannot understand complex systems without understanding simpler systems. His deep insights and many constructive suggestions led to great improvement of my thesis. Nilton Renno of the University of Arizona kindly gave me his radiative-convective model and patiently answered my endless questions. His help is greatly appreciated. I also want to thank my other committee members, Reginald Newell and John Marshall, for their constructive comments on validating the application of zonally-symmetric models to the study of West African monsoons, which make the thesis more self-contained.

My fellow graduate students and colleagues made my life at MIT enjoyable. Janusz Eluszkiewicz, with whom I had a lot of talk while we were sitting in front of the computers, made my work more relaxing. Will Hires, our system administrator,

responded promptly to my computer problems. My other group members, Juno Hsu, Moto Nakamura, Adam Sobel have helped in one way or another. I also enjoyed my discussion with Amy Solomon, both scientific and non-scientific. She was always ready to help (e.g., NCAR Graphics, LaTex). I am very grateful for her kindness. I also learned a lot from my former officemates Gerard Roe and Vincent Larson about the western world. They also kindly helped me to correct some errors in English. Yuanlong Hu helped me a lot in getting rainfall data and in using GrADS plotting software. Jeremy Pal is thanked for his great help in setting up *congo* and *amazonia* in such a timely fashion so that I could perform my numerous model runs on those two powerful machines. I also want to thank Guiling Wang for providing me the observational data. Jane McNabb, Tracey Stanelun and Joel Sloman have made my life a lot easier at MIT, for which I am grateful.

Finally, I thank my parents, Shuhua Han and Daowen Zheng, and sister Hong Zheng for their steadfast moral support. My father-in-law and my mother-in-law, who persuaded me to pursue my Ph.D. in the States, have helped in many ways. I appreciate their unselfish support. Above all, I would like to express my sincerest gratitude to my wife, Yu Xia, for her encouragement and tremendous patience. She also gave me our precious son Anthony, which made my life more colorful and meaningful. For all she has done for me, this thesis is dedicated to her.

<div align="right">

Xinyu Zheng

</div>

Cambridge, Massachusetts

1 March, 1997

Contents

List of Figures

12

13

15

16

17

21

22

Chapter 1

Introduction

1.1 General Remarks

Monsoons play an important role in both regional and global circulations. There have been a lot of studies on various monsoon systems, especially the Asian monsoon, the African monsoon and the Australian monsoon. Qualitatively speaking, the major driving mechanisms of monsoons have been identified as the land sea contrast, the moist processes and the earth's rotation (Webster, 1987). However, the quantitative modeling of monsoons is still a challenge. As modern computers become more and more powerful, numerical models emerge as very useful tools for understanding physical mechanisms that might be operating in real monsoons. The most sophisticated numerical models for simulating the earth's atmosphere are general circulation models (GCMs), which include all important physical processes in the atmosphere. These models can be used to study monsoon systems which are sub-systems of atmospheric general circulations. On the other hand, in order to understand some individual processes, we sometimes use simplified models — process models. These models only include a limited set of physical processes, but much more powerful for understanding particular processes. In this thesis, we have developed moist zonally-symmetric models as process models, neglecting zonal asymmetries. First, the model is used

25

to address the role of moisture-dynamics in the atmospheric response to subtropical surface temperature perturbations. Secondly, we will discuss the relevance of the zonally-symmetric models to West African monsoons and then use the models to study West African rainfall variability.

1.2 Monsoon as Thermally-Direct Circulation

1.2.1 Observations

The actual monsoon circulation has strong divergent wind components (Krishnamurti, 1971). Therefore, strong vertical motions are observed. To facilitate theoretical analysis, monsoons are often simplified as two-dimensional (latitude and height plane) thermally-direct meridional circulations. Figure 1.1 indicates the meridional cross section of meridional wind component averaged for July-September in the region of West Africa (15W-15E) in 1994 (ECMWF[1] analyzed data). The monsoon meridional cell is indeed very clear. Similar meridional cells are also observed in other monsoon regions, e.g., Asia and Australia (not shown here).

In reality monsoons involve fully three-dimensional disturbances. For example, monsoon depressions are responsible for most of the Indian rainfall whereas the West African monsoon rainfall is mainly associated with easterly waves. However, the life cycle of these synoptic disturbances is usually several days. If we are interested in longer time scale (from supra-synoptic up to seasonal time scale) monsoon variabilities, the assumption of zonal-symmetry is acceptable as long as the collective effect of zonal asymmetries is negligible for the region of interest. The assumption of zonal symmetry is better suited for the West African region than for any other regions, as we will show in Chapter 4. The reason is that the West African region does not have significant topography. This region will be the major concern of the thesis. Under

---

[1]ECMWF stands for European Centre for Medium Range Weather Forecast.
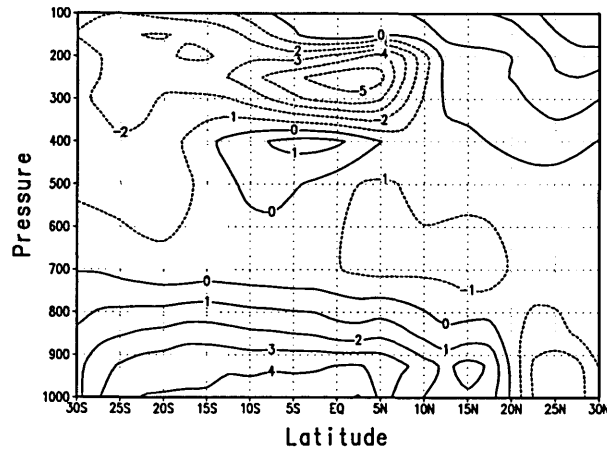
Figure 1.1: The meridional cross section of meridional wind (ms^{-1}) component, averaged through summer months (July-September) for the region of West Africa (15W-15E) in 1994, based on the ECMWF analyzed data. The contour interval is 1 ms^{-1}.

the assumption of zonal symmetry, the divergence is completely due to the meridional wind and the vorticity is solely due to the zonal wind. The strong meridional wind shown in Fig. 1.1 confirms the notion that monsoon circulations are strongly divergent and strong vertical motions are implied.

1.2.2 Previous Studies Using Two-Dimensional Models

There have been numerous mechanistic studies on monsoons, based on the assumption that the monsoon is zonally-symmetric meridional circulation.

Murakami *et al.* (1970) developed a zonally-symmetric numerical model to simulate the seasonally-averaged structure of the Asian monsoon along 80°E and with topography included. The role of the Tibetan Plateau was investigated. Without mountains, the low-level westerlies and upper level easterlies are too weak compared with those of the observations. This indicates the substantial role of the Tibetan Plateau in the Asian summer monsoon, consistent with the GCM study of Hahn and

Manabe (1975). The zonally-symmetric framework was also used by Webster and Chou (1980a) to study the role of moist processes in the Asian monsoon. Their model has two vertical layers with an interactive ocean located south of 18°N (the continental edge). The seasonally-averaged fields (such as wind, temperature, etc.) showed reasonable agreement with the observations, even though the mountains were not included. They performed four sets of numerical experiments: dry ocean, moist ocean, dry ocean-continent and moist ocean-continent. They found that only the moist ocean-continent experiment could succeed in simulating the real monsoon, suggesting that land-sea contrast and moist processes are essential for the successful simulation. The model was further used to study the low-frequency variabilities of this simple monsoon system (Webster and Chou, 1980b). Observations indicate that monsoon systems are rich in sub-seasonal variations within the relatively regular seasonal cycle. With a time scale of two weeks and sometimes longer, regions of ascending motion are observed to form to the north of the equator and propagate slowly northward across southeast Asia. The propagation appears to be associated with the "active-break sequence" of the summer monsoon which acts as a local modulator on the activity of the synoptic-scale disturbances. Only in the moist ocean-continent experiment could they get this observed monsoon quasi-biweekly active/break cycle. Webster (1983) proposed the mechanism of monsoon active/break cycle as the interaction between the components of diabatic heating and the ground hydrology. The interaction between the soil moisture and the atmosphere was found to be essential for producing the quasi-biweekly variability in his model. Xue at al. (1990) used a two-dimensional model to investigate the role of biogeophysical feedback in the African climate. The simulated temperature, humidity, and winds for July mean conditions compare reasonably well with zonally averaged, observed values in West Africa. They found that the expansion of the Sahara desert (desertification) causes the reduction of rainfall within the region of desertification.

In summary, the paradigm of zonally-symmetric monsoons provides a much sim-

pler framework for understanding important physical processes in real monsoons. While GCMs are necessary to simulate the real monsoon variabilities including synoptic events (e.g., easterly waves, monsoon depressions), GCMs are often too complicated to study processes. In fact, GCM data are as huge as the observations. In addition, even though several GCM simulations are doable in terms of the current computational resources, it is still impossible to perform too many GCM experiments. The two-dimensional models sacrifice the simulation of individual zonally-asymmetric disturbances but allow extensive exploration of the physical processes we are interested in, as long as the collective effect of those zonal asymmetries can be ignored to the first order.

1.2.3 Theories of Zonally-Symmetric Circulations

Although the tropical Hadley cell has been noted for a long time in observations (Hadley, 1735), only recently has the theoretical basis of the zonally-symmetric circulations been laid. Held and Hou (1980) proposed an idealized zonally-symmetric model of the Hadley circulation, forced by symmetric thermal forcing (to the equator). For an inviscid zonally-symmetric atmosphere on the sphere, forced by an imposed external thermal forcing (in units of temperature per unit time) $\alpha(T_e - T_0)$, where α is a relaxation rate, T_e an equilibrium temperature, and T_0 some reference background temperature, the conservation of angular momentum can be written as:

$$\frac{\partial M}{\partial t} + \frac{v}{a}\frac{\partial M}{\partial \phi} + w\frac{\partial M}{\partial z} = 0, \tag{1.1}$$

where $M = \Omega a^2 \cos^2\phi + ua\cos\phi$. The mass conservation is described as:

$$\frac{1}{a\cos\phi}\frac{\partial}{\partial \phi}(v\cos\phi) + \frac{1}{p}\frac{\partial}{\partial z}(pw) = 0. \tag{1.2}$$

The heat balance is given by:

$$\frac{\partial T}{\partial t} + \frac{v}{a}\frac{\partial T}{\partial \phi} + wS = \alpha(T_e - T). \tag{1.3}$$

Finally, from hydrostatic and gradient wind balance:

$$\frac{\partial}{\partial z}\left[2\Omega u \sin\phi + \frac{\tan\phi}{a}u^2\right] = -\frac{g}{aT_0}\frac{\partial T}{\partial \phi}. \tag{1.4}$$

Here (u, v, w) are the velocity components, p pressure, T temperature, g acceleration of gravity, Ω and a the earth's rotation rate and radius, ϕ latitude, and z log-pressure height. S is the static stability $\frac{\partial T}{\partial z} + \gamma_d$, γ_d being the dry adiabatic lapse rate.

Held and Hou (1980) pointed out that equation (1.1)-(1.4) have two steady state solutions for zero viscosity:

(i) a thermal equilibrium (TE) solution

$$T = T_e; v = w = 0;$$

with $u = u_e$, where

$$\frac{\partial}{\partial z}\left[2\Omega u_e \sin\phi + \frac{\tan\phi}{a}u_e^2\right] = -\frac{g}{aT_0}\frac{\partial T_e}{\partial \phi}; \tag{1.5}$$

(ii) an angular momentum-conserving (AMC) solution for which $T \neq T_e$, $(v, w) \neq 0$ with M constant along streamlines of the meridional flow.

The model was used to examine some basic features of the Hadley cell. They were able to derive the width of the Hadley cell, the total poleward heat flux, the latitude of upper level jets and the distribution of surface easterlies and westerlies. Their theoretical predictions were consistent with observations. Held and Hou (1980)

found that the Hadley-cell is the AMC solution of the above model. This directly follows from equation (1.1). For simplicity, at the tropopause where $w = 0$, from equation (1.1), we have $\frac{v}{a}\frac{\partial M}{\partial \phi} = 0$. Therefore, any non-zero meridional flow implies that $\frac{\partial M}{\partial \phi} = 0$. The follow-up study by Lindzen and Hou (1988) looked at the case in which the forcing centers off the equator so that there is an equilibrium temperature gradient at the equator ($\frac{\partial T_e}{\partial \phi} \neq 0$). From equation (1.4), we can see that at the equator $u \to \infty$ for this case. As a result, the TE solution is not regular and AMC solution has to be adopted. Since now the forcing T_e is asymmetric against the equator, the two Hadley cells are not identical, with the winter cell is much stronger than the summer one, as observed.

The application of the zonally-symmetric circulation theories to the monsoon-like circulation was conducted by Plumb and Hou (1992). They examined the response of an isolated subtropical thermal forcing in the zonally-symmetric atmosphere described by (1.1)-(1.4). They specified the equilibrium temperature as follows:

$$T_e(\phi, z) = \frac{\pi}{2}\Theta_e \sin\left(\pi\frac{z}{D}\right)\Phi(\phi) + T_0, \tag{1.6}$$

where

$$\Phi(\phi) = \begin{cases} \cos^2\left(\frac{\pi}{2}\frac{(\phi-\phi_0)}{\delta\phi}\right), & \mid \phi - \phi_0 \mid \leq \delta\phi, \\ 0, & \text{otherwise.} \end{cases} \tag{1.7}$$

Here Θ_e is the forcing magnitude in degrees, D the tropopause height. The forcing is centered on $\phi_0 = 25°$N and of half width $\delta\phi = 15°$. They argued that because of the finite planetary vorticity in the subtropics, the response should exhibit a threshold behavior, i.e., when the forcing magnitude is below some threshold value, no meridional circulation could occur (TE regime). On the other hand, when the forcing magnitude is above the threshold, a strong cross-equatorial meridional circulation (AMC

regime) should be expected. Based on the constraint of angular momentum at the tropopause, they derived the condition for the TE solution to be regular (regularity condition) and the threshold can be obtained from this condition:

$$-\frac{1}{2}\frac{gD}{T_0}\frac{1}{\cos\phi}\frac{\partial}{\partial\phi}\left[\frac{\cos^3\phi}{\sin\phi}\frac{\partial\hat{T}_e}{\partial\phi}\right] < 2\Omega^2 a^2\sin\phi\cos^2\phi, \qquad (1.8)$$

where

$$\hat{T}_e = \frac{1}{D}\int_0^D T_e dz.$$

Then they used a numerical model to verify their ideas. Figure 1.2 is the main result of their work. While the inclusion of numerical diffusion delays the transition from the TE regime to the AMC regime, the two regimes are very distinct.
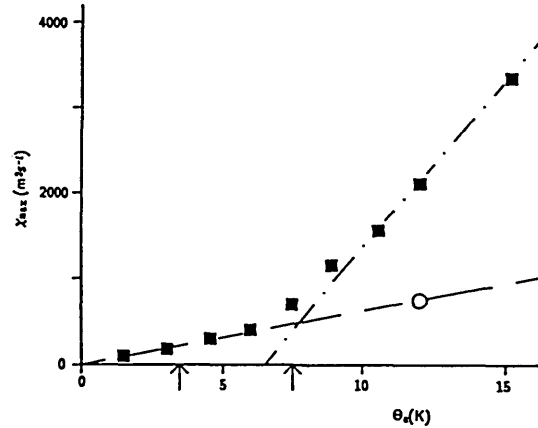
Figure 1.2: The maximum streamfunction χ_{max} (m^2s^{-1}, in latitude-height plane) against forcing magnitudes Θ_e (K), arrows indicate the theoretical (left side) and the model thresholds respectively, adopted from Plumb and Hou (1992).

The threshold behavior arises from the inertial rigidity of the system. This can be

illustrated clearly by considering the angular momentum budget at the tropopause (from eq. (1.1), note that $w = 0$) : $v\frac{\partial M}{a\partial\phi} = 0$. Note that M is related to ζ_a (absolute vorticity) by: $\zeta_a = -\frac{1}{a^2\cos\phi}\frac{\partial M}{\partial\phi}$, we then see that the absolute vorticity at the upper level is the key quantity here. When the forcing is sub-critical, the absolute vorticity at the tropopause is positive (Northern Hemisphere), the TE regime is adopted, and no meridional circulation ($v = 0$) exists. On the other hand, when the forcing is super-critical, the absolute vorticity at the tropopause is negative somewhere over the forcing region, the TE regime is not regular (see a formal mathematical proof in Plumb and Hou, 1992), a strong meridional circulation occurs ($v \neq 0$) and therefore angular momentum must be a conserved quantity at the tropopause ($\frac{\partial M}{a\partial\phi} = 0$). The work of Plumb and Hou (1992) implies that there may be a pure dynamical constraint in the real monsoon system— absolute vorticity at the upper level. Although more work has to be done in order to relate the theory to reality, we may speculate that it is this dynamical constraint that distinguishes the pre-monsoon and post-monsoon regimes.

All the above theoretical studies use dry models. In other words, no explicit hydrological cycle is included. Emanuel (1995) extended the theory of thermally-direct circulation to moist atmospheres. The dynamical constraint of the absolute vorticity at the upper level can be expressed as a constraint on the distribution of the boundary layer entropy by assuming moist neutrality above the subcloud layer. A critical profile of the boundary layer entropy was derived corresponding to zero absolute vorticity at the tropopause. The onset of the thermally-direct circulation tends to drive the boundary layer entropy to the critical profile. He also translated the constraint of the upper-level absolute vorticity to the distribution of the boundary layer entropy in three-dimensional moist atmospheres. Emanuel (1994) and Emanuel *et al.* (1994) suggested that the boundary layer entropy is the crucial quantity to look at in terms of the interaction between large-scale circulation and moist convection in moist atmospheres. Since our major concern in this thesis is about monsoons, in

which moist processes are critical, the concept of boundary layer entropy will be used throughout.

1.3 Monsoon Onset — Why Abrupt?

Most studies of monsoons are focused on Asian monsoons, especially the Indian monsoon. While the seasonal rhythm of monsoons is quite regular, there exist many sub-seasonal and supra-synoptic variabilities. During the late spring and early summer, the monsoon rainfall jumps onto the Indian continent accompanied by the sudden strengthening of surface southwesterlies within 10 to 20 days. Figure 1.3, adopted from Krishnamurti (1987), shows the area-averaged (averaged domain 10°S - 20°N, 50°E - 100°E) low-level (850mb) kinetic energies over the Arabian Sea during the summer monsoon episode of 1979. We see the rapid increase (an order of magnitude) of the rotational component and to a lesser extent the divergent part. The rainfall over the Indian continent also displays a similarly abrupt increase during the onset process. This suggests that the pre-monsoon phase and the post-monsoon phase may be in two distinct dynamical regimes.

Krishnamurti (1985) demonstrated that the large increase of low-level wind during the onset process requires the build-up of the large differential heating (mainly due to latent heat release) between land and sea. In addition, the sharp increase of kinetic energy is not limited to low-level wind, 200mb winds also show (not shown here) the similar feature, implying that the transition from the pre-monsoon regime to the post-monsoon regime is a deep phenomenon. This observational study is supported by many numerical experiments as well. In particular, Krishnamurti and Ramanathan (1982) carefully studied the sensitivity of the monsoon onset to the differential heating using the Florida State University's multi-level, grid point, primitive equation model. It is quite clear that in terms of the planetary-scale monsoons, the differential heating arising from the land-sea contrast is responsible for forcing the low-level wind
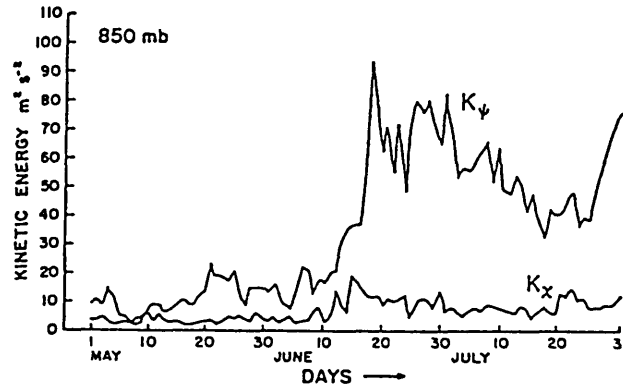
Figure 1.3: Time evolution of the area-averaged (domain 10°S-20°N, 50°E-100°E) rotational and divergent kinetic energies at 850 mb over the Arabian Sea during the 1979 summer monsoon episode, adopted from Krishnamurti and Ramanathan (1982, Fig. 3a).

strengthening over the Arabian sea.

Both the Florida State University's model and the United Kingdom Meteorological Office's model were able to capture the observed drastic increase of the low-level wind during the monsoon onset (Krishnamurti, 1987). Washington and Daggapaty (1975) were able to simulate the basic features of the African/Asian summer monsoon using the NCAR[2] GCM. Hahn and Manabe (1975) carried out the GFDL[3] GCM simulation of the Asian summer monsoon. They tried to investigate the role of the Tibetan Plateau. In particular, they found that the quite abrupt onset of the monsoon occurs only if mountains are included. However, for locations without mountains, the abrupt changes during monsoon onset are also observed. By analyzing 5-day mean cross sections of the observed zonal wind, Yeh et al. (1959) found that abrupt changes in the upper-level circulation (e.g., the jet position) occur in many regions, even away

---

[2]NCAR stands for National Center for Atmospheric Research.

[3]Geophysical Fluid Dynamics Laboratory of National Oceanic and Atmospheric Administration.

from the Asian region. The abrupt increase of rainfall and wind during the onset process were also reported for Australian monsoons (Hendon and Liebmann, 1990).

Both observational and numerical studies show that the monsoon onset is a somewhat abrupt transition from the spring to the the summer (with 10-20 day subseasonal time scale). The mechanism behind this is not clear from these studies. It appears that the mountains are not the direct cause for the abrupt changes since these abrupt changes can also occur at locations away from mountain regions. From the two-dimensional theories we described above, we know the absolute vorticity at the tropopause controls the atmospheric response to the imposed thermal forcing. The behavior of the absolute vorticity distinguishes the TE and AMC regimes. The TE regime is essentially linear while the AMC regime is nonlinear in terms of upper-level dynamics. The transition from the TE regime to the AMC regime is abrupt, as we have shown above. We may speculate that this inertial rigidity may be still operating to some extent in three-dimensional atmospheres. The Tibetan Plateau acts like an elevated heat source during summer (Murakami, 1987). In addition, the existence of mountains also enhances the latent heat release by forcing upward motions. Therefore, the inclusion of these mountains is more or less equivalent to the inclusion of an enhanced thermal forcing over Eurasia. This effect should help breaking the atmospheric inertial rigidity and the abrupt changes follow. As different locations have different inertial rigidity[4], mountains may not be necessary to produce abrupt changes. For example, Australia is much closer to the equator than the Tibetan region, the inertial rigidity in Australia is also much smaller and easier to break. In what follows, we will show some empirical evidence of this inertial rigidity, taking the Australian monsoon as an example.

---

[4]The inertial rigidity can be expressed as $f = 2\Omega\sin\phi$, the Coriolis parameter.

1.4 Some Empirical Evidence of the Dynamic Constraint

The study of Plumb and Hou (1992) points to the possible role of the dynamical constraint — absolute vorticity at the upper level in shaping the more or less abrupt onset of the observed monsoons. However, we have to keep in mind the limitations of Plumb and Hou (1992). First of all, the argument was based on the steady, dry, zonally-symmetric atmosphere. In the real atmosphere, of course, the forcing itself cannot be considered as given, because the forcing itself is a function of dynamical processes. In other words, moisture-dynamics feedback needs to be incorporated. This will be one of the goals of this thesis where we will try to relax this limitation by adding an explicit hydrological cycle. Furthermore, the exclusion of eddies in the above models could have substantial influence. Nevertheless, observations do show some support of the distinct upper-level absolute vorticity patterns between pre-monsoon and post-monsoon phases. Figure 1.4 shows the 200mb absolute vorticity averaged over the period 20 days before the onset of the Australian summer monsoon in 1991, based on the ECMWF data set. On the other hand, Fig. 1.5 is the same as Fig. 1.4 but averaged over the period 20 days after the onset of the monsoon. Focusing on the Australian region[5], we can see clearly that the post-monsoon absolute vorticity is closer to zero than that of the pre-monsoon case. A particular snapshot of the absolute vorticity at 200 mb on December 6 (Fig. 1.6, the onset time is identified as December 5) displays a clear low absolute vorticity region over Australia. In short, the constraint of the absolute vorticity, originating in two-dimensional thinkings, may be relevant to the real three-dimensional atmosphere.

---

[5]Using Darwin station as a reference, which is located at around 12°S, 120°E.
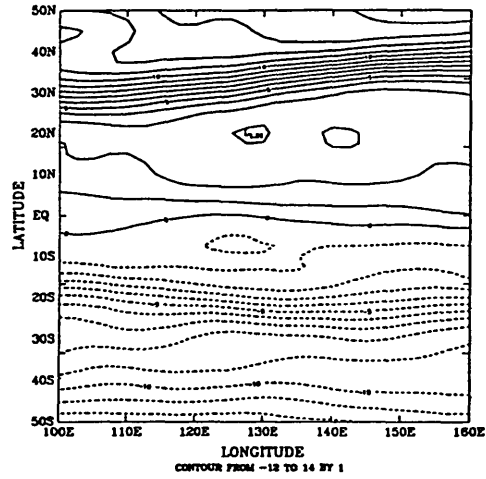
Figure 1.4: The absolute vorticity (contour interval $1 \times 10^{-5} \text{s}^{-1}$) at 200 mb averaged over the 20-day period before the onset of the Australian summer monsoon in 1991, data from ECMWF.
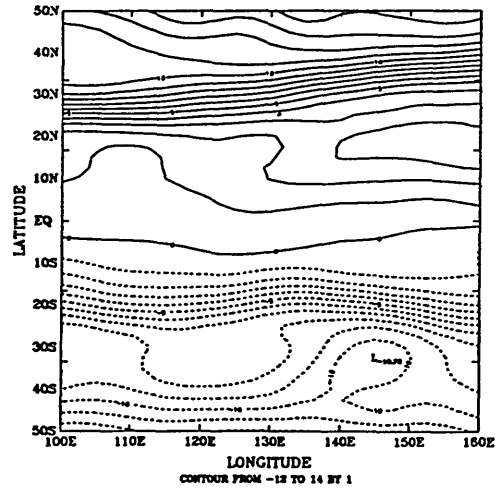
Figure 1.5: The same as Fig. 1.4 except that the averaged period is the 20-day period after the monsoon onset.
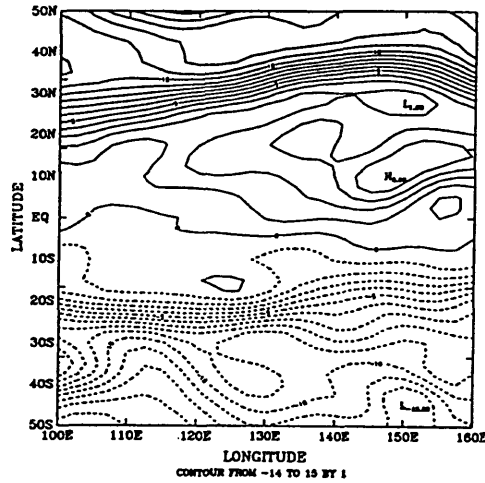
Figure 1.6: The absolute vorticity (contour interval $1 \times 10^{-5} s^{-1}$) at 200 mb on December 6, 1991 (the onset occurs on December 5, 1991), from ECMWF data.

1.5 Thesis Overview

The focus of this thesis is to develop mechanistic models that can be applicable to study "monsoon-like" circulations. We pay special attention to two aspects. The first is the inclusion of an explicit hydrological cycle, since moist processes are instrumental in real monsoon systems. The previous two-dimensional simple monsoon models such as Webster (1983) also included explicit hydrological cycles of the atmosphere. However, the representation of ensemble effect of moist convections in his model was based on the Kuo-type (Kuo, 1974) scheme which was shown to be seriously flawed by Emanuel (1994) and Emanuel et al. (1994). We use the state-of-the-art Emanuel scheme (Emanuel, 1991) to parameterize the ensemble effect of the moist convection on the large-scale circulation. Secondly, we emphasize the nonlinearity of the monsoon system, in terms of the upper-level dynamics. As indicated by the theories and observations we have discussed above, the onset of the meridional circulation is characterized by the vanishing absolute vorticity at the tropopause, which means comparable magnitudes of planetary and relative vorticities, and thus the nonlinear

advective terms are in the same order as the Coriolis terms. Therefore, at least within the context of zonally-symmetric models (with some evidence for three-dimensional atmosphere presented in Section 1.4), a nonlinear model has to be adopted. These considerations translate into two basic features of our models: primitive dynamical equations with an explicit hydrological cycle.

In Chapter 2, we will describe the model formulation. This is followed by Chapter 3 in which we investigate how the inclusion of the moisture-dynamics feedback may influence the result of Plumb and Hou (1992). In addition, our model results are compared to the theory of Emanuel (1995). The forcing for this model is the specified surface temperature perturbation. Then in Chapter 4, we discuss how zonally-symmetric models can be approximately applied to study West African monsoons. We then adapt our zonally-symmetric models to West African region and examine the sensitivity of the vegetation pattern to the West African monsoons (for perpetual summer solar forcing). The role of vegetation in the dynamics of West African monsoons is discussed. In Chapter 5, we investigate the impact of tropical Atlantic Sea Surface Temperature (SST), spring SST in particular, on the West African rainfall. Finally in Chapter 6, we summarize our main results and sketch some future research plans.

Chapter 2

Model Formulation

The common features of all the models we use in this thesis are the dynamical framework (zonally-symmetric primitive equations) and the inclusion of an explicit hydrology cycle. As we have discussed in Chapter 1, those are essential ingredients in simulating monsoons. Since the models we are going to use in each chapter are different from one another in terms of the treatment of individual physical process, we here only describe the common features of all the models. The features unique to the individual models will be described in the relevant chapters.

2.1 Model Equations

The dynamical framework of the models is based on Plumb and Hou (1992) which originates from Holton and Wehrbein (1980). The model equations are written in $z = -H ln \frac{p}{p_s}$ as the vertical coordinate and $y = asin\phi$ as the horizontal coordinate. The model equations are as follows:

$$\frac{\partial U}{\partial t} - fV = AU + DU + FU, \qquad (2.1)$$

$$\frac{\partial V}{\partial t} + fU = AV + DV + FV - \cos^2\phi\frac{\partial \Psi}{\partial y}, \qquad (2.2)$$

$$\frac{\partial T}{\partial t} + N^2 W = AT + DT + e^{-\frac{z}{2H}}\frac{R}{H}\dot{Q}_d + FT, \qquad (2.3)$$

$$\frac{\partial \Psi}{\partial z} + \frac{\Psi}{2H} = T = M_2(\Psi), \qquad (2.4)$$

$$\frac{\partial V}{\partial y} = -\left(\frac{\partial}{\partial z} - \frac{1}{2H}\right) W = -M_1(W), \qquad (2.5)$$

$$\frac{\partial Q}{\partial t} = AQ + e^{-\frac{z}{2H}}S_q + DQ + FQ, \qquad (2.6)$$

where N^2 is the squared Brunt-Väisällä frequency; H a reference scale height (we use 8 km); p_s a reference pressure normally taken as 1000 mb; R the gas constant for dry air; ϕ latitude and a the earth's radius. In addtion,

$$(U, V, W, \Psi, T, Q) = (u\cos\phi, v\cos\phi, w, \Phi, RT^*/H, q)e^{-\frac{z}{2H}}, \qquad (2.7)$$

where u, v, w, Φ, T^*, q are three components of the velocity, geopotential, temperature (deviation from some reference state) and specific humidity respectively. DU, DV, DT, DQ are diffusive terms included to suppress the numerical instabilities (Holton and Wehrbein, 1980). FU, FV represent interior sub-grid scale friction (e.g., cumulus friction, we do not include any interior momentum friction for all our models used in this thesis.) and surface momentum flux divergence. $\dot{Q}_d$ is total diabatic heating rate which consists of radiative cooling, convective heating as well as heating due to large-scale condensation. FT is surface sensible heat flux divergence. S_q is total moisture source/sink which includes effects of moist convection and large-scale condensation. FQ is the surface moisture flux divergence. The advective terms are:

$$AU = -e^{\frac{z}{2H}}\left\{\frac{\partial}{\partial y}(UV) + \frac{\partial}{\partial z}(UW)\right\}, \qquad (2.8)$$

$$AV = -e^{\frac{z}{2H}}\frac{U^2 y}{a^2\cos^2\phi}, \qquad (2.9)$$

$$AT = -e^{\frac{z}{2H}}\left\{\frac{\partial}{\partial y}(VT) + \frac{\partial}{\partial z}(WT)\right\}, \qquad (2.10)$$

$$AQ = -e^{\frac{z}{2H}} \left\{ \frac{\partial}{\partial y}(VQ) + \frac{\partial}{\partial z}(WQ) \right\}.$$ (2.11)

Note that we have neglected the advective terms in y-momentum equation (2.2) due to the smallness of those terms.

The time integration scheme follows that of Holton (1976). It is a semi-implicit scheme in which all the linear terms are treated implicitly while all the nonlinear terms are treated explicitly. This allows longer time step up to 1 hour for the dry model (Holton, 1976). The details of the model numerics can be found in Appendix A.

2.2   Physical Processes

2.2.1   Moist Convection

All the models use the same convective scheme — Emanuel scheme (Emanuel, 1991). The Emanuel scheme, which is a physically-based scheme, takes account of current available theories, observations and numerical simulations. Based on observations of inhomogeneity of individual convective clouds, the basic assumption of this scheme is that the fundamental entities are those subcloud-scale (O(100m)) updrafts and downdrafts rather than the clouds themselves. The main closure parameters are: parcel precipitation efficiency, ϵ^i , which determines the fraction of condensed water in a parcel lifted to level i that is converted to precipitation; the fraction σ_i^s of precipitation that falls through unsaturated air; and σ_d, which is the fractional area covered by the precipitating downdrafts. These represent the physical processes responsible for determining how much condensed water reevaporates, thus moistening and cooling the air, and how much falls out of the system, leading to warming and drying. Thus, this scheme directly relates the large-scale temperature and moisture tendencies to microphysical parameters. Another advantage of the scheme is that it can handle both shallow and deep convection. The scheme produces large-scale tendencies (ensemble effect of moist convections) of temperature and specific humidity by inputting

the profiles of temperature and specific humidity.

2.2.2 Diffusion

The standard diffusion used in these experiments is 4th order in the horizontal and conventional Fickian diffusion in the vertical. In some experiments, for the sake of model stability, it is helpful to use a vertically varying diffusion coefficient with larger values at lower levels. We use the form:

$$D(z) = A + Be^{-\frac{z}{H_D}}, \qquad (2.12)$$

where $D(z)$ is the diffusion coefficient, A is the value at upper levels, $A + B$ is the value at the surface $(z = 0)$, H_D is the decay scale. The values of these parameters will be mentioned when implemented in a specific model. In addition, the diffusion scheme is designed in such a way that the decay time scale of the 2-grid-length waves in the horizontal is comparable with the decay time scale of the 2-grid-length waves in the vertical. For most experiments, we choose the latter to be half the former.

2.2.3 Surface Fluxes

The surface fluxes are parameterized by the bulk aerodynamic formulae. For the momentum equations, using the same notation as above,

$$FU = e^{-\frac{z}{2H}}\cos\phi F_x, \qquad (2.13)$$

$$FV = e^{-\frac{z}{2H}}\cos\phi F_y, \qquad (2.14)$$

where

$$F_x = -g\frac{\partial \tau_x}{\partial p},$$

$$F_y = -g\frac{\partial \tau_y}{\partial p},$$

and

$$(\tau_x, \tau_y) = \rho_s C_D(u_s, v_s)V_s.$$

In the above equations, F_x, F_y are momentum flux divergence in x and y directions respectively; τ_x, τ_y surface stresses; g acceleration of gravity; p pressure; ρ_s surface air density; C_D drag coefficient; u_s and v_s surface winds in x and y directions; V_s magnitude of the surface wind, which is $\sqrt{u_s^2 + v_s^2}$.

Similarly, the sensible heat flux divergence and moisture flux divergence are given by:

$$FT = e^{-\frac{z}{2H}}\frac{R}{H}g\frac{\partial F_T}{\partial p}, \tag{2.15}$$

$$FQ = e^{-\frac{z}{2H}}g\frac{\partial F_q}{\partial p}, \tag{2.16}$$

and

$$F_T = \rho_s C_D V_s(T_s - T_1),$$

$$F_q = \rho_s C_D V_s(q_s - q_1),$$

where F_T is surface heat flux; F_q surface moisture flux; T_s surface temperature; T_1 surface air temperature; q_s surface saturation specific humidity; q_1 surface air specific humidity. Note that V_s is set to have a minimum of 5 ms^{-1}. It should be mentioned that all the flux divergences are added at the lowest model level where quantities are defined. For example, the lowest model level for u, v is $z = \frac{\Delta z}{2}$; the lowest model level for T, q is $z = 0$. Appendix A describes the details of model grid distribution.

So far, we have not defined other terms on the right hand of the model equations, namely, large-scale condensation and radiative cooling rate. This is because we treat these processes differently in different chapters. In addition, when we apply our model to West African monsoons, we have to deal with land surface processes. All these will be discussed when we come to the particular application of the model.

Chapter 3

The Response of Moist Atmospheres to Subtropical Surface Temperature Perturbations

3.1 Background

Plumb and Hou (1992, hereafter PH92) considered the response of a zonally symmetric dry atmosphere to a localized subtropical thermal forcing. Based on the inviscid steady-state theory they argued that the response to such localized subtropical forcing (the equilibrium temperature distribution has no curvature elsewhere including at the equator) displays two distinct regimes. They identified that the absolute vorticity at the tropopause is the key constraint in shaping this kind of response. Below a threshold forcing, the atmosphere adopts a steady-state of thermal equilibrium with no meridional flow; but with supercritical forcing, this thermal equilibrium state breaks down, and the atmosphere switches to a regime with a strong meridional circulation. This supercritical regime is characterized by zero absolute vorticity at upper levels,

47

and correspondingly, it is the angular momentum conserving regime pointed out by some earlier papers regarding tropical Hadley cells (e.g., Schneider and Lindzen, 1977; Held and Hou, 1980). The constraint of absolute vorticity allows PH92 to estimate the theoretical threshold for a given thermal equilibrium state, from equation (1.8). PH92 also developed a numerical model to verify their theory. Although the model viscosity shifts the threshold and modifies the response, the threshold behavior is clear in the model response as shown in Figure 1.2. This can be explained by the constraint of absolute vorticity at the tropopause. In the subtropics, the planetary vorticity is finite. If the forcing is too weak, the upper-level absolute vorticity is dominated by the planetary component and the thermal equilibrium solution is regular, and there is no meridional circulation. Only if the forcing is strong enough for the induced anticyclonic relative vorticity over the forcing region to cancel the planetary vorticity can a meridional circulation exist.

The obvious application of PH92 is to monsoonal flows. However, PH92 neglected many potentially important processes in the real monsoon onset, in particular, the moist processes. The thermal forcing in reality cannot be considered as given. In fact, it is influenced by the circulation. Recently, Emanuel (1995) extended the dry theory of PH92 to moist atmospheres, as we have reviewed in Section 1.2.3. It is our intention here to address how the inclusion of moisture-dynamics feedback might influence the threshold behavior predicted by the dry model (PH92) and to check the prediction of Emanuel (1995).

3.2   Regularity Condition and Critical State for Moist Atmospheres

The regularity condition of the thermal equilibrium state for moist atmospheres was derived by Emanuel (1995), again based on the constraint of absolute vorticity at upper levels. In the Northern Hemisphere, this condition for an atmosphere in moist

radiative-convective equilibrium (thermal equilibrium) is the satisfaction everywhere of the following inequality:

$$2\Omega^2 a^2 \sin\phi\cos^2\phi + \frac{1}{2}\frac{1}{\cos\phi}\frac{\partial}{\partial\phi}\left[\frac{\cos^3\phi}{\sin\phi}\frac{\partial s^*}{\partial\phi}(T_s - T_t)\right] > 0, \qquad (3.1)$$

where ϕ is latitude, Ω planetary rotation rate, a radius of the earth, T_s surface air temperature, T_t tropopause temperature and s^* saturation moist entropy. Condition (3.1) is similar to the result of PH92 (eq. (1.8)) except that it is expressed in terms of moist variables. The basic assumption in deriving this is to assume moist neutrality above the subcloud layer, i.e., height independence of the saturation moist saturation entropy s^* (neglecting water substance on density). In what follows, the threshold estimated from condition (3.1) will be compared with our model results.

Furthermore, a critical state was defined by Emanuel (1995) by demanding zero absolute vorticity everywhere at the tropopause. Note that the left hand side of (3.1) is proportional to the absolute vorticity at the tropopause (see Emanuel (1995) for details), so the critical value of moist entropy is determined by replacing the inequality in (3.1) byan equality. In addition, it was assumed that the saturation moist entropy in the free atmosphere is close to the actual subcloud layer entropy; then the critical subcloud layer entropy expressed by the equivalent potential temperature (θ_{eb}) can be obtained (equation (11) in Emanuel (1995)):

$$\theta_{eb} = \theta_{em}exp\left[-\chi\frac{(\cos^2\phi_m - \cos^2\phi)^2}{\cos^2\phi}\right], \qquad (3.2)$$

where

$$\chi = \frac{\Omega^2 a^2}{2C_p(T_s - T_t)},$$

in which ϕ_m is the latitude at which θ_{eb} has its maximum value θ_{em} and C_p the air heat capacity at constant pressure. This critical distribution of θ_{eb} will be compared with our model results.

3.3 Estimate of Threshold

3.3.1 Some Model Details

The model framework has been discussed in Chapter 2. Here we present some specifics of the model we use in this chapter.

The model domain is global horizontally and extends from 0 to 20 km (log-pressure) vertically. The time step for most experiments is 10 minutes. The grid points are evenly spaced in sine latitude horizontally with 30 increments and also equally spaced vertically with 20 increments (1 km vertical resolution).

The ensemble effect of moist convection is parameterized by the Emanuel scheme, as discussed in Chapter 2. We use the standard version 2.01.

In order to eliminate supersaturation in the model atmosphere, large-scale condensation is included. The large-scale condensation scheme is designed to relax specific humidity back to some suitable saturation value whenever supersaturation happens in the atmosphere, irrespective of the column stability and the large scale environment:

$$\left(\frac{\partial T}{\partial t}\right)_{lsc} = \frac{\alpha_q}{2} \frac{L_v}{C_{pd}(1-q) + qC_{pv}}(q - r_c q_s + \mid q - r_c q_s \mid),$$

$$\left(\frac{\partial q}{\partial t}\right)_{lsc} = -\frac{\alpha_q}{2}(q - r_c q_s + \mid q - r_c q_s \mid),$$

where r_c is the critical relative humidity value for condensation, which we take as 0.95. q_s is saturation specific humidity, q specific humidity, T temperature, and t time. L_v

is latent heat of vaporization and C_{pv}, C_{pd} are heat capacities of water vapor and dry air respectively. α_q^{-1} is the relaxation time scale taken as 10 times as the time step. The simplest Newtonian cooling radiative parameterization is used here, i.e.,

$$\left(\frac{\partial T}{\partial t}\right)_{rad} = -\alpha(T - T_e),$$

where we take T_e to be the constant stratospheric temperature (200.0K). This allows internal determination of the tropopause. Although this may not be able to give us the correct vertical gradient of radiative cooling, we believe this is not important because our major concern here is the interaction between dynamics and moist convection. The relaxation time scale $\alpha^{-1} = 30$ days.

Surface fluxes are parameterized by the bulk aerodynamic formulae as detailed in Chapter 2. We fix the surface wind at 5.0 ms^{-1} for all experiments (so no wind-flux feedback is included) and the drag coefficient is taken as $C_D = 1.0 \times 10^{-3}$ everywhere.

The diffusion scheme has been described in Chapter 2. We reinterate here: $D(z) = A + B exp(-z/H_D)$; where $D(z)$ is the diffusion coefficient, A is the value at infinity, $A + B$ the value at the surface $(z = 0)$, H_D is the decay length scale. The standard values are: $A = 5.00$ m^{2}s^{-1}, $B = 20.0$ m^{2}s^{-1}, $H_D = 3$ km. These values were used for all numerical experiments described in this chapter. To avoid supersaturation, the perturbations of temperature and specific humidity (with respect to some reference states) are diffused (Emanuel, personal communication).

The model is forced by a specified surface temperature distribution. Our intent here is to investigate how the moisture-dynamics feedback may influence the results of PH92, therefore, no explicit land-sea contrast is included in this model. Subtropical surface temperature perturbations are specified to mimic the real monsoon differential heating between land and sea in summer. The surface is assumed to be moist so that the evaporation always achieves its potential value.

3.3.2 Theoretical Threshold

In this section, we try to estimate the threshold from the regularity condition (3.1). A surface temperature perturbation is imposed in the northern subtropics to mimic the surface temperature perturbation during the summer monsoon episode. The standard temperature distribution is given by:

$$T_s = \begin{cases} 290.0 + T_{max}\cos^2\left[\frac{\pi}{2}(\frac{\phi-\phi_0}{\Delta\phi})\right] & \text{if } \mid \phi - \phi_0 \mid \leq \Delta\phi, \\ 290.0 & \text{otherwise,} \end{cases} \tag{3.3}$$

where we take $\phi_0 = 25°$ and $\Delta\phi = 15°$. T_{max} is the forcing magnitude.

Note that for simplicity, we have deliberately not imposed any equatorial forcing, i.e., no surface temperature gradient and curvature at the equator, the background is uniformly 290.0K. This is because from Lindzen and Hou (1988), we know that any gradient across the equator will induce thermally-direct circulations.

What we need to know in order to solve for the threshold is the radiative-convective equilibrium state corresponding to the above given surface temperature distribution (this gives us the s^* in (3.1)). In other words, the radiative-convective equilibrium state has to be determined by the surface temperature distribution. We have done a total of 81 one-dimensional radiative-convective equilibrium calculations for surface temperatures ranging from 260.0K up to 300.0K with 0.5K interval. In estimating the threshold, the actual s^* is interpolated from the above-defined column-by-column radiative-convective equilibria. It is worth mentioning that for all these one-dimensional calculations there is nearly no viscosity. This allows direct comparison between the theoretically derived threshold based on (3.1) and the results from two-dimensional calculations. The discrepancy between them will be attributed to the approximations in deriving (3.1) and the inclusion of viscosity in the two-dimensional calculations.

Figure 3.1 shows typical equilibrium vertical profiles of moist entropy and equivalent potential temperature for a one-dimensional moist radiative-convective atmo-

sphere at surface temperature of 300.0K. For the calculation of entropy and equivalent potential temperature, we have neglected the effect of water substance on the density for consistency with the derivation of the regularity condition (3.1). As we can see, the saturation entropy is nearly constant with height above the subcloud layer ($\sim$ 1km), implying a nearly moist neutral state, so the moist neutrality assumption in deriving (3.1) is fairly reasonable in our model.
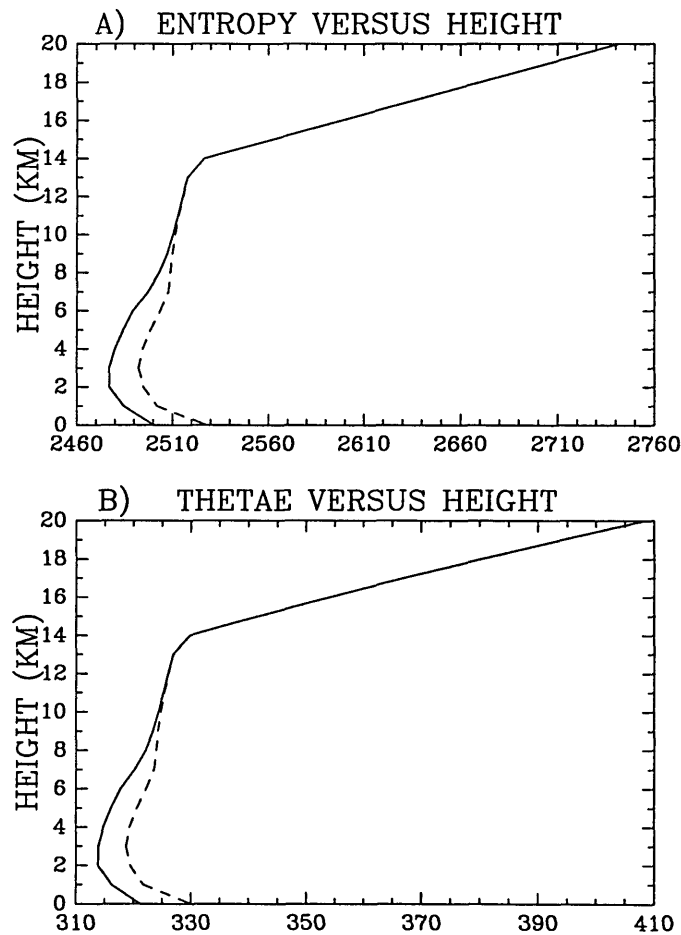
Figure 3.1: The vertical profiles of (a) moist entropies ($JK^{-1}kg^{-1}$) and (b) equivalent potential temperatures (K) θ_e and θ_{es}. In each plot, solid curve is the actual value, dashed the saturation value.

With the standard surface temperature distribution given by (3.3), the threshold $T_{max} = 2.4K$. This shows that the threshold can be easily attained in practice.

It should be noted that the inclusion of a background, broad-scale tropical distribution of surface temperature does not change the threshold very much. For example, if we adopt a symmetric (about the equator) distribution as follows:

$$T_s = \begin{cases} 300.0 - 40.0\sin^2\phi + T_{max}\cos^2\left[\frac{\pi}{2}(\frac{\phi-\phi_0}{\Delta\phi})\right] & \text{if } |\ \phi - \phi_0\ | \le \Delta\phi, \\ 300.0 - 40.0\sin^2\phi & \text{otherwise,} \end{cases} \quad (3.4)$$

we find the threshold to be around 2.7K.

3.4 Experiments and Results

Here we present two sets of numerical experiments. The first set comprises steady-state experiments where the surface temperature perturbation in the subtropics is invariant with time, either in the form of (3.3) (referred to as "without equatorial forcing" since there is no curvature at the equator) or in the form of (3.4) (referred to as "with equatorial forcing"). We have performed a series of numerical experiments for each form of the surface temperature distribution. We take various magnitudes of the surface temperature maximum (T_{max}). For each value of T_{max}, the model is integrated long enough to achieve a quasi-steady state. The second set of experiments comprises unsteady cases in which the surface temperature is allowed to vary with time. Since all the arguments about threshold behavior stem from the steady-state assumption, we want to check to what extent the theory can be applied to cases with time-varying surface temperature perturbation.

3.4.1 Steady Case without Equatorial Forcing

This is the case that PH92 considered but with the dry model. The surface temperature distribution is given by (3.3). We have conducted 10 calculations with T_{max} ranging from 1.5K to 15.0K by 1.5K increments. The initial condition is the radiative-

convective equilibrium state at the uniform background surface temperature 290.0K calculated from the one-dimensional integration (using the same model, but only two increments in the horizontal and set the surface temperature constant). For each value of T_{max}, the model is integrated for 200 days, reaching a quasi-steady state (it may take longer for some cases). The equilibrated maximum streamfunction (defined as the average of the last 25 days) versus the forcing magnitude (T_{max}) is shown in Figure 3.2.
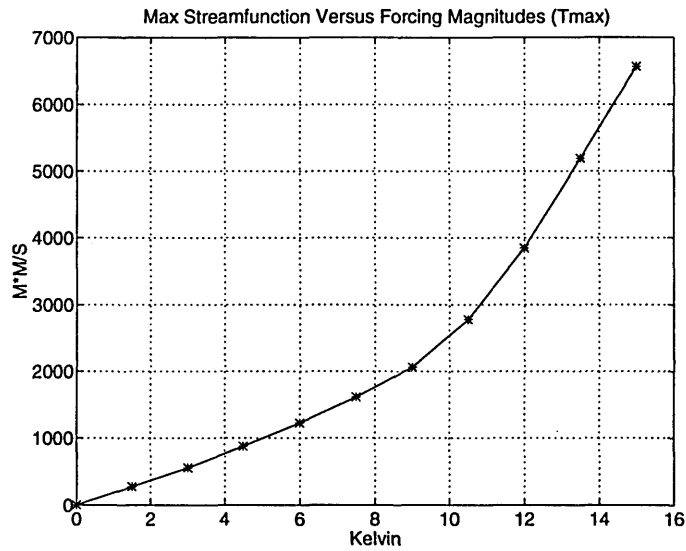
Figure 3.2: The equilibrated maximum streamfunction against the forcing magnitude (T_{max}) of the surface temperature perturbation: steady case without equatorial forcing (localized).

The inviscid theory predicts that below the threshold (which is around 2.4K by Section 3.3.2), no meridional circulation occurs. The inclusion of viscosity in our two-dimensional runs will necessarily drive a meridional circulation no matter how small the forcing is, as pointed out by Schneider and Lindzen (1977). Therefore, as discussed in PH92, the transition from the subcritical to the supercritical regime in the model is delayed and is less abrupt than that predicted by the theory. However, from Figure 3.2 we still can detect the two distinct regimes (in terms of the slope of the plot of the maximum streamfunction versus the forcing magnitude). The threshold is

around 9.0K instead of 2.4K by the theory. The inclusion of the viscosity increases the threshold; another set of experiments has been done to support this point. This set of the experiments is identical with the standard one except the diffusion coefficient is halved (not shown here). The decrease of the diffusion indeed makes the threshold smaller and the transition more abrupt. The model threshold, although it is different from the inviscid theory, corresponds closely to the forcing magnitude that makes the absolute vorticity zero, based on the linear viscosity-driven circulation. For example, $T_{max} = 4.5K$ is clearly in the linear regime from Figure 3.2 , so the circulation is mainly viscosity driven. This forcing produces a minimum of $\zeta_a \sim 2.92 \times 10^{-5}$ s^{-1} at around 25°N (not shown here). In other words, for $T_{max} = 4.5K$, $-\frac{\zeta_r}{f}$ (ζ_r denotes relative vorticity) has a maximum of 0.5249. Therefore, the forcing magnitude which makes $-\frac{\zeta_r}{f} = 1$ (equivalent to $\zeta_a = 0$) at the tropopause is simply 4.5/0.5249 $\sim$ 8.6K which is very close to 9.0K shown in Figure 3.2.

A typical supercritical response is shown by Figure 3.3, for $T_{max} = 15.0K$. While the subtropical forcing is localized, for the typical supercritical regime the response is global, i.e., the circulation is nonlocal and cross-equatorial (Fig. 3.3a), similar to PH92. Note that the onset of the strong global meridional circulation effectively creates very weak absolute vorticity (Fig. 3.3d) near the tropopause. In other words, the flow is indeed nearly in the angular momentum conserving (AMC) regime at upper levels (Fig. 3.3c). The apparent nonconservation of angular momentum at equatorial upper levels is clearly an indication of the inclusion of viscosity in our model. Note in particular that there is a tendency for the flow to follow the angular momentum surfaces over the equator even in the lower and middle troposphere. This induces two downward motion regions for the given temperature perturbation (Fig. 3.3e). Namely, one downdraft occurs at the same side of the equator as the forcing while the other occurs at the other side of the equator. There is a weak updraft between the two downdrafts.

The critical state (3.2) predicted by Emanuel (1995) is compared with our model
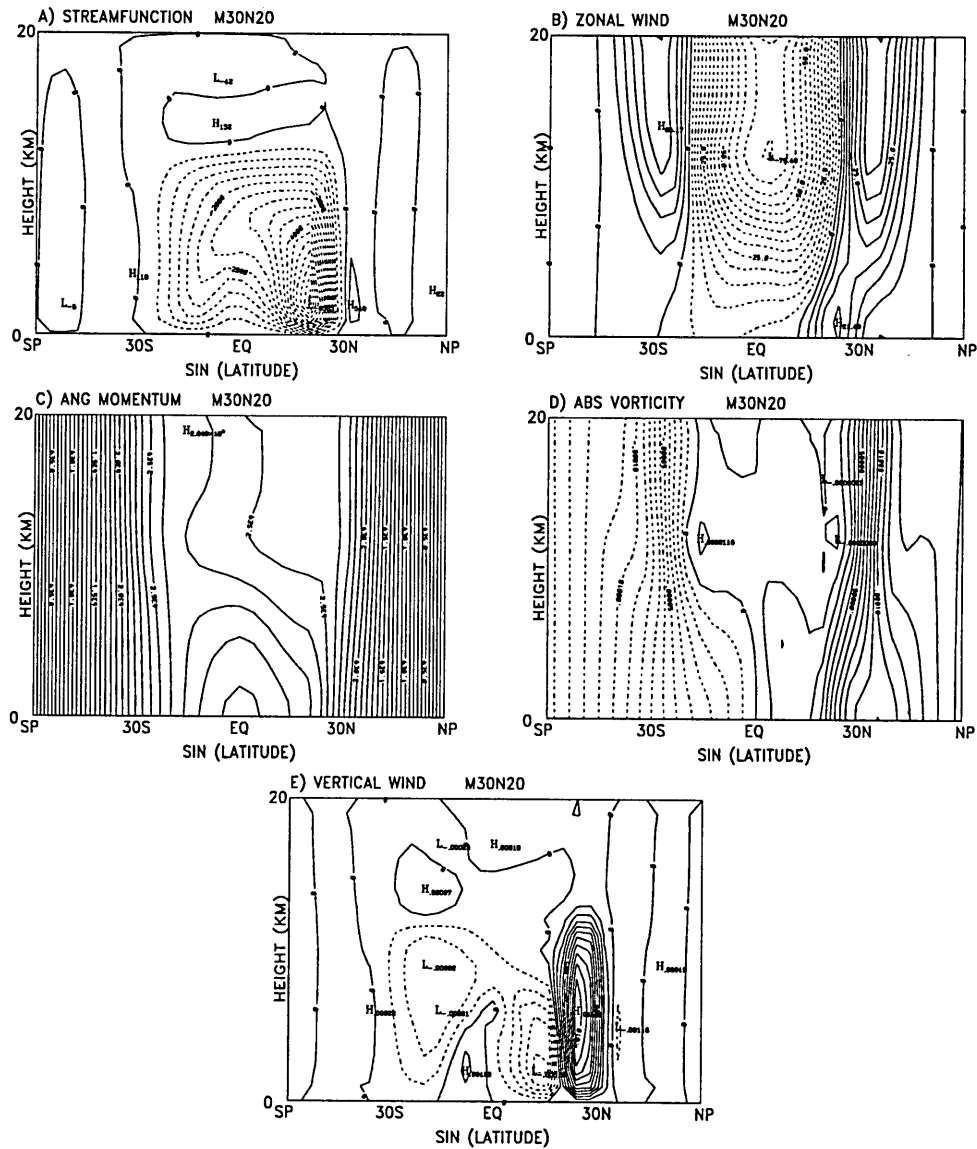
Figure 3.3: A typical supercritical regime, standard parameters, $T_{max} = 15.0$K: (a) streamfunction (contour interval 1×10^3 m^{2}s^{-1}), (b) zonal wind (contour interval 10 ms^{-1}), (c) angular momentum (contour interval 1×10^9 m^{2}s^{-1}), (d) absolute vorticity (contour interval 1×10^{-4} s^{-1}) and (e) vertical velocity (contour interval 1×10^{-3} ms^{-1}).

equilibrated state for the above typical supercritical regime (Fig. 3.4). Also plotted in Fig. 3.4 is the thermal equilibrium solution (of course it is not regular in this case). While the thermal equilibrium state for this magnitude of the perturbation $T_{max} = 15.0\text{K}$ is well above the threshold, the onset of the global meridional circulation produces a surface entropy distribution which is not far away from the theoretical value given by (3.2) within the meridional circulation, indicating that the assumptions made in deriving the critical value of θ_e are not unreasonable. This also confirms the scale analysis by Emanuel (1995) where it was argued that the onset of the thermally-direct cell effectively suppresses the supercriticality so that the equilibrium subcloud layer entropy should not be too different from its critical value. Note that the relatively larger deviation of the surface entropy compared with the critical value in the subsidence region (see Fig. 3.3e) may be due to the decoupling between the subcloud layer and the free atmosphere.
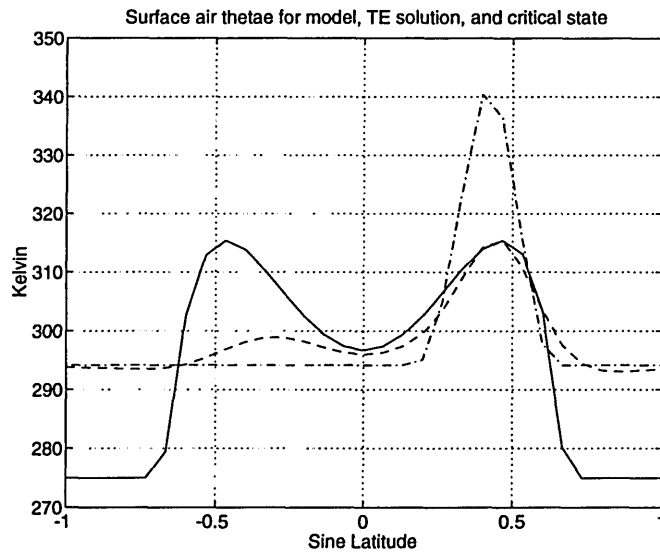
Figure 3.4: Comparison among model equilibrium surface θ_e (dashed), thermal equilibrium solution (TE, dashed-dotted) and the critical curve (solid) calculated by (3.2). This is the same case as Fig. 3.3. Note that for the critical curve, all values below 275.0K are set to 275.0K for better comparison.

In short, the inclusion of moisture-dynamics feedback does not change the quali-

tative features of the response to a localized subtropical forcing. The reason for this
is that the threshold arises from the *pure* dynamical rigidity (upper level absolute
vorticity) of the system, as we mentioned before. The response of a moist zonally
symmetric atmosphere to a localized subtropical temperature perturbation, like the
dry counterpart addressed by PH92, displays two clear distinct regimes. The subcrit-
ical regime is basically in radiative-convective equilibrium. The supercritical regime
is the AMC one as predicted by the theory.

3.4.2 Steady Cases with Equatorial Forcing

The existence of the equatorial forcing given by (3.4) will necessarily drive a symmetric
Hadley circulation, as addressed by many previous works (e.g., Schneider and Lindzen,
1977; Held and Hou, 1980). The onset of the Hadley circulation will create a more or
less zero absolute vorticity region at upper levels. If the subtropical forcing is within
this region, the dynamical rigidity (upper level absolute vorticity) of the system may
be influenced. We conduct this set of experiments to check how the constraint of the
upper level dynamical rigidity works under these circumstances.

Two sets of experiments have been done. First, we essentially do the same thing as
in Section 3.4.1 but with the surface temperature distribution given by (3.4). Second,
in order to put the forcing inside the Hadley cell, we deliberately halve the rotation
rate so that the Hadley cell is much broader. Again, the model is integrated up to 200
days to a quasi-steady state for each value of T_{max}. For the first set of experiments,
the magnitudes range from 1.5K up to 15K with 1.5K increments; For the second set
of experiments the magnitudes range from 3.0K to 15K with 3.0K interval.

Figure 3.5 shows the maximum streamfunction against the forcing magnitude for
the first case and Figure 3.6 for the second. Referring to Figure 3.5, in this case, the
maximum forcing is located near the northern edge of the preexisting zero absolute
vorticity region due to the Hadley cell; the dynamical rigidity is still there. Therefore,
it is not surprising that the dependence of maximum streamfunction against the

Max Streamfunction Versus Forcing Magnitudes (Tmax)
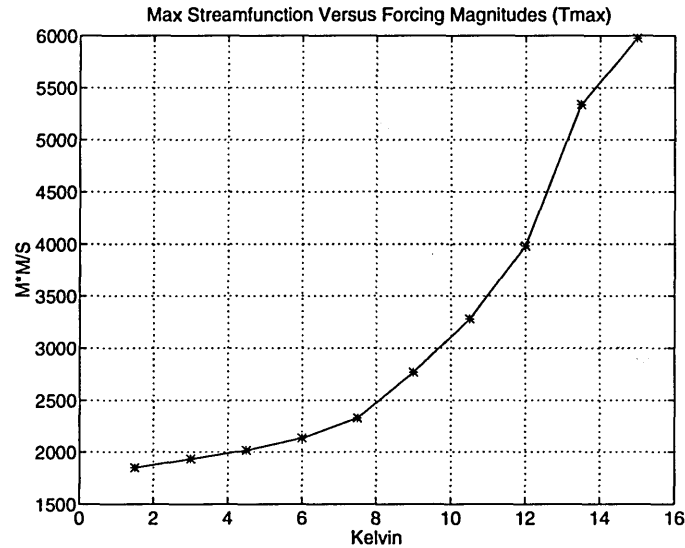
Figure 3.5: The equilibrated maximum streamfunction against the forcing magnitude (T_{max}) of the surface temperature perturbation: steady case with equatorial forcing, normal rotation rate.

forcing magnitudes shows similar features as cases without equatorial forcing, despite some quantitative differences. The transition seems to be from 6.0K to 7.5K but not as clear as the localized surface temperature perturbation cases discussed in Section 3.4.1 (Fig. 3.2). As for Figure 3.6, the dependence of the maximum streamfunction against the forcing magnitude also displays a clear transition from one regime (weak forcing) to another regime (strong forcing) in terms of the slope of the curve, surprisingly at first thought because the forcing now is located within the preexisting zero absolute vorticity region produced by the Hadley cell. This can be understood as follows: for the second case above, even though there is a preexisting zero absolute vorticity at upper levels, as the subtropical forcing gets stronger, it will necessarily produce a strong anticyclonic vorticity at upper levels over the forcing region, the total absolute vorticity now is substantially negative there and away from zero, only a modification of the strong thermally-direct circulation can bring the negative absolute vorticity back to zero. This is the state that the dynamical system has to reach whenever the thermally-direct circulation is present.
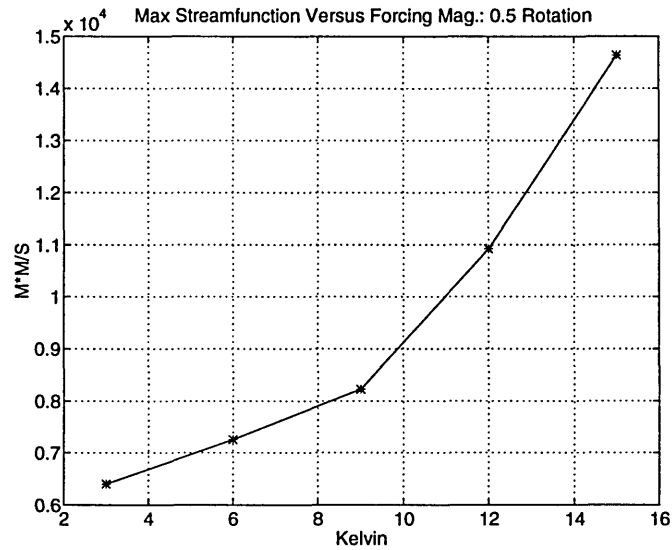
Figure 3.6: The same as Fig. 3.5 except the rotation rate is halved.

In this section, the original idea of the transition from the thermal equilibrium state to AMC regime has been extended. We have seen that a preexisting Hadley cell does not change the qualitative features of the response of a given subtropical temperature perturbation. The relation between the maximum streamfunction and the forcing magnitude always displays similar nonlinear features, as compared with the localized forcing case (Section 3.4.1). Again, the dynamical rigidity of the system plays a key role in shaping this nonlinear behavior.

3.4.3   Unsteady Cases

In this section, we try to extend our numerical experiments to time-varying surface temperature cases. Since all the above discussion is based on steady states, it is necessary to see to what extent the steady-state theory can be applied to the time-varying onset of the meridional circulation. The surface temperature here is specified the same as (3.3) or (3.4) except that the perturbation part has a time-varying factor which tends to mimic the seasonal temperature variation in the subtropics. The time

factor $GT(t)$ is expressed as:

$$GT(t) = \begin{cases} \mid \sin(\frac{\pi t}{T}) \mid & \text{if } 0 \leq t \leq T, \\ 0.0 & \text{if } T < t < 2T, \end{cases} \tag{3.5}$$

where $T = 180$ days (about half a year).

For $T \geq 2T$, GT is defined as a periodic function with period $2T$, i.e., $GT(t+2T) = GT(t)$. An example of the latitude time surface temperature distribution is given by Figure 3.7, for $T_{max} = 15.0$K.
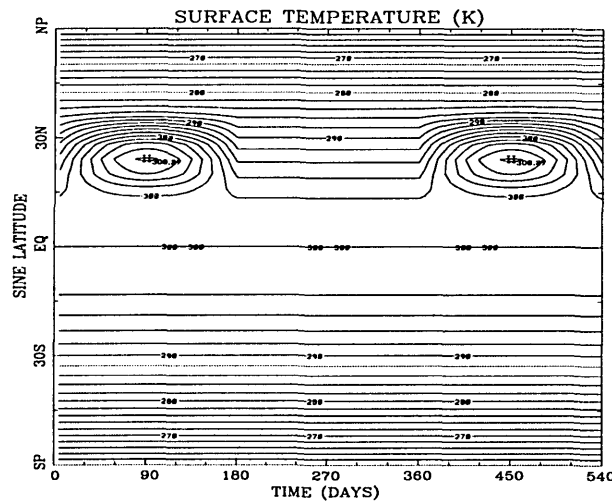
Figure 3.7: Time (day) — Sine Latitude plot of the specified surface temperature used in unsteady case with symmetric temperature background (contour interval 2.0K): $T_{max} = 15$K.

The model starts from column-by-column radiative-convective equilibrium corresponding to either the background symmetric surface temperature distribution (3.4). or the flat background 290.0K. The model is integrated up to 540 days (about one and a half years) in all the following experiments.

Figure 3.8 shows the case $T_{max} = 18.0$K under the situation without equatorial forcing. Figure 3.8a shows the streamfunction at 3km (where the streamfunction

more or less achieves its maximum magnitude). The onset of the cross-equatorial meridional circulation is very clear at around 60-70 days and repeated at around 420-430 days with very little difference. Consistent with this, the convective precipitation (Fig. 3.8b) and surface wind (Fig. 3.8c) also show sharp increases with time at the latitude (25°) of maximum surface temperature. The very strong surface wind (compared with observations) is not surprising because of the two-dimensionality of the model. In terms of the upper level dynamics, the onset of the strong meridional circulation coincides with weakening of the upper level absolute vorticity (Fig. 3.8d). This case is clearly similar to the supercritical regime (AMC regime) we have discussed in Section 3.4.1 for the steady case.

If we decrease the forcing to $T_{max} = 5.0K$, the results are shown in Figure 3.9, we cannot see any sign of cross-equatorial meridional circulation. The time variation of convective precipitation (Fig. 3.9a) almost follows the specified time variation of the surface temperature and no sharp increase with time is observed. Consistent with this, the upper level absolute vorticity is not close to zero, and the planetary component is still dominant (Fig. 3.9b) indicating that this case is still in the linear viscous regime in terms of upper level dynamics. The convective precipitation minimum (Fig. 3.9a) south of the forcing indicates the existence of a meridional circulation, which is clearly viscosity driven.

Furthermore, similar to steady-state cases, the inclusion of equatorial forcing will not influence the qualitative features of the response. Figure 3.10 describes the unsteady case identical to Figure 3.8 except for the inclusion of a symmetric background temperature defined by (3.4) (the surface temperature pattern is given by Figure 3.7). The convective precipitation (Fig. 3.10a) and surface wind (Fig. 3.10b) all display a sharp increase with time at around 60-70 days. Again, the onset is cross-equatorial, as can be seen from the convective precipitation plot (Fig. 3.10a). The convective precipitation shows two minima at the time of strongest meridional circulation (around day 100). One is located at the same side of the equator as the forcing and the
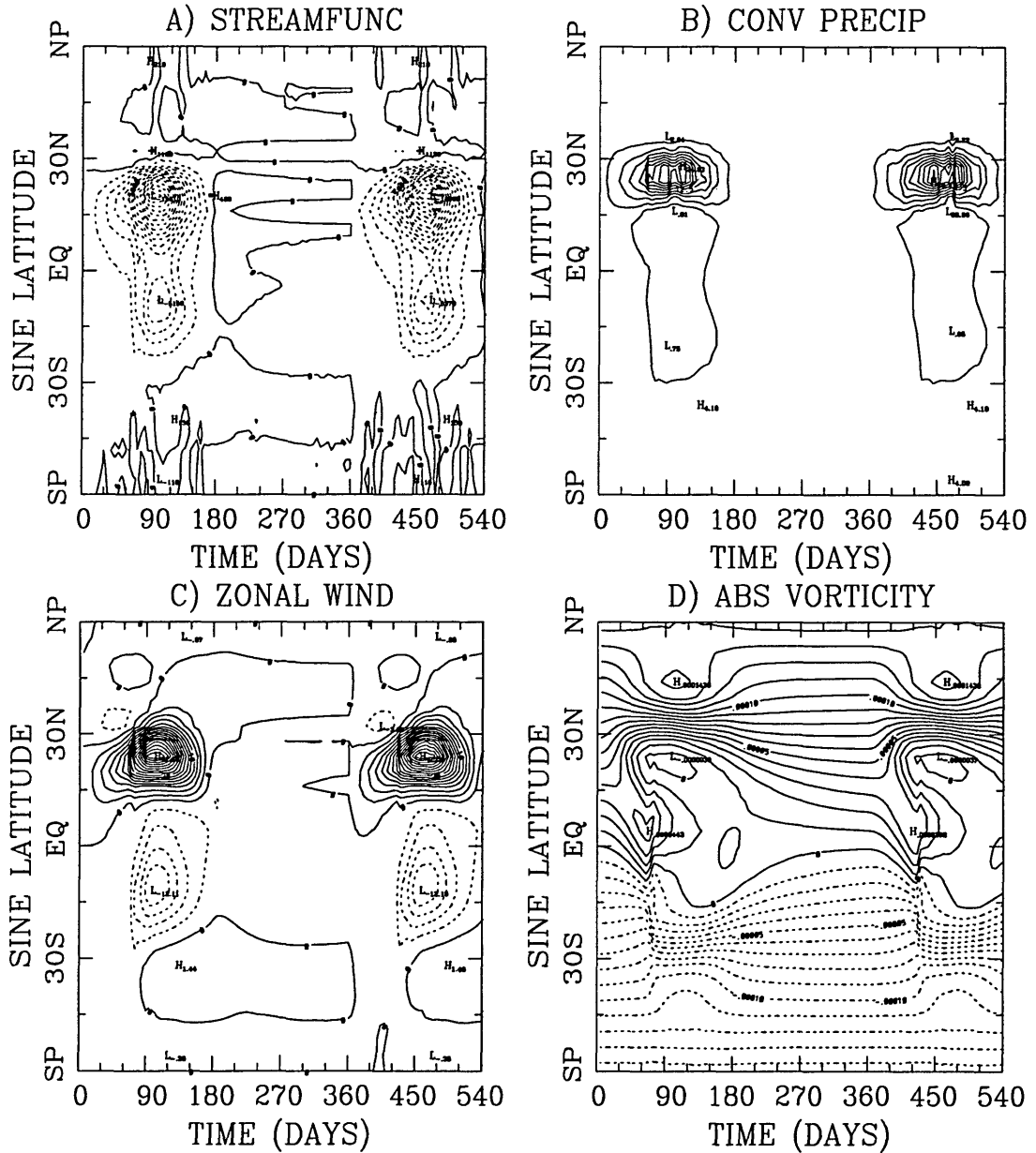
Figure 3.8: Time (day) — Sine Latitude plot of (a) streamfunction at 3km level (contour interval $1 \times 10^3 \mathrm{m}^2 \mathrm{s}^{-1}$), (b) convective precipitation (contour interval 2.5 mm/day), (c) zonal component of the surface wind (contour interval 2.5 ms^{-1}) and (d) absolute vorticity at the tropopause (contour interval 1×10^{-4} s^{-1}) ; for the flat background temperature 290.0K: $T_{max} = 18.0$K.
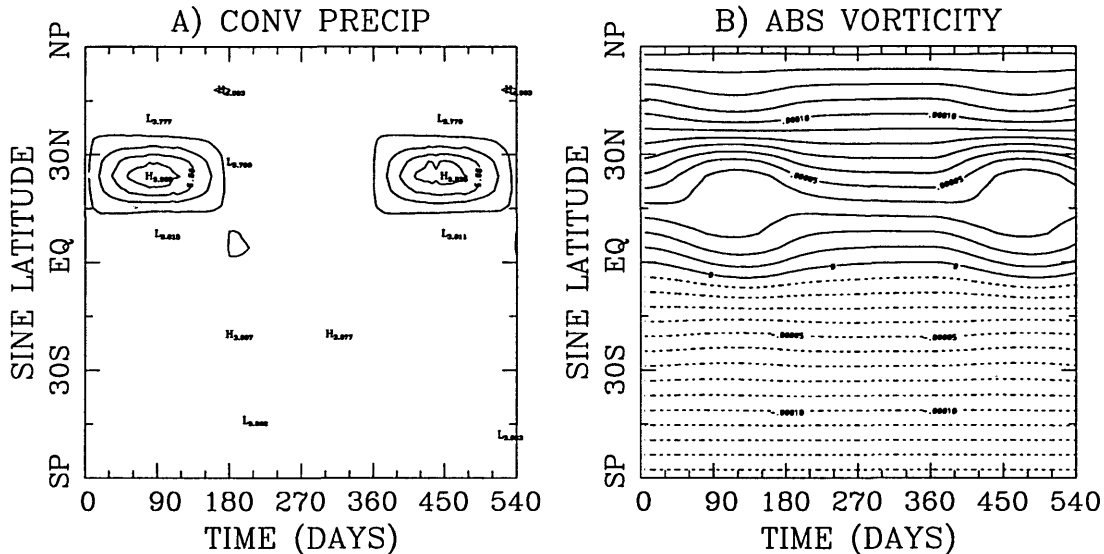
Figure 3.9: Time (day) — Sine Latitude plot of (a) convective precipitation (contour interval 0.5 mm/day) and (b) absolute vorticity at the tropopause (contour interval 1×10^{-4} s^{-1}); for the flat background temperature 290.0K: $T_{max} = 5.0$K.

other in the Southern Hemisphere, clearly due to two downdrafts as illustrated in Section 3.4.1 (Fig. 3.3).

We have also done the case where the forcing is located at the preexisting zero absolute vorticity region (by halving the rotation rate); the results (not shown here) simply confirm the steady-state experiments.

3.5 Local and Global AMC Regimes

We know that once the regularity condition is violated, the atmospheric response to such a forcing must adopt an AMC regime. However, we don't know a priori whether this AMC circulation remains local (not extending across the other side of the equator) with the forcing or if it can extend across the equator as we have seen in our experiments above. For the parameters we chose in Section 3.4, it seems from Figure 3.2 that the resulting AMC regime adopts the global form following the violation of the regularity condition. However, this may be parameter dependent.
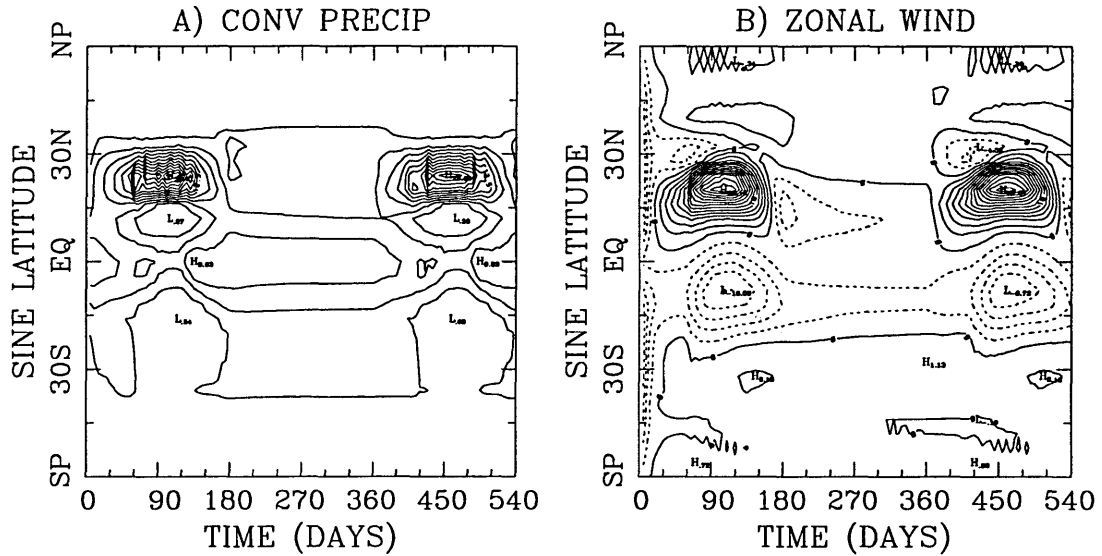
Figure 3.10: Time (day) — Sine Latitude plot of (a) convective precipitation (contour interval 2.5 mm/day) and (b) zonal component of the surface wind (contour interval 2.5 ms^{-2}); with symmetric temperature background 3.4: $T_{max} = 18.0$K.

Schneider (1983) used a delta-function type of forcing (thus the regularity condition is always violated based on (3.1)) to show that the local AMC regime switches to the global AMC regime as the forcing magnitude increases, suggesting that the transition marks the onset of the Martian dust storm. In this section, we conduct a series of numerical experiments similar to Section 3.4.1, but with the forcing half-width halved to 7.5°. This is a case somewhat in between what we have done above (half width 15°) and that of Schneider (1983) (half width zero). We want to check how the response varies with the forcing magnitude. Higher horizontal resolution is needed when we use a narrow forcing with 7.5° half width. We now have 60 intervals in the horizontal with a resolution of about 1.9°. The surface temperature distribution is given again by (3.3). Again, for different forcing magnitudes (from 2.0K to 14.0K every 2.0K increment), the model is integrated to achieve quasi-steady states. The maximum streamfunction against the forcing magnitude is given by Figure 3.11. The linear regime refers to cases where the upper level absolute vorticity still positive. The local AMC regime refers to cases where the upper level absolute vorticity is negative above

the forcing but the circulation is local. Finally, the global AMC regime refers to the onset of the cross-equatorial meridional circulation. We can see that the local AMC regime does exist for intermediate magnitudes of forcing (6K, 8K, 10K). Therefore, in general, as the forcing magnitude increases, the responses experience linear, local AMC and global AMC regimes. For the normal half width of the forcing as we used 15° in our experiments in Section 3.4, the local AMC phase is almost non-existent. However, as we show in this section, as the forcing narrows, the local AMC regime can stand out. Only when the global AMC regime occurs does the streamfunction increases abruptly.
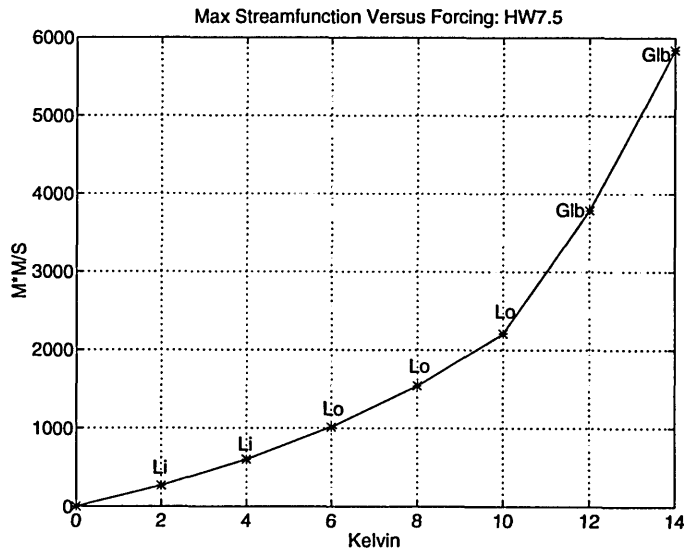
Figure 3.11: The equilibrated maximum streamfunction against the forcing magnitude (T_{max}) of the surface temperature perturbation: steady case without equatorial forcing (localized), half width 7.5°. Note that 'Li' means linear regime, 'Lo' local AMC regime, 'Glb' global AMC regime.

3.6   Summary

In this chapter, by developing a model with an explicit hydrological cycle, we are able to investigate how the dynamics-moisture feedback may affect the results of PH92.

In addition, this model also allows us to check the theoretical prediction by Emanuel (1995). From the results discussed above, we can draw the following conclusions:

(1). From the moist steady-state inviscid theory developed by Emanuel (1995), we estimate the threshold for moist atmospheres. For a reasonably defined thermal equilibrium state, the threshold is easily attainable (Section 3.3.2). For a localized subtropical surface temperature perturbation, the threshold behavior is very clear in our moist symmetric model, even though we have added the interaction between the large-scale flow and the convection (Section 3.4.1). It is argued that the dynamical, inertial rigidity is the reason for this.

(2). The model equilibrated sub-cloud entropy follows roughly the theoretical profile obtained by Emanuel (1995) (Eq. (3.2)). This confirms the scaling analysis of Emanuel (1995) that the onset of the meridional circulation will effectively suppress the supercriticality and the actual sub-cloud entropy should not be very far from the critical curve within the region of strong meridional circulation.

(3). A surface temperature curvature at the equator will necessarily drive a meridional circulation. Even so, as we have shown in Section 3.4.2, the dynamical regime with weak subtropical forcing is different from the regime in which the subtropical temperature perturbation is supercritical. Even though we put the forcing inside the preexisting zero absolute vorticity region at upper levels, the maximum streamfunction versus forcing magnitudes still displays two noticeable regimes (Fig. 3.6). The constraint of the upper level absolute vorticity plays an essential role in shaping the nonlinear feature of the relation between the strength of the meridional circulation and the forcing magnitude.

(4). The extension of the calculations to a seasonally varying surface temperature perturbation (Section 3.4.3) shows that the dynamical rigidity still exists even for the time-dependent (seasonal time scale) system. The steady-state theory can be applied at least to the time-varying subtropical temperature perturbation with a seasonal time scale, which is the time scale we are interested in terms of real monsoon episodes.

(5). We have also explored the possibility of the existence of local AMC regimes. In general, the response of the atmosphere to a subtropical forcing experiences linear, local AMC, and global (cross-equatorial) AMC phases as the forcing magnitude increases. The local AMC regime can be viewed as a transitional phase from the linear regime to the global AMC regime (in which the circulation is very strong). For a normal latitudinal width of the forcing (15°) we hardly see the local AMC regime whereas as we deliberately narrow the width down to 7.5°, the transition phase (local AMC) is clear.

Attempts to use zonally-symmetric models to simulate the monsoon circulation have been made by several previous investigators (e.g., Webster and Chou, 1980a,b; Webster, 1983). Our model here is not meant to simulate the real monsoon, but to understand the moist dynamics of the system. Webster and Chou (1980a,b) concluded that moist processes were crucial for their model to simulate realistic monsoons. Our model shows that the dynamical constraint of the system, namely the absolute vorticity at upper levels, may also control the behavior of the onset of the thermally-direct circulations such as monsoons, besides moist processes themselves.

There is a hint that this dynamical constraint may be related to the observed abrupt monsoon rainfall and wind increases (Fig. 1.3). For example, the sudden increase of the wind during the onset of the cross-equatorial meridional circulation (e.g., Fig. 3.8, Fig. 3.10) in our model resembles the sharp increase of the rotational wind in the real monsoon episode (Fig. 1.3). The similar abrupt increase is also applicable to convective precipitation in our model. In real monsoon episodes, this kind of somewhat abrupt change from pre-monsoon period to post-monsoon period of various physical quantities (e.g., surface wind, rainfall, position of upper-level jet) has been observed very often both in observational and in modeling studies as we have reviewed in the Chapter 1. We may speculate from PH92 and this work that the abrupt change associated with the monsoon onset has to do with the inertial rigidity (upper-level absolute vorticity) of the system and it is this constraint that

distinguishes the pre-monsoon and post-monsoon regimes.

On the other hand, we should be aware the limitations of these studies. In particular, the three-dimensionality of the real monsoon may be important. Clearly more work has to be done before we can finally identify the role of the upper-level absolute vorticity in shaping the sharp increase of wind and rainfall during the monsoon onset. As we have seen in the Section 1.4, we do have some empirical evidence showing the existence of the constraint of absolute vorticity in the real world. In addition, the theoretical work by Schneider (1987) shows that the existence of net integrated divergence at the upper level requires zero absolute vorticity. Therefore, we believe that the dynamical constraint (absolute vorticity) at upper levels may likely be relevant even to the real three-dimensional systems. For example, Emanuel (1986) showed this within the context of tropical cyclones.

Even within the context of zonal symmetry (which is the focus of this thesis), the model here fails to consider land surface processes. In particular, the land surface is not always an infinite moisture source, as we have assumed here. The evaporation depends very much on soil moisture and may not be able to achieve its potential value. This issue will be addressed next when we come to investigate West African monsoons.

Chapter 4

The Role of Vegetation in the Dynamics of West African Monsoons

4.1   Background

Observations from West Africa indicate a significant decline in rainfall levels since the early 1960s (e.g., Nicholson, 1994; Hulme, 1994), see Fig. 4.1. This continuing drought episode spans most of the last three decades, with a decline in rainfall levels that is large enough to suggest a significant change in the normal[1] regional climate for this century (Eltahir, 1992; Farmer and Wigley, 1985). Whether or not this long episode of deficient rainfall will continue remains to be seen. Nevertheless, these observations have motivated many studies on rainfall, droughts, and climate variability over West Africa. Most of these studies can be classified into two groups: studies that emphasize the role of local land-atmosphere interaction in the regional climate, and studies that emphasize the role of ocean-atmosphere interaction and Sea Sur-

---

[1]Normal here means the long-term average over this century.

face Temperature (SST) distribution in the variability of rainfall over West Africa. This chapter concerns the role of land surface processes in the rainfall variability over West Africa. In the next chapter we will investigate the possible influence of tropical Atlantic SST on West African rainfall.
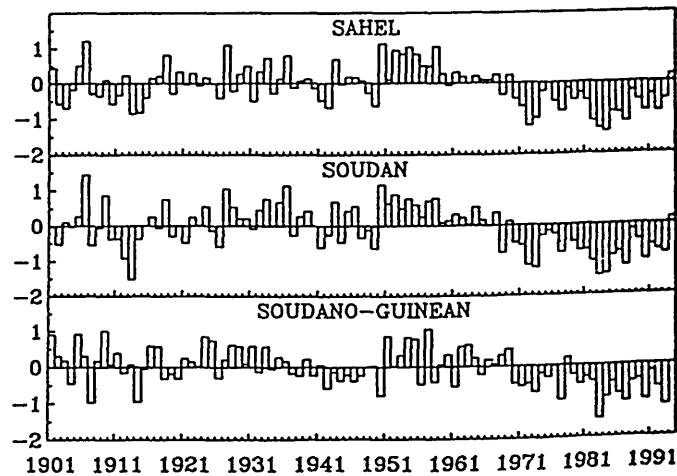
Figure 4.1: The normalized rainfall anomalies over West Africa, adopted from Nicholson *et al.* (1996).

First, studies concerned with the role of land-atmosphere interaction in the variability of regional climate investigate the role of land-surface processes that involve vegetation, soil moisture, surface albedo, and evaporation in the dynamics of regional rainfall. The pioneering study on land-atmosphere interaction in this region is that of Charney (1975), which presented a hypothesis for describing the mechanisms of droughts. This hypothesis suggested a significant role for vegetation in the dynamics of rainfall over the Sahel, implying that the rainfall-producing circulation over this region is sensitive to changes in the state of vegetation at the desert border with the Sahara. However, Charney's theory did not address the role of soil moisture and evaporation, which motivated other studies such as Walker and Rowntree (1977) to investigate the effect of soil moisture conditions on circulation and rainfall in West

Africa. The role of land surface processes in the regional climate was investigated by several modeling studies: Charney *et al.* (1975), Charney *et al.* (1977), Yeh *et al.* (1984), Sud and Fennessy (1984), Sud and Molod (1988), Cunnington and Rowntree (1986), Kitoh *et al.* (1988), Powell and Blondin (1990), Rodriguez-Iturbe *et al.* (1991), and Xue and Shukla (1993). The results of these studies suggest that the conditions of the land surface as characterized by vegetative cover and soil moisture play a significant role in rainfall variability over West Africa. Among those studies on the impact of vegetative cover (e.g., Charney *et al.*, 1975; Xue and Shukla, 1993), it is generally concluded that the desertification near the sub-Saharan desert border reduces rainfall within the region of vegetation perturbation and increases rainfall south of the perturbation region. The soil moisture-rainfall feedback is often found to be able to sustain rainfall anomaly and thus a positive feedback (e.g., Walker and Rowntree, 1977; Yeh *et al.*, 1984).

The second group of studies is concerned with the role of the ocean, and in particular the distribution of SST, in the dynamics of climate over West Africa. The relation of rainfall over this region to the distribution of SST in the tropical Atlantic has been the focus of several studies. At the regional scale, Lamb (1978a, 1978b), and Lamb and Peppler (1992) investigated the relation of Sahel rainfall to the distribution of SST over the Atlantic Ocean. In a similar study, Lough (1986) identified the dominant spatial patterns of normalized SST departures in the tropical Atlantic using principal component analysis, and then correlated these different patterns to rainfall in the Sahel region. At the global scale, Folland *et al.* (1986) discussed the relation between Sahel rainfall and worldwide SST distribution. The use of SST observations for the purpose of forecasting rainfall in the Sahel was explored by Owen and Ward (1989) using a global SST data set. The results of all these studies suggest that the conditions over the Atlantic Ocean as characterized by SST may play a significant role in rainfall variability over West Africa. The role of tropical Atlantic SST in the dynamics of West African monsoons will be discussed in the next chapter.

A different view on the mechanisms of floods and droughts over West Africa has been proposed recently by Eltahir and Gong (1996). They suggested that rainfall variability over this region is a manifestation of a large scale ocean-land-atmosphere interaction. According to this theory, dynamics of wet and dry years over West Africa are governed by not only the land-atmosphere interaction, or the ocean-atmosphere interaction considered independently; but the critical factor to consider is the meridional gradients of boundary layer conditions between the land and the Atlantic Ocean. The measure that was proposed to describe these conditions over land and the ocean is the meridional gradient of moist entropy (or moist static energy). This theory predicts that a flat meridional distribution of entropy does not drive any circulation (sub-critical TE regime in PH92), and that a relatively large gradient of entropy should drive a strong monsoon circulation (super-critical regime in PH92) which is of course the main rainfall-producing system in the Sahel region.

The study of Eltahir and Gong (1996) builds on the results of the earlier studies on the dynamics of zonally-symmetric thermally-direct atmospheric circulations by Held and Hou (1980), Lindzen and Hou (1988), and in particular Plumb and Hou (1992) and Emanuel (1995). The dynamics of monsoons within the framework of zonally-symmetric atmosphere have been reviewed in Section 1.2.3. In short, for a meridional circulation to develop over any tropical or subtropical region off the equator, the absolute vorticity near the tropopause has to reach a threshold value of zero somewhere. However, for a moist atmosphere that satisfies a quasi-equilibrium balance between moist convection and radiative forcing, the absolute vorticity at upper tropospheric levels is a function of latitude and the meridional distribution of boundary layer entropy. Hence, the onset of a monsoon circulation depends in a nonlinear fashion on these two factors. Eltahir and Gong (1995) argued that the location of the region of West Africa, relatively close to the equator, dictates that the dynamics of monsoon over the region are relatively sensitive to inter-annual fluctuations in the meridional gradient of boundary layer entropy. They further presented observations

on entropy and wind over West Africa during the monsoon seasons of 1958 and 1960. These observations are consistent with the proposed relation between boundary layer entropy and the monsoon circulation: a large meridional gradient of boundary layer entropy, a healthy monsoon, and wet conditions over the Sahel region were observed in 1958; a nearly flat distribution of entropy, very weak circulation, and relatively dry conditions were observed in 1960.

The proposed relation between the meridional gradient of boundary layer entropy and the monsoon circulation over West Africa is consistent with the empirical observations of Sea Surface Temperature Anomalies (SSTAs) in the tropical Atlantic, and rainfall in the Sahel region (Lamb, 1978a; Lamb, 1978b; Lough, 1986). Theoretically, a cold (warm) SSTA in the region located south of the West African coast should favor a large (small) meridional gradient of entropy, a strong (weak) monsoon circulation, and wet (dry) conditions in the Sahel. A large body of observations confirms that cold (warm) SSTAs off the southern coast of West Africa are associated with wet (dry) years in the Sahel region (Lamb, 1978a; Lamb, 1978b; Lough, 1986; Owen and Ward, 1989). However, the gradient of entropy is also controlled by the relative boundary conditions over land. In particular, the distribution of vegetation leaves a significant signature in the meridional distributions of net surface radiation, total surface heat flux, and boundary layer entropy (Eltahir, 1996). The focus of this chapter is on the role of land boundary layer conditions in the dynamics of West African monsoons and therefore the oceanic conditions (SST) are fixed.

In order to investigate the role of vegetation in the dynamics of West African monsoons, more sophisticated physical processes have to be incorporated into our model framework. We simulate and compare the response of the monsoon circulation to changes in the vegetation distribution considering several different scenarios: degradation of land cover along the northern border between West Africa and the Sahara desert (desertification), and degradation of land cover along the southern coast of West Africa (deforestation). While the desertification scenario is similar to the

changes in land cover that were assumed by several previous studies (e.g., Charney, 1975; Charney et al., 1977; Xue and Shukla, 1993), the sensitivity of rainfall in West Africa to deforestation along the coast has not yet received a similar level of attention.

The applications of zonally-symmetric models to West African monsoons assume that the effect of zonal asymmetries can be neglected to the first order. In what follows, we will discuss this assumption, based on the ECMWF data for both the dry year of 1992 and the wet year of 1994 (see Fig. 4.1).

4.2 Zonally-Symmetric Models for Studying West African Monsoons

In the literature, a few studies use zonally-symmetric or zonally-averaged models to study West African monsoons. Most notably, the pioneering work of Charney (1975) used an analytical zonally-symmetric model to study the qualitative effect of increasing surface albedo on Sahelian rainfall. Xue et al. (1990) investigated the impact of sub-Saharan desertification on West African rainfall using a zonally-averaged model of the West African monsoon. Their justification of using two-dimensional model is based on the fact that West Africa has fairly zonally-uniform distribution of rainfall, vegetation and other meteorological quantities. No quantitative analyses were presented in both of those studies. Here, we go one step further to assess the effect of ignoring zonal asymmetries by looking at the water vapor, angular momentum and moist static energy budget for the region of West Africa, for both the dry year of 1992 and the wet year of 1994.

4.2.1 Water Vapor Divergence

We use the monthly averaged data from ECMWF. The West Africa is defined here as the region from 15°W to 15°E, 5°N to 20°N, as sketched in Fig. 4.2.
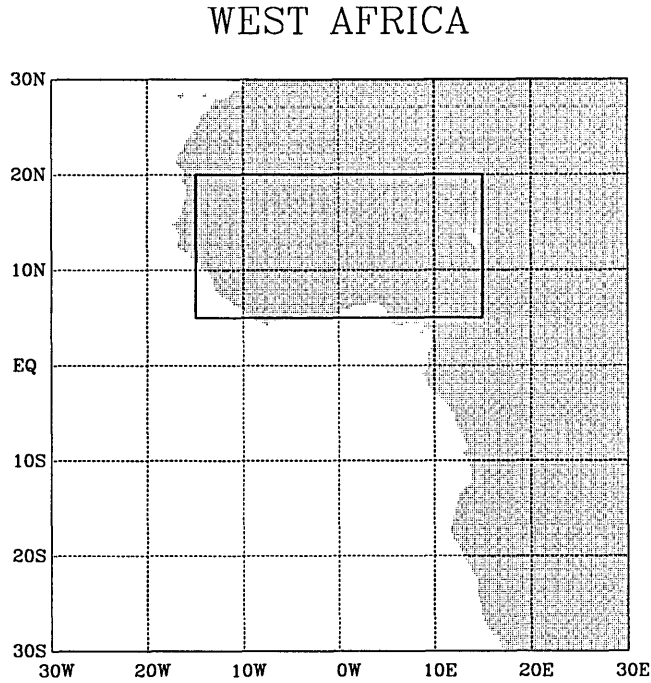
WEST AFRICA

Figure 4.2: The map of West Africa and the region of the study, defined as the region from 15°W to 15°E, 5°N to 20°N (the dark rectangle).

According to Newell *et al.* (1972a), the water vapor conservation can be expressed as:

$$\frac{\partial W}{\partial t} + \nabla \bullet Q = E - P, \tag{4.1}$$

where $W = \frac{1}{g} \int_{p_u}^{p_s} q dp$, is precipitable water, p_s surface pressure, p_u the pressure above which the flux and flux divergence become negligible (here it is taken as 275 mb); $Q = i \, Q_\lambda + j Q_\phi$, where i, j are eastward and northward pointing unit vector, respectively. Here the total zonal flux of water vapor Q_λ is defined as:

$$Q_\lambda = \frac{1}{g} \int_{p_u}^{p_s} q u dp, \tag{4.2}$$

and the total meridional flux of water vapor Q_ϕ is:

$$Q_\phi = \frac{1}{g} \int_{p_u}^{p_s} qv\,dp, \tag{4.3}$$

The monthly averaged fluxes of water vapor can then be expressed as:

$$\overline{Q}_\lambda = \frac{1}{g} \int_{p_u}^{p_s} \left(\overline{q}\,\overline{u} + \overline{q'u'} \right) dp, \tag{4.4}$$

and

$$\overline{Q}_\phi = \frac{1}{g} \int_{p_u}^{p_s} \left(\overline{q}\,\overline{v} + \overline{q'v'} \right) dp, \tag{4.5}$$

where overbars indicate the monthly mean values; primes indicate the transient eddies. Our data set only consists of monthly averaged fields. However, as demonstrated by Flohn et al. (1965) and Rasmussen (1972), over West Africa in summer, the total water vapor fluxes are dominated by the monthly mean winds, with transient eddy fluxes an order of magnitude smaller. Therefore, we can approximately calculate the water vapor fluxes using monthly mean winds, a procedure also used by Kidson (1977) in his analysis.

For the region of this study, which is sketched by the dark rectangle in Fig. 4.2, the net divergence of water vapor can be expressed, through application of the Gauss theorem as: $(F_x + F_y)/A$, where F_x is the amount of net water vapor flux across eastern-western boundaries; F_y[2]is the amount of net water vapor flux across northern-southern boundaries; A is the area of the region. A can be calculated by:

---

[2]The unit of F_x and F_y is kg s^{-1}.

$$A = a^2 \Delta\lambda \left(\sin\phi_2 - \sin\phi_1\right), \tag{4.6}$$

where $\Delta\lambda = \frac{\pi}{6}$, which is the longitude difference between the east and the west boundaries in radians; $\phi_1 = 5°N$ (southern boundary) and $\phi_2 = 20°N$ (northern boundary); a the earth's radius.

The zonal fluxes (Q_λ) of water vapor in August for 1992 (dry) and 1994 (wet) are shown in Fig. 4.3. The meridional fluxes (Q_ϕ) of water vapor are shown in Fig. 4.4. The magnitude of zonal fluxes is in general larger than that of meridional fluxes. This is because the zonal wind is much larger than the meridional wind in terms of the magnitude. In addition to that, the zonal fluxes show prevailing westward transport of moisture in most of the regions except the region of strong monsoon south-westerlies — south of around 10°N. In the mean time, the meridional fluxes show northward transport by the monsoon south-westerlies from the tropical Atlantic Ocean to the West African region. The qualitative features of water vapor transport agree well with the study of Kidson (1977) in which he showed that streamlines of the water vapor flux are fairly zonal.

However, the more meaningful quantity to look at is the divergence of the water vapor for the region of our study. In order to be able to apply zonally-symmetric models to study West African monsoons, the net zonal water vapor flux F_x (magnitude) must be substantially smaller than the net meridional water vapor flux F_y (magnitude), during the summer months. In other words, the total net water vapor flux within the region ($F_x + F_y$) must be dominated by F_y. The seasonal variations of F_x, F_y and ($F_x + F_y$), scaled by the area of the region of our study A (eq. (4.6)), are shown by Fig. 4.5 for 1992 and by Fig. 4.6 for 1994. The positive values indicate net water vapor into the region and negative values indicate net water vapor out of the region. It is very clear that the net meridional fluxes are dominant over the zonal
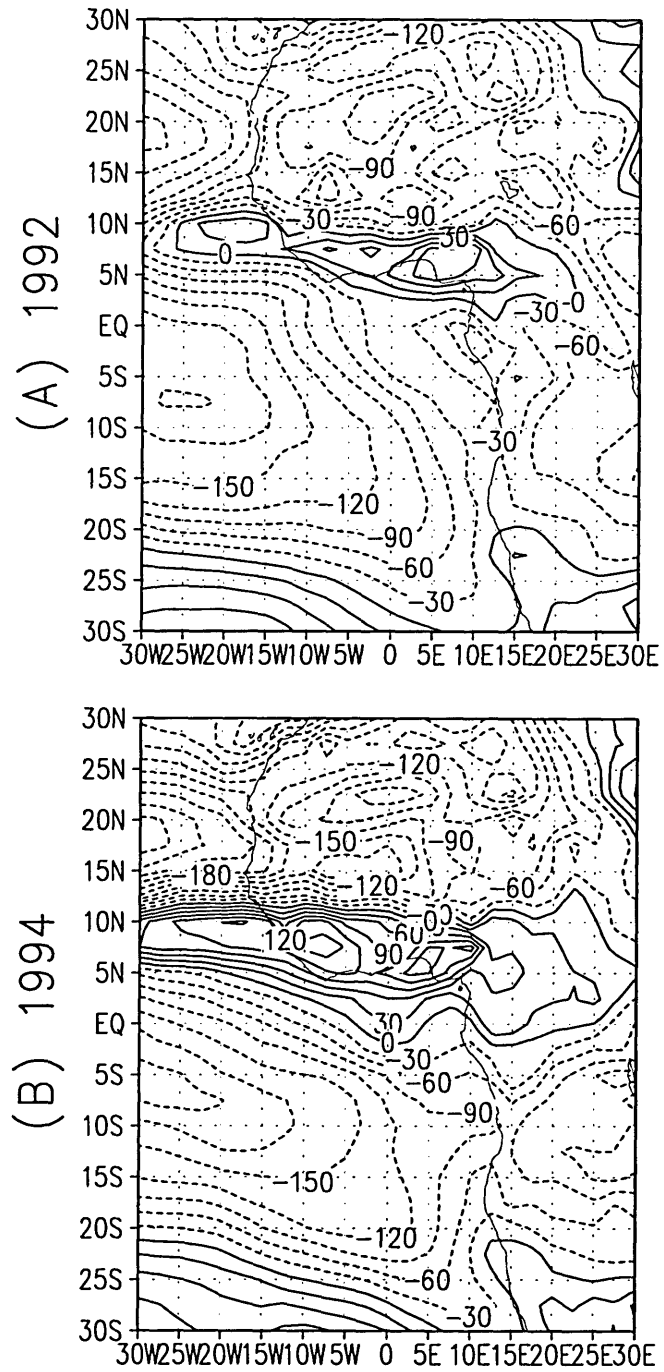
Figure 4.3: The vertically-averaged zonal water vapor flux (Q_λ, contour interval 30 kgm^{-1}s^{-1}) in August for (a) 1992, (b) 1994.
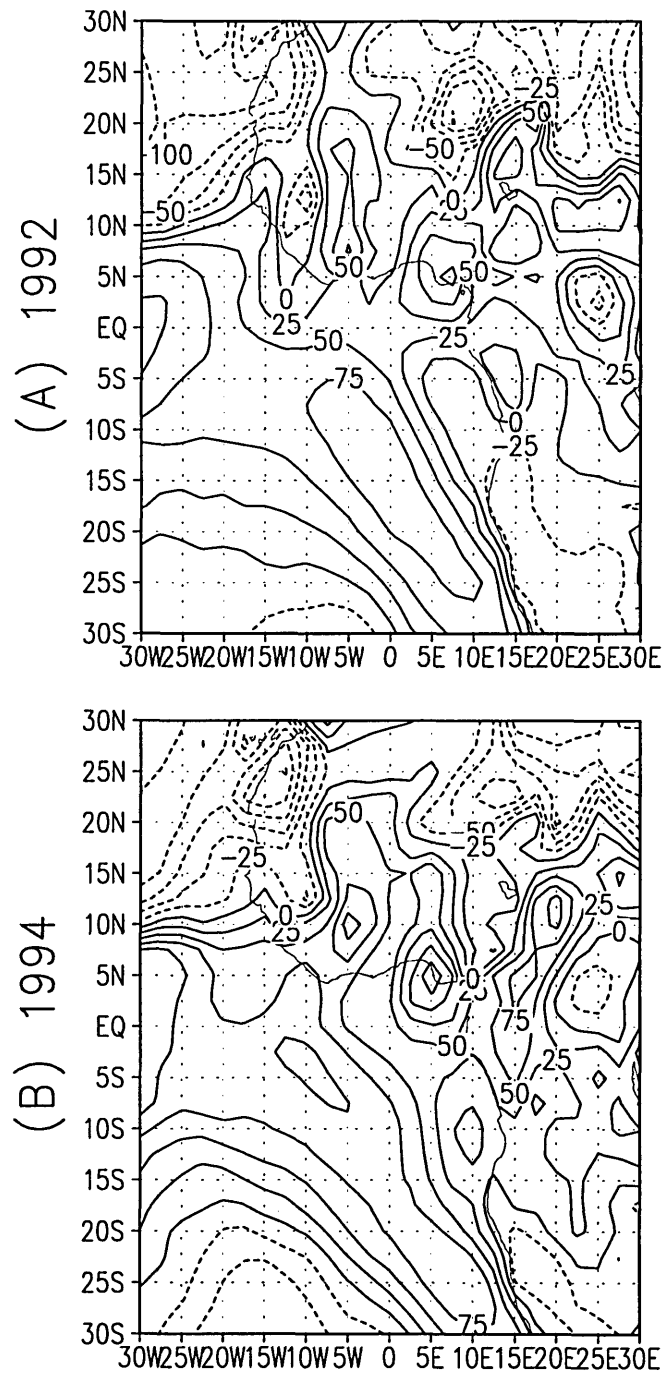
Figure 4.4: The vertically-averaged meridional water vapor flux (Q_ϕ, contour interval 25 $kgm^{-1}s^{-1}$) in August for (a) 1992, (b) 1994.

Water Vapor Fluxes 1992
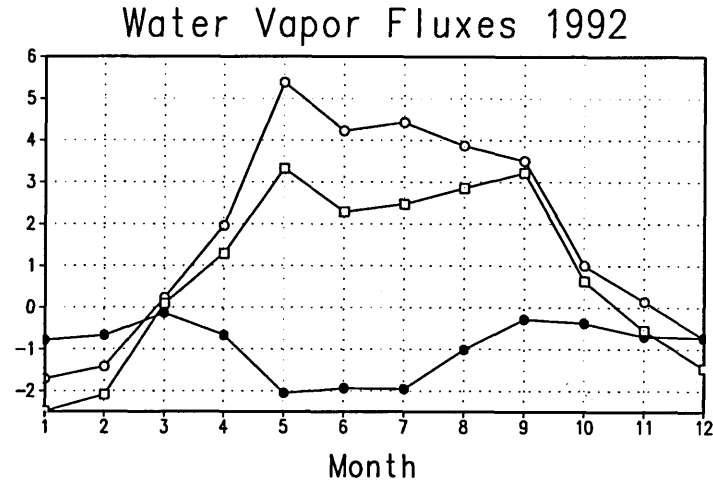
Figure 4.5: The seasonal evolution of the net water fluxes into the region of study, scaled by the area of the region A, which can be calculated by equation (4.6), for 1992. The bullets indicate the net flux across the eastern-western boundaries (F_x); the circles the net flux across northern-southern boundaries (F_y); the squares the total net fluxes. Positive values mean the net convergence of water vapor flux, negative values mean the net divergence of water vapor flux. The unit is 10^{-5} kgm^{-2}s^{-1}.

fluxes in summer (July-September), for both dry (1992) and wet (1994) years. It seems that the zonal water flux divergence (F_x) is negative over most of the summer, except slightly positive in September of 1994. This suggests that the zonal asymmetries contribute a net water vapor flux out of the region. Compared to the net meridional water vapor flux (F_y) in the region, the effect of zonal asymmetries on the water vapor flux divergence is secondary, if not absolutely negligible. In particular, in August and September when the rainfall reaches maximum in West African region (see Fig. 5.3), the contribution of F_x to the total net water vapor flux is only around 30 % or less.

In summary, from the standpoint of water vapor divergence in West Africa, which we defined as the region in Fig. 4.2, the effect of north-south water vapor flux divergence is dominant. In fact, during summer months, the net meridional flux of water vapor injects moisture into the West African region. At the same time, the net

Water Vapor Fluxes 1994
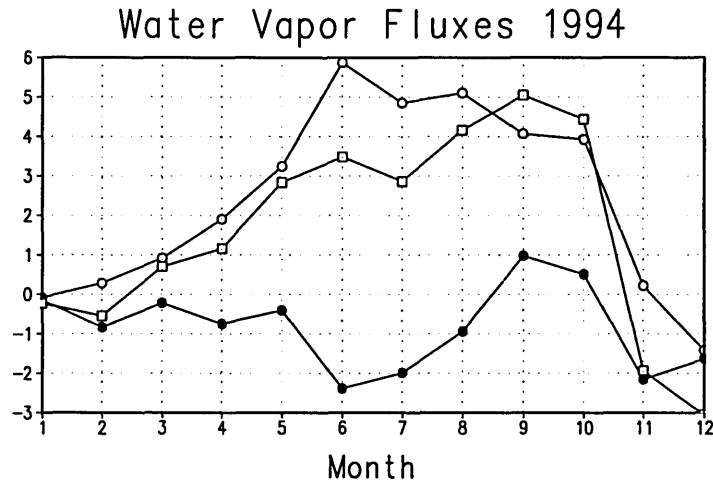
Figure 4.6: The seasonal evolution of the net water fluxes into the region of study, scaled by the area of the region A, which can be calculated by equation (4.6), for 1994. The bullets indicate the net flux across the eastern-western boundaries (F_x); the circles the net flux across northern-southern boundaries (F_y); the squares the total net fluxes. Positive values mean the net convergence of water vapor flux, negative values mean the net divergence of water vapor flux. The unit is 10^{-5} kgm^{-2}s^{-1}.

zonal flux of water vapor brings moisture out of the region with substantially smaller magnitude. This study agrees with Lamb (1983) where he found that the evaporation over the tropical Atlantic Ocean is the primary moisture source for the West African monsoon. Gong and Eltahir (1996) also pointed out the rainfall over West Africa is almost in phase with the moisture flux from the tropical Atlantic Ocean. In short, zonally-symmetric models should be applicable to the study of West African monsoons, as long as we are interested in rainfall variability on time scales of one month to season. Furthermore, we want to emphasize here that zonally-symmetric models are not designed to simulate real monsoons in great details. On the other hand, these models allow us to explore physical processes extensively.

4.2.2 Angular Momentum

We now perform the similar analysis for the same region we defined in Fig. 4.2, but for angular momentum. Since our objective here is to estimate the effect of zonal asymmetries, we mainly concentrate on horizontal fluxes of vertically-averaged angular momentum. The complete conservation of angular momentum can be written as follows (Newell *et al.*, 1972a):

$$\frac{\partial \overline{M}}{\partial t} + \frac{1}{a\cos\phi}\left(\frac{\partial \overline{J}_\lambda}{\partial \lambda} + \frac{\partial}{\partial \phi}\overline{J}_\phi \cos\phi\right) + \frac{\partial \overline{J}_p}{\partial p} = -\frac{\partial \overline{\Phi}}{\partial \lambda}, \tag{4.7}$$

where the angular momentum is defined as in equation (1.1). Overbars mean time-averaged quantities. The fluxes of angular momentum are defined as:

$$\overline{J}_\lambda = a^2\cos^2\phi\,\Omega\overline{u} + a\cos\phi(\overline{u}\,\overline{u} + \overline{u'u'}), \tag{4.8}$$

$$\overline{J}_\phi = a^2\cos^2\phi\,\Omega\overline{v} + a\cos\phi(\overline{u}\,\overline{v} + \overline{u'v'}), \tag{4.9}$$

and

$$\overline{J}_p = a^2\cos^2\phi\,\Omega\overline{\omega} + a\cos\phi(\overline{u}\,\overline{\omega} + \overline{u'\omega'}) + ga\cos\phi\overline{\tau}_\lambda. \tag{4.10}$$

Here primes indicate transient eddies. (u, v, ω) are wind components; $\overline{\tau}_\lambda$ is surface drag in x direction; Other notations have been defined before. Over the West African region, the effect of transient eddies is generally of second importance, compared to mean motions (Newell *et al.*, 1972a). So again, we can use the monthly averaged data

to assess the net fluxes of angular momentum. Similar to the analysis of water vapor fluxes, we examine the vertically averaged fluxes of angular momentum ($\frac{1}{g}\int_{p_u}^{p_s}\overline{J}_\lambda dp$ and $\frac{1}{g}\int_{p_u}^{p_s}\overline{J}_\phi dp$), for both the dry year of 1992 and the wet year of 1994.

For the region sketched in Fig. 4.2, the time evolution of net angular momentum fluxes in 1992 is shown in Fig. 4.7. We can see clearly that the net angular momentum flux across eastern-western boundaries is much smaller than the net angular momentum flux across northern-southern boundaries. This suggests the influence of zonal asymmetries can be neglected compared to the meridional angular momentum flux divergence. This conclusion also applies to the wet year of 1994, as shown in Fig. 4.8.
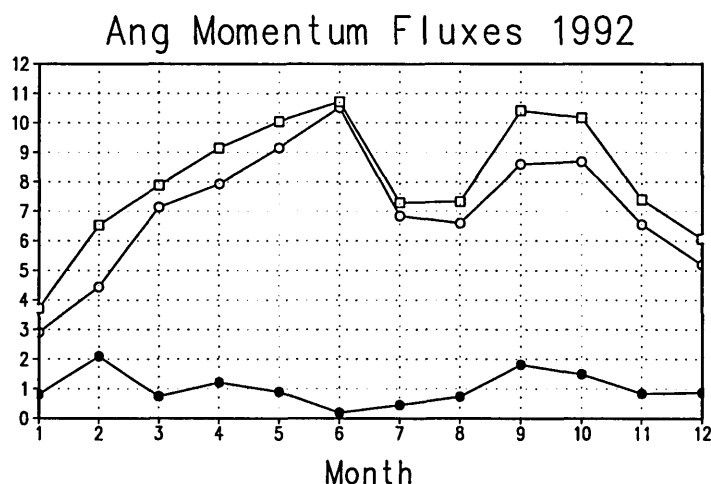
Figure 4.7: The seasonal evolution of the net vertically-averaged angular momentum fluxes into the region of study, scaled by the area of the region A, which can be calculated by equation (4.6), for 1992. The bullets indicate the net flux across the eastern-western boundaries; the circles the net flux across northern-southern boundaries; the squares the total net fluxes. Positive values mean the net convergence of angular momentum flux. The unit is 10^7 kgs^{-2}.

4.2.3   Moist Static Energy

Finally, we examine the effect of neglecting zonal asymmetries on moist static energy, which has been shown to be a crucial quantity in moist atmospheres (Emanuel, 1994;

86

Ang Momentum Fluxes 1994
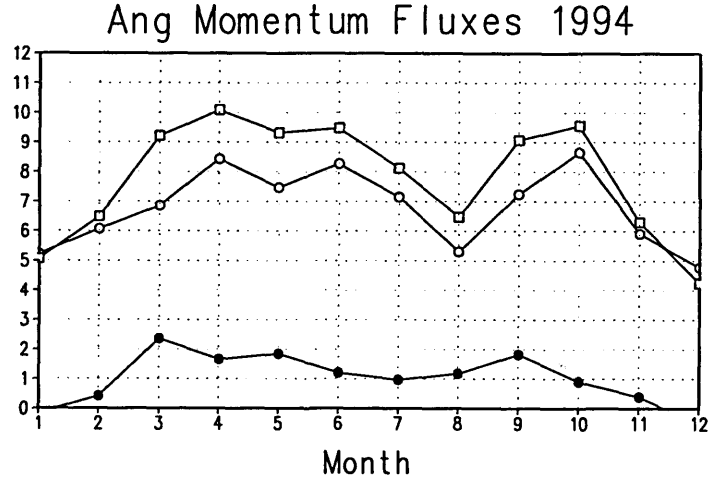
Figure 4.8: The seasonal evolution of the net vertically-averaged angular momentum fluxes into the region of study, scaled by the area of the region A, which can be calculated by equation (4.6), for 1994. The bullets indicate the net flux across the eastern-western boundaries; the circles the net flux across northern-southern boundaries; the squares the total net fluxes. Positive values mean the net convergence of angular momentum flux. The unit is 10^7 kgs^{-2}.

Emanuel *et al.*, 1994). Similar to our analyses of both water vapor and angular momentum, the monthly averaged vertically-averaged zonal flux of moist static energy $(\overline{M}_\lambda)$ can be approximated by:

$$\overline{M}_\lambda = \frac{1}{g} \int_{p_u}^{p_s} \left(C_p \overline{T} + L_v \overline{q} \right) \overline{u} dp, \tag{4.11}$$

where the contribution from transient eddies have been ignored (Newell *et al.*, 1972b); L_v is latent heat of vaporization. The vertically-averaged meridional flux of moist static energy $(\overline{M}_\phi)$ is:

$$\overline{M}_\phi = \frac{1}{g} \int_{p_u}^{p_s} \left(C_p \overline{T} + L_v \overline{q} \right) \overline{v} dp, \tag{4.12}$$

For the region of our study, the time evolution of net moist static energy fluxes in 1992 is shown in Fig. 4.9 and Fig. 4.10 shows the 1994 case. Again, we see that during summer months, the meridional flux divergence is dominant over the zonal flux divergence.
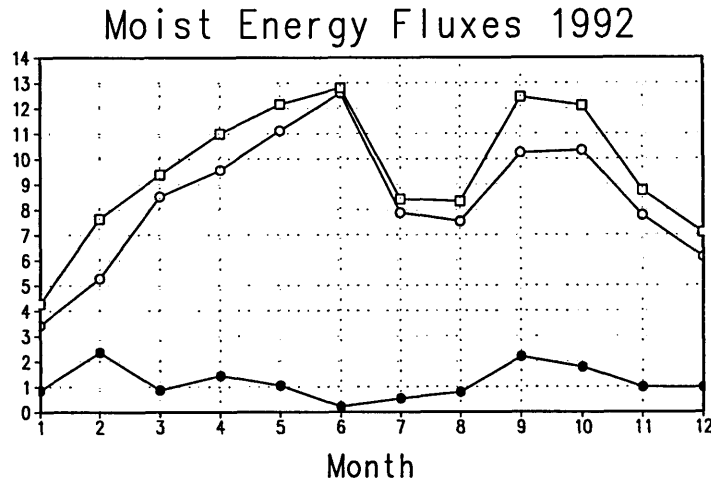
Figure 4.9: The seasonal evolution of the net vertically-averaged moist static energy fluxes into the region of study, scaled by the area of the region A, which can be calculated by equation (4.6), for 1992. The bullets indicate the net flux across the eastern-western boundaries; the circles the net flux across northern-southern boundaries; the squares the total net fluxes. Positive values mean the net convergence of moist static energy flux. The unit is 10^3 W m^{-2}.

By analyzing the effect of zonal asymmetries for the region of West Africa, in terms of moisture and angular momentum as well as moist static energy divergence, we found that the error caused by neglecting zonal asymmetries is secondary. For the West African region, zonally-symmetric models should be sufficient to describe the gross features of seasonal rainfall variability, as long as we are not interested in individual synoptic disturbances, which have to be modeled by three-dimensional models. In what follows, the framework of zonal symmetry will be applied to West African monsoons. Our focus is to understand physical mechanisms using these zonally-symmetric models.

Moist Energy Fluxes 1994
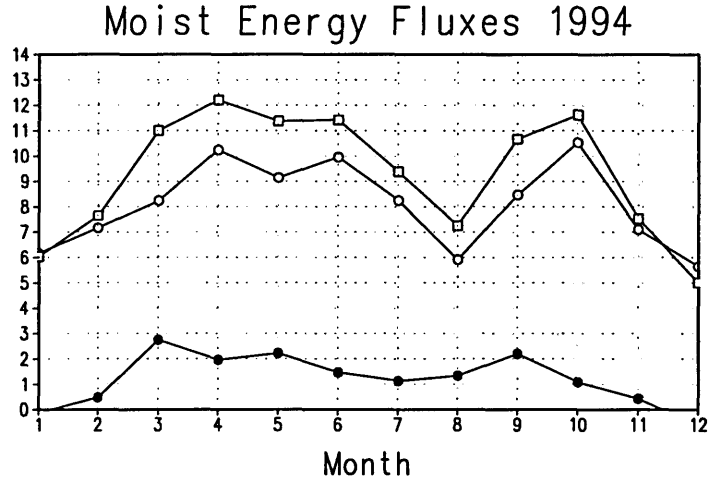
Figure 4.10: The seasonal evolution of the net vertically-averaged moist static energy fluxes into the region of study, scaled by the area of the region A, which can be calculated by equation (4.6), for 1992. The bullets indicate the net flux across the eastern-western boundaries; the circles the net flux across northern-southern boundaries; the squares the total net fluxes. Positive values mean the net convergence of moist static energy flux. The unit is 10^3 W m^{-2}.

4.3 Some Model Details

The model we use in this chapter has essentially the same dynamical framework and convective scheme as we described in Chapter 2. However, since we are concerned with land surface transformation in the dynamics of West African monsoons, land surface processes have to be considered. Land surface temperature is no longer specified, it is determined by the energy balance at the surface. To do so, all radiative fluxes (longwave and shortwave components) at the surface have to be known. Hence, a much more sophisticated physically-based radiation scheme is included.

The model domain is global horizontally and extends from 0 to 25 km (log-pressure) vertically. The grid points are evenly spaced in sine latitude horizontally with 60 increments (about 2.0 degree resolution in tropical regions) and also equally spaced vertically with 25 intervals (1 km vertical resolution). The time step is 20 minutes. The diffusion coefficient is 5 m^{2}s^{-1} (no vertical dependence).

We use a fast radiation parameterization scheme developed by Chou et al. (1991). The scheme combines both longwave and shortwave radiation to produce a computationally fast yet still accurate radiation parameterization. For longwave absorption, this scheme uses Chou (1984) broadband transmission approach for water vapor, Chou and Peng (1983) for carbon dioxide, and Rodgers (1968) method for ozone. The scheme includes the water vapor line and continuum absorption; carbon dioxide absorption through band centers and band wing regions; and infrared ozone-absorption bands.

Solar radiation is absorbed by water vapor and ozone, scattered by cloud droplets, and reflected at the surface. The scheme employs the parameterization method of Lacis and Hansen (1974) for ozone and water vapor. Plane-parallel clouds (modeled with a delta-Eddington two-stream flux model) (King and Harshvardhan, 1986; Joseph et al., 1976) provide fractional coverage. For the experiments we have performed in this thesis, we assume clear sky conditions.

Above the model top (25km, about 38.8 mb, the model surface is 1000 mb), for the calculation of radiative fluxes, we add 9 layers up to 1 mb in radiative equilibrium. The carbon dioxide concentration is 330 ppm. Ozone mixing ratio and stratospheric water vapor profile are from the AFGL (MaClatchey et al., 1972) standard atmosphere.

The surface configuration is as follows: the continental edge is located at 5°N mimicing the southern coast of West Africa; north of it is land whereas south of it is ocean. The ocean surface temperature is specified from the observation as will be discussed later in more detail. The surface albedo for oceanic surface is 0.10. The land surface temperature is computed using the energy balance and assuming zero heat capacity.

We use the Budyko dryness index as an indicator of vegetation type (Budyko, 1974). It is defined as:

$$D = \frac{R}{L_v P},$$

where D is the dryness index; R the annual mean net surface radiation; P the annual mean precipitation, and L_v the latent heat rate of vaporization. However, in this thesis, D is served only as a dummy variable, and is given.
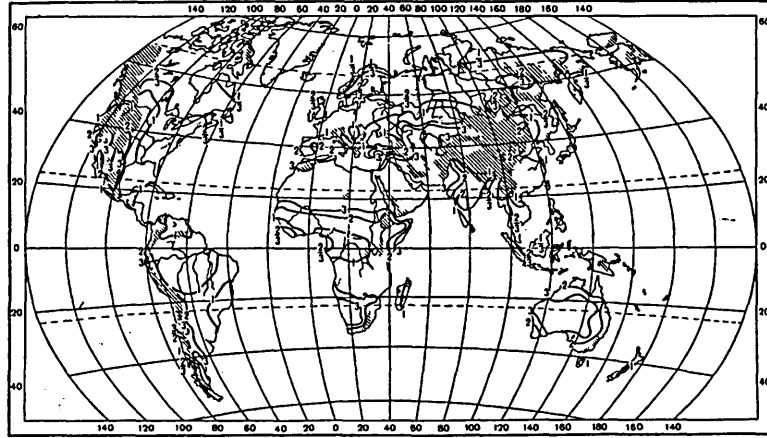
Figure 4.11: The Budyko dryness index over West Africa, adopted from Budyko (1974).

According to Budyko (1974, see Fig. 4.11) , for tropical forest D is generally less than 1.0 whereas for the desert region D is above 3.0. The savanna region D lies between 1.0 to 2.0. The semi-desert region D is from 2.0 to 3.0. In our land surface scheme, we follow Gutman *et al.* (1984) in relating the index of dryness (D) with both surface albedo (α) and surface water availability (w) as follows:

$$w = 1.23\frac{\tanh D}{D} - 0.33 \qquad D \geq 0, \tag{4.13}$$

and

$$\alpha = \begin{cases} \min(0.25, 0.07 + 0.06D) & D \geq 1, \\ 0.10 & 0 < D < 1. \end{cases} \tag{4.14}$$

Note that within the tropical forest region (defined as $0 < D < 1$), there is no dependence of the surface albedo on the dryness index. On the other hand, the upper limit of the surface albedo is set to 0.25 which is reasonable for deserts. The surface water availability is prescribed to be close to 1.0 (moist surface) in the forest region, and approaches 0.0 as D increases in the desert and semi-desert regions.

This simple land surface scheme basically uses the dryness index D as an indicator of vegetation types. A distribution of D corresponds to a particular vegetation distribution, giving us a unique distribution of surface albedo and a unique distribution of water availability. Hence, for a given vegetation distribution we know how much of the solar insolation is absorbed at the surface (through surface albedo), and how much the surface net radiation is partitioned between latent heat flux and sensible heat flux. This is done through water availability w. The actual evaporation is defined as $w \times E_p$, where E_p is the potential surface evaporation calculated by the bulk formula as defined in Chapter 2.

4.4   Sensitivity of the West African Monsoon to the Meridional Distribution of Vegetation

In the previous sections we argued that the dynamics of monsoons are regulated by the meridional distribution of boundary layer entropy. Since any change of land cover is necessarily associated with changes in surface albedo, surface water availability (root zone depth), as well as surface roughness; the net surface radiative flux and the entropy flux from the underlying surface will change correspondingly (Eltahir,

1996). Therefore, any land cover transformation is likely to have substantial effects on boundary layer entropy and thus the monsoon circulation. Here, we would like to investigate this issue and examine the sensitivity of West African monsoons to changes in vegetation that may occur at different latitudinal belts. Our approach consists of numerical experiments using the model described above. Four primary experiments were performed and will be discussed in the following subsections.

4.4.1 Control Experiment

The natural vegetation in West Africa ranges from short grass at the desert border to humid rain forests at the southern border of the region near the Atlantic coast. The area in between is occupied by several vegetation zones ranging from tropical forests, to woodland, savanna, shrubs, and short grass. The vegetation pattern in terms of the index of dryness (D) for the control experiment is specified in Figure 4.12a. Also in Figure 4.12 we show the vegetation perturbations that will be discussed later. For the area between the coast (5°N) to 10°N, we assign a D value of 0.50 which corresponds to tropical forests; north of 20°N, D is set to 3.0 implying a surface albedo of 0.25 which corresponds to desert conditions. The dryness index is assumed to increase linearly between 10°N to 20°N to represent the transition from the tropical forest conditions to the desert conditions. The corresponding patterns of surface albedo and water availability are described in Figure 4.13 and Figure 4.14.

For the sake of simplicity, we are going to concentrate on the perpetual summer case[3]. The solar insolation of August 15 is assumed in these experiments; this date coincides approximately with the period of the observed maximum precipitation in West Africa. The oceanic temperature is specified as the observed mean SST distribution in August (climatology 1981-1994) off the West African coast (Reynolds, R.W., 1988; Reynolds, R.W. and D.C. Marsico, 1993; Reynolds, R.W. and T.M. Smith,

---

[3]In the Appendix B, we repeat some of the main experiments here using the model with a seasonal cycle, which will be described in Chapter 5.
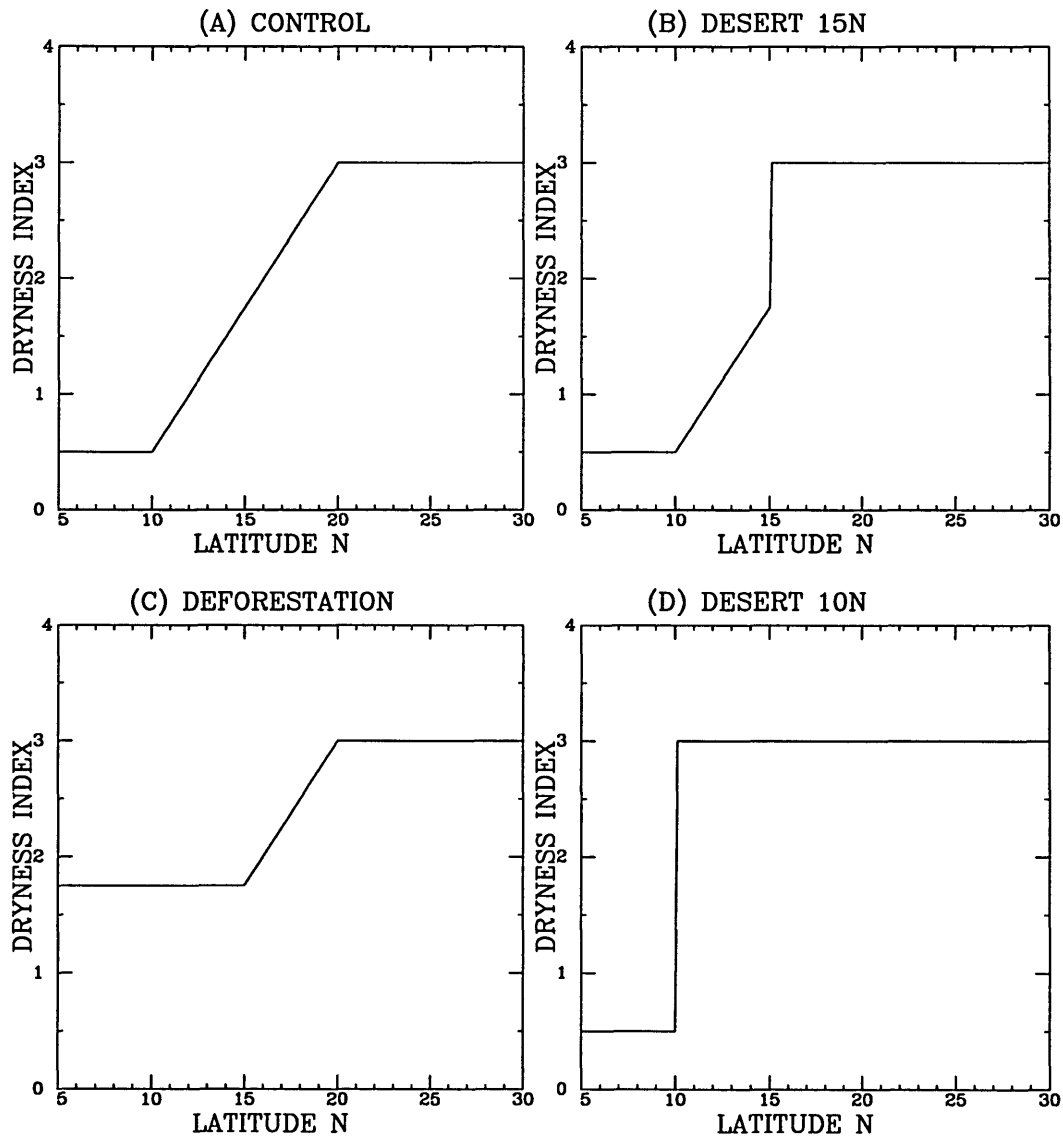
Figure 4.12: The distribution of vegetation (described by the dryness index): (a) for the control experiment, (b) the desertification (from 15°N) experiment, (c) the deforestation experiment, and (d) the desertification (from 10°N) experiment.
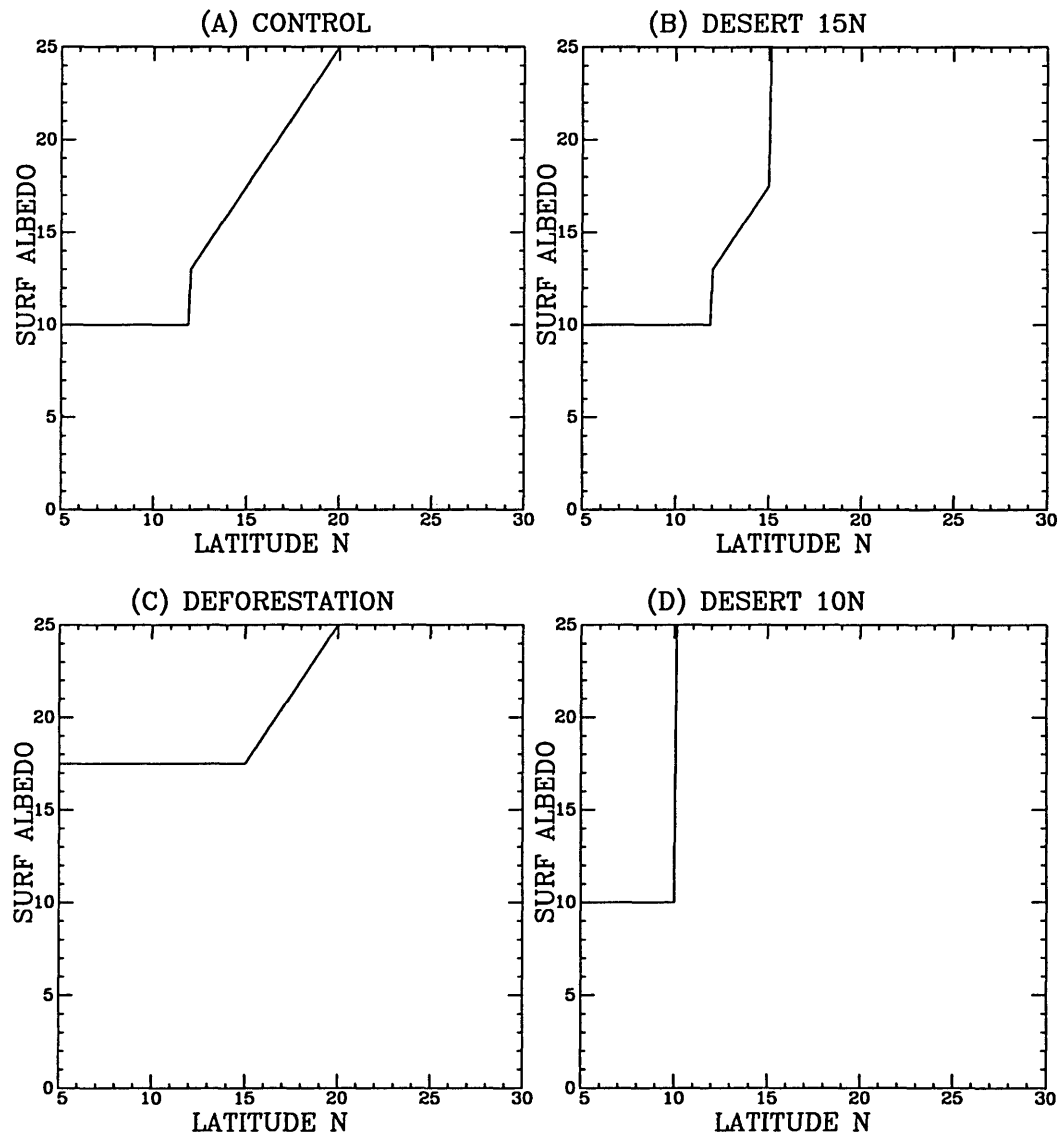
Figure 4.13: The distribution of surface albedo in percentage: (a) for the control experiment, (b) the desertification (from 15°N) experiment, (c) the deforestation experiment, and (d) the desertification (from 10°N) experiment.
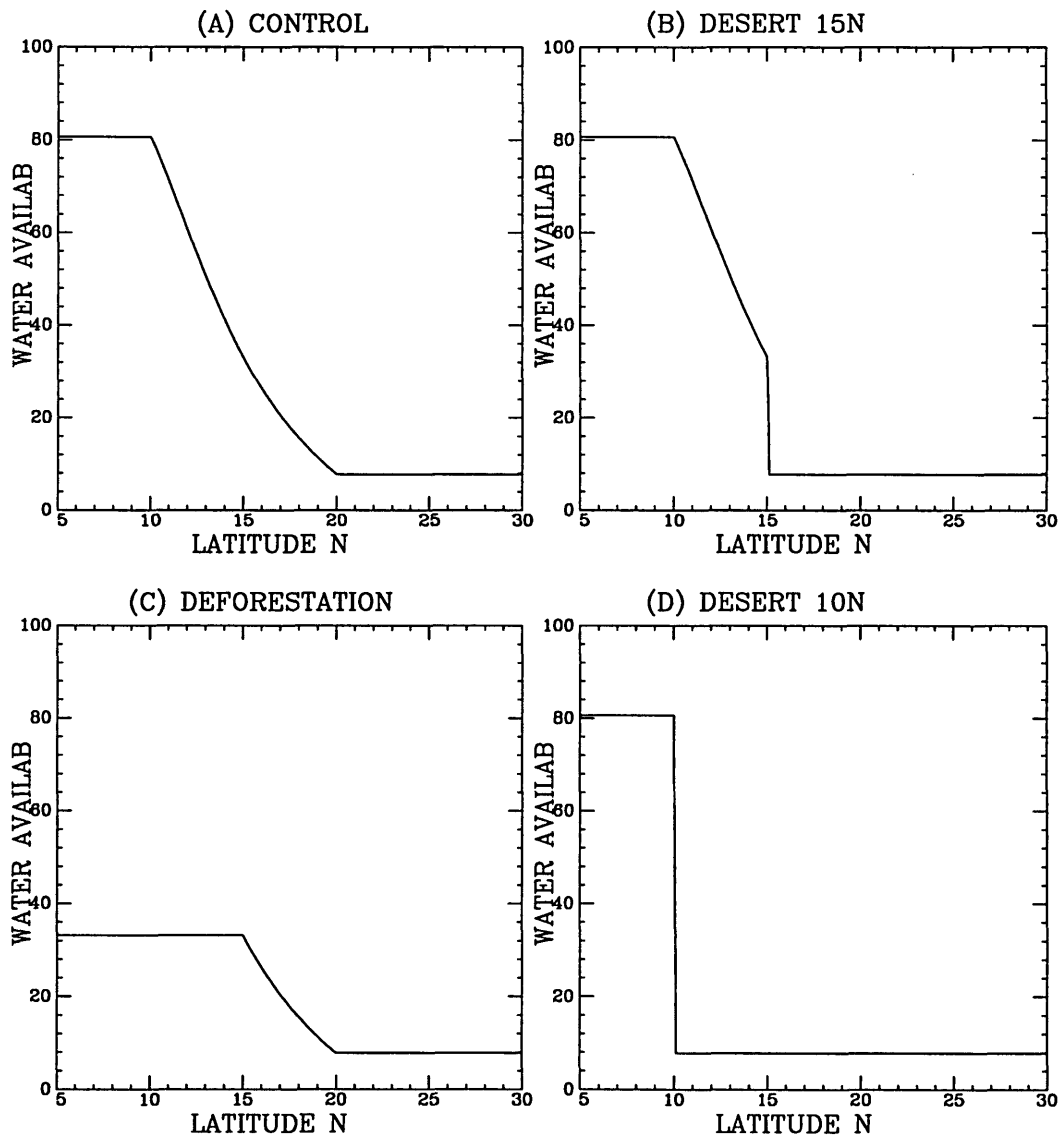
Figure 4.14: The distribution of surface water availability in percentage: (a) for the control experiment, (b) the desertification (from 15°N) experiment, (a) the deforestation experiment, and (d) the desertification (from 10°N) experiment.

1994). The model is integrated for 500 days to achieve a quasi-steady state. Hence, the numerical simulations discussed here describe the steady state solutions for the dynamics of monsoons that correspond to different surface boundary conditions, but using the same solar forcing.
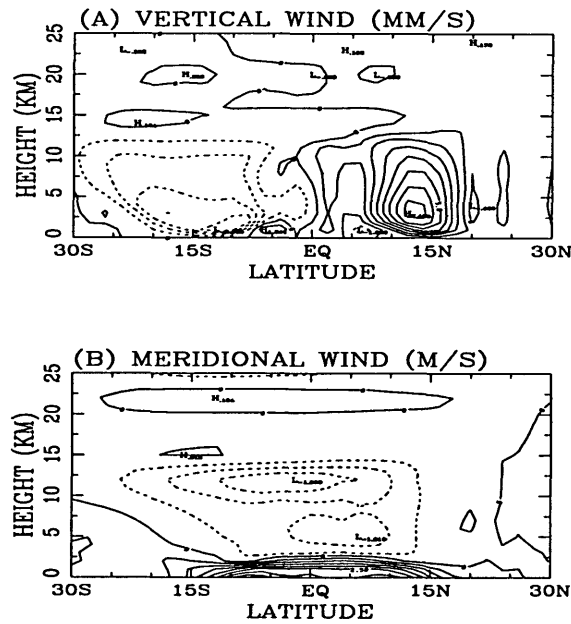
Figure 4.15: The vertical wind (contour interval 1 mms⁻¹) and meridional wind (contour interval 0.5 ms⁻¹) of the control circulation.

The results of the control experiment indicate a development of a healthy monsoon circulation. Figure 4.15 displays the vertical and meridional components of the monsoon circulation. A clear thermally-direct circulation is observed, consistent with the notion we discussed in Section 1.2. Figure 4.16a shows the distribution of absolute and planetary vorticities at the tropopause. While the inviscid theory predicts zero absolute vorticity at the tropopause, the model shows effective weakening of the absolute vorticity from about 25°S to 15°N. A slight nonconservation of angular momentum is implied by non-zero absolute vorticity within the region, presumably due to the inclusion of the numerical diffusion. The meridional distributions of total rainfall, evaporation and $P - E$ (P total rainfall, E evaporation, this is a measure of large

scale moisture convergence) are shown in Figure 4.17, Figure 4.18 and Figure 4.19 resectively. The maximum precipitation occurs at a latitude between 12°N to 13°N where $P - E$ also maximizes. This latitude coincides with the location of maximum vertical wind (Fig. 4.15a) as well. Although the control experiment we describe here cannot be compared with the observed August rainfall exactly (where August is just part of the seasonal cycle), the location of ITCZ[4] is not very far from the reality ($\sim$ 10°N-12°N, see Figure 5.22). The latitude of the maximum evaporation (Fig. 4.18), however, is south of the ITCZ at around 8°N to 10°N. This is due to larger surface water availability near the coastal region as shown in Figure 4.14. The meridional distribution of boundary layer entropy is shown in Figure 4.20. Note that the latitude of maximum boundary layer entropy (about 22°N) is far north of the latitude of maximum rainfall. The latitude of maximum boundary layer entropy can be viewed as the northern boundary of the monsoon circulation since this is where angular momentum contour becomes vertical (Emanuel, 1995). In addition, the results that are not presented here show a strong easterly jet at upper levels, and a surface westerly flow over the land. The same results show westerly jets in both hemispheres with a much stronger winter jet. The intensity of these jets is unrealistically strong since we use a zonally-symmetric model. In reality, mid-latitudinal eddies would tend to reduce the intensity of these jets. Overall, these features are consistent with the development of a healthy monsoon (Ramage, 1971).

4.4.2   Desertification (from 15°N) Experiment

This experiment is identical to the control experiment except that the vegetative cover in the region between 15°N to 20°N is removed resulting in expansion of the desert (see Fig. 4.12b). This change in the surface boundary mimics the desertification of the semi-arid region that is located to the south of the Sahara desert, and is similar to the case considered by Charney (1975) and several other studies.

---

[4]ITCZ here is defined as the location of the maximum rainfall.

98
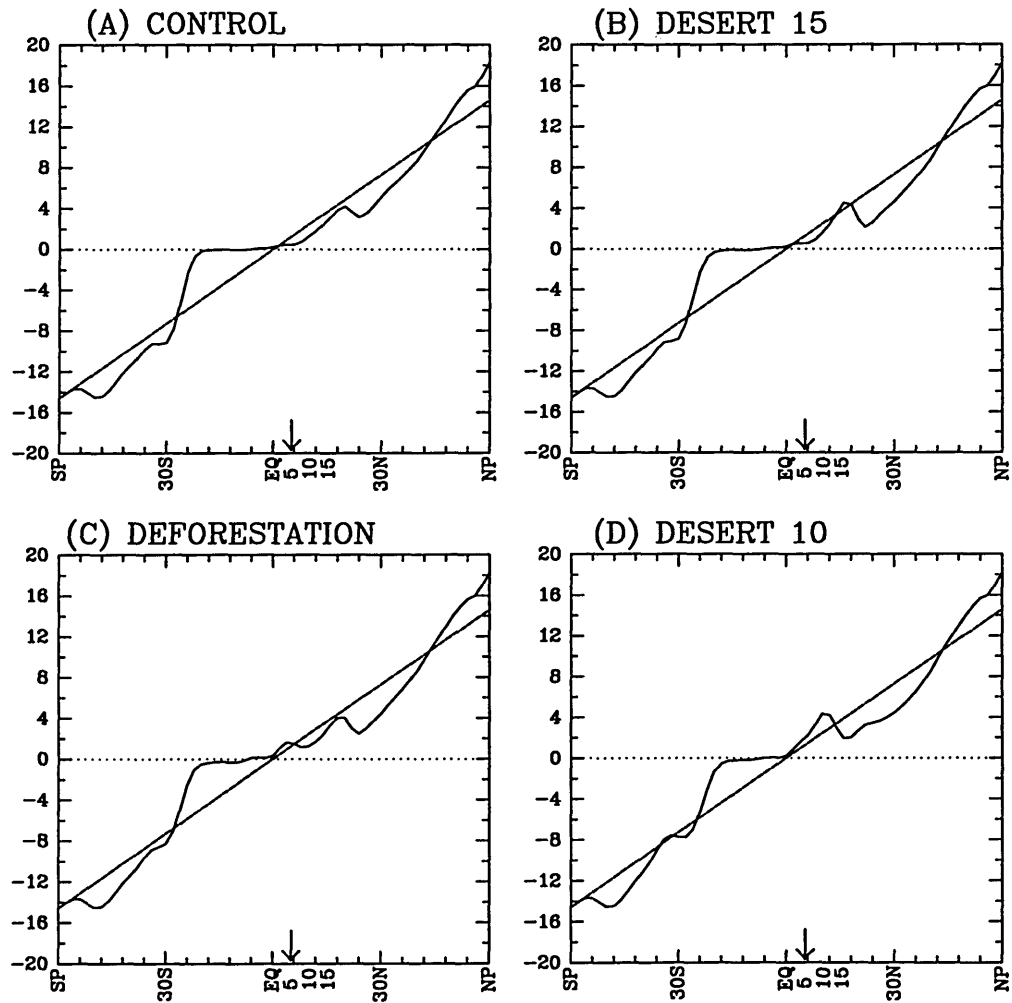
Figure 4.16: The absolute (solid) and planetary (dashed) vorticities (unit 10^{-5}s^{-1}) at the tropopause for (a) control, (b) desertification (from 15°N), (c) deforestation, and (d) desertification (from 10°N). The vertical arrow indicates the coastline of the southern Atlantic Ocean.

Figure 4.17: The meridional distribution of rainfall in (mm/day), for the control (solid line), desertification from 15°N (dashed line), deforestation (dashed-dotted line) and desertification from 10°N (dotted line).

Figure 4.18: The meridional distribution of evaporation in (mm/day), for the control (solid line), desertification from 15°N (dashed line), deforestation (dashed-dotted line) and desertification from 10°N (dotted line).
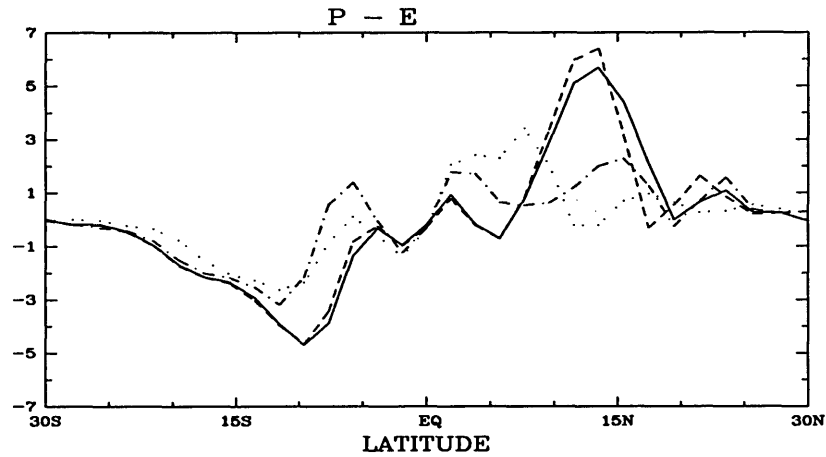
Figure 4.19: The meridional distribution of the difference between precipitation and evaporation $(P - E)$ in (mm/day) for control (solid line), desertification from 15°N (dashed line), deforestation (dashed-dotted line) and desertification from 10°N (dotted line).
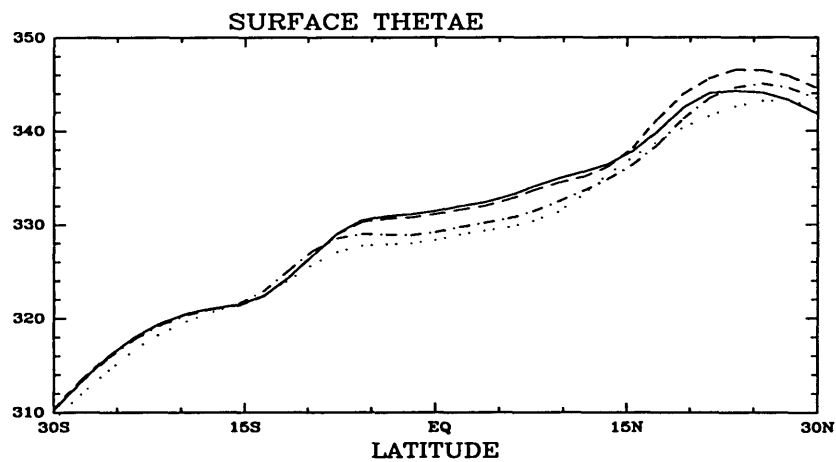
Figure 4.20: Boundary layer entropy in terms of surface θ_e in Kelvin for the control (solid line), desertification from 15°N (dashed line), deforestation (dashed-dotted line) and desertification from 10°N (dotted line).
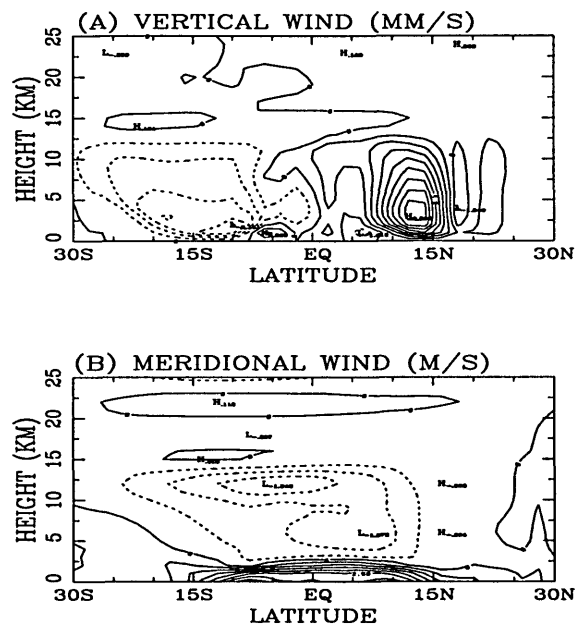
Figure 4.21: The vertical wind (contour interval 1 mms^{-1}) and meridional wind (contour interval 0.5 ms^{-1}) of the desertification from (15°N) experiment.

Even with the desertification in the semi-arid region, the monsoon circulation still exists and strong. This can be seen from Figure 4.21. The distribution of upper-level absolute vorticity in Figure 4.16b indicates that the north edge (about 12°N) of the weakened absolute vorticity region is slightly south of the corresponding location of the control experiment. The latitudinal profile of rainfall in Figure 4.17 shows that the rainfall decreases substantially within the perturbation region (from 15°N to 20°N). This is due to both the decrease of moisture convergence and the decrease of the local evaporation. However, south of 15°N, rainfall even increases. The increase of rainfall south of the perturbation region is mainly associated with the increase of the large-scale moisture convergence which is consistent with the stronger and more concentrated monsoon updraft, as can be seen from Fig. 4.19. Furthermore, the location of the maximum rainfall of Figure 4.17, and hence ITCZ, does not change significantly following the desertification. The ITCZ seems to be more concentrated following the desertification. A surface westerly wind (not shown) also develops over

the land with similar magnitude to that of the control case (comparing Fig. 4.15 with Fig. 4.21). In summary, the desertification near the southern edge of the desert reduces the rainfall within the desertification region and enhances the rainfall south of it. However, the resulting modification of the circulation is not significant enough for the monsoon to collapse.

4.4.3 Deforestation Experiment

This experiment is identical to the control case except that the vegetative cover for the region 5°N to 15°N is replaced by savanna with the dryness index value at 15°N (see Fig. 4.12c). In the control experiment, this region is covered by tropical forest between 5°N to 10°N and by savanna for the subregion between 10°N to 15°N. This experiment attempts to simulate the worst case scenario for tropical deforestation in West Africa.

Unlike the desertification experiment, the influence of the deforestation is dramatic. The maximum rainfall ($\sim$ 5 mm/day) is only half of the control experiment (Fig. 4.17). In addition, the moisture convergence (which is a measure of the strength of the monsoon circulation) is only one-third of the value in the control case, implying a much weaker circulation (Fig. 4.19). In accordance with this, the upper level absolute vorticity is no longer close to zero over the land (Fig. 4.16c), indicating the collapse of the nonlinear monsoon circulation. The collapse of the monsoon can be explained as follows. Figure 4.22 shows the net surface radiative fluxes. It is clear that within the perturbation region the net radiative flux is much smaller than that of the control case (about 40 Wm^{-2}). This reduction in net surface radiation results in a similar reduction of surface entropy flux for the coastal region, hence reducing substantially the boundary layer entropy there. The total surface heat flux, which equals the net radiative flux over the land, is displayed in Figure 4.23. The reduction of the surface heat flux over the land results in the gradient of boundary layer entropy between land and ocean being too weak to trigger a monsoon circulation. Therefore,

the monsoon collapses.
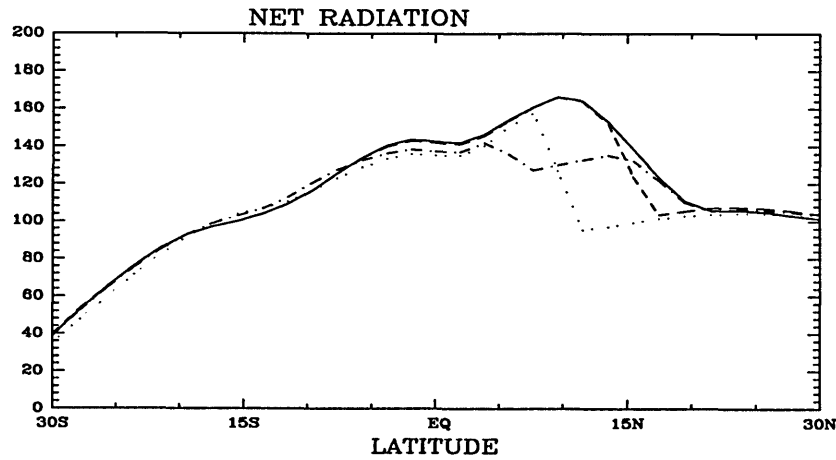
Figure 4.22: The same as Figure 4.20 except for net surface radiation (Wm^{-2}).
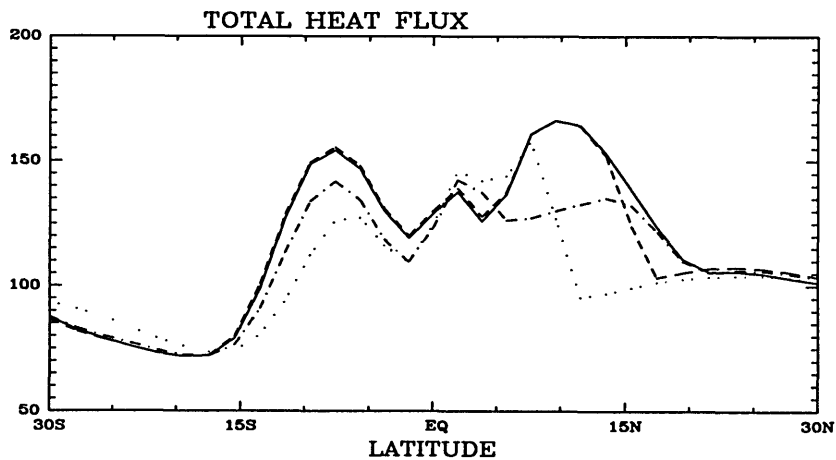
Figure 4.23: The total surface fluxes (Wm^{-2}) for the control (solid line), desertification from 15°N (dashed line), deforestation (dashed-dotted line) and desertification from 10°N (dotted line).

In general, the degradation of the vegetative cover will induce increase of albedo (Fig. 4.13) and decrease of surface water availability (Fig. 4.14). The increase of the surface albedo will decrease the surface solar radiative flux. On the other hand, the decrease of the surface water availability has the tendency of heating up the land surface. This results in larger outgoing longwave radiative flux (other things being

the same). In addition, the decrease of the surface water availability also reduces the surface evaporation. This introduces less water vapor in the atmosphere and a smaller greenhouse effect. The combination of the two effects induced by smaller surface water availability produces a net increase of the upward outgoing longwave radiative flux. Therefore, the overall effects of both shortwave and longwave radiative components arising from the degradation of the vegetative cover lead to a net decrease of the net surface radiation.

Another experiment was performed to isolate the relative roles of albedo and water availability changes. This experiment is identical to the standard deforestation experiment we just described in surface albedo but the water availability is fixed to that of the control experiment. The net surface radiative flux for this experiment is compared to those of the standard deforestation experiment and the control experiment (Fig. 4.24). The difference between this experiment and the control state is the net effect of the increasing surface albedo whereas the difference between this experiment and the standard deforestation experiment indicates the net effect of the decreasing surface water availability. In terms of the relative contribution to the net surface radiation, we see that the effect of the surface moisture availability is substantial, although slightly smaller than the albedo effect here. The effect of decreasing surface water availability can be explained almost completely by the longwave component whereas the effect of increasing surface albedo is responsible for the shortwave component (Fig. 4.25 and Fig. 4.26). The model result confirms our conceptual reasoning presented earlier.

Figure 4.27 and Figure 4.28 show the surface net solar radiative flux (downward) and net upward terrestrial (longwave) radiative flux for the four standard experiments. For the case of deforestation, we see that both shortwave and longwave components contribute to the decreased net surface radiation comparably. The surface albedo contributes mainly to the solar part of the net radiation whereas the surface water availability is mostly responsible for the longwave component of the net radiation.
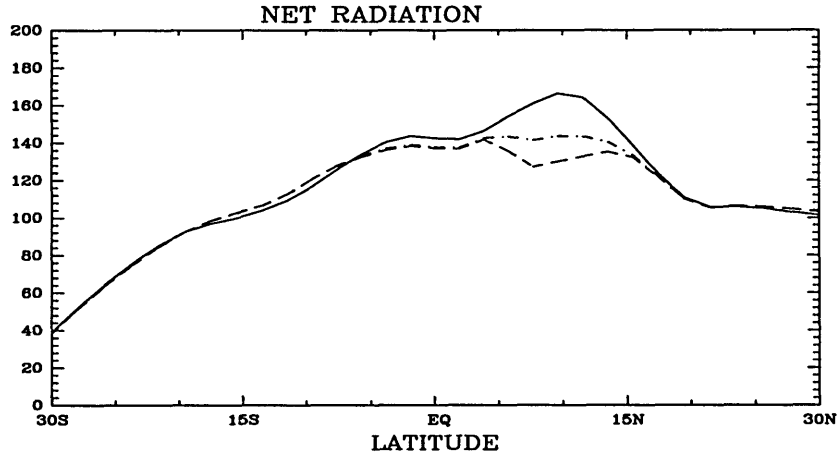
NET RADIATION

Figure 4.24: The surface net radiation (Wm^{-2}) for the control (solid line), deforestation (dashed line) and the experiment with the same surface albedo as the deforestation experiment and the same surface water availability as the control case.

NET LW RAD
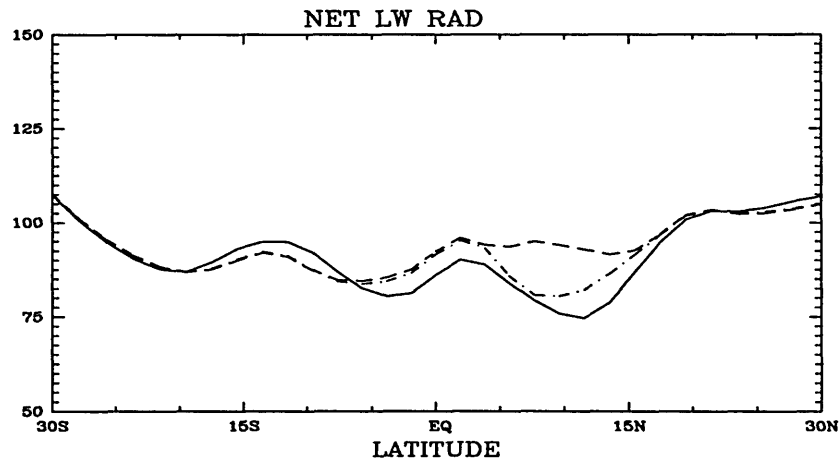
Figure 4.25: The same as Figure 4.24 but for the surface upward longwave radiation.
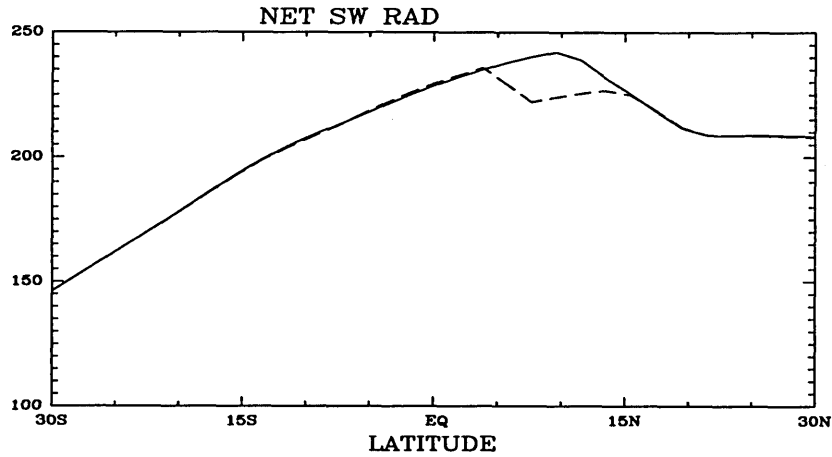
Figure 4.26: The same as Figure 4.24 but for the surface downward shortwave radiation. Note that the standard deforestation experiment and our hypothetical experiment here have indistinguishable surface downward solar radiation due to identical albedo.
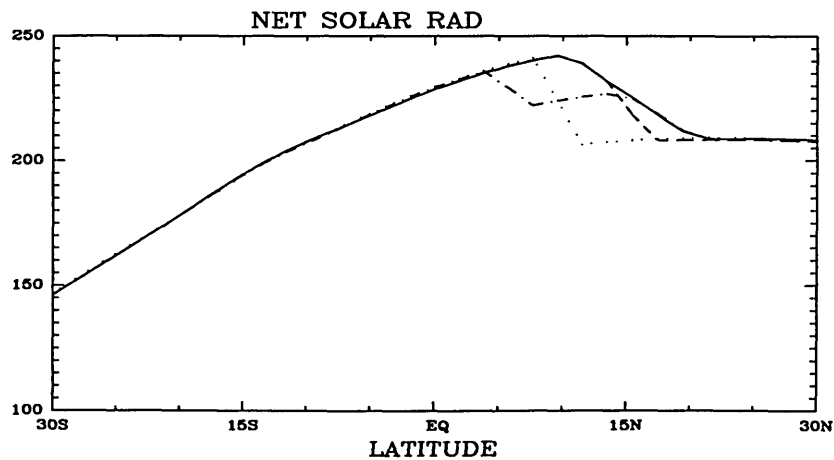
Figure 4.27: The net surface shortwave radiative flux (downward, Wm^{-2}) for the control (solid line), desertification (from 15°N, dashed line), deforestation (dashed-dotted line) and desertification (from 10°N, dotted line).
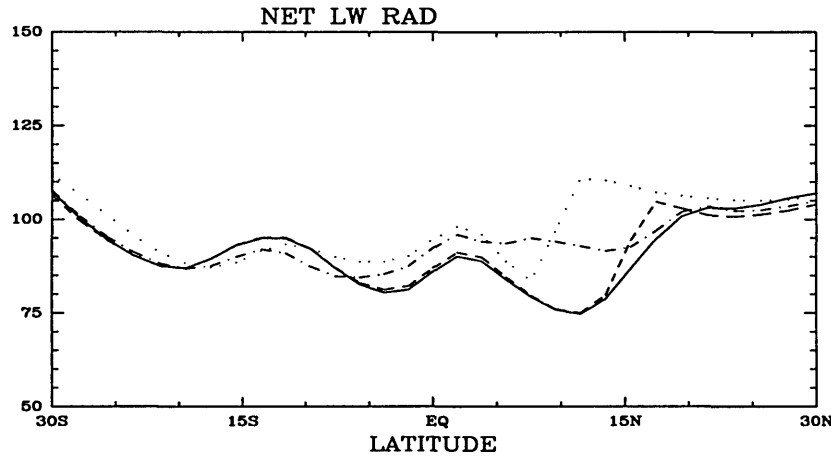
Figure 4.28: The net surface longwave radiative flux (upward, Wm^{-2}) for the control (solid line), desertification (from 15°N, dashed line), deforestation (dashed-dotted line) and desertification (from 10°N, dotted line).

4.4.4 Desertification (from 10°N) Experiment

The relation between the distribution of vegetation and the monsoon circulation is investigated further by considering the impact on the circulation that may result from desertification extending to 10°N. This experiment is identical to the control case except that we assign the value of the dryness index D to 3.0 (desert value) north of 10°N. As we can see from Figure 4.17, the maximum rainfall occurs over the coastal region between about 6°N to 8°N. Compared to both control and desertification (from 15°N) experiments, the rainfall belt (or ITCZ) has been pushed further south. The region of the perturbation experiences strong negative moisture convergence and evaporation anomalies, resulting in substantial decrease of rainfall over that region. South of the perturbation region, we observe an increase of rainfall caused mainly by the increase of moisture convergence, similar to the desertification (from 15°N) case. In terms of the rainfall within Sahel region ($\sim$ 12°N to 18°N), where most previous studies were concerned, this case introduces the most decrease compared to any other cases we described. The ITCZ stays over the coastal land and cannot move northward enough to bring rainfall to the Sahel region.

4.4.5 Other Experiments

The distribution of vegetation that is shown in Figure 4.12a is similar to the observed distribution over West Africa; the density of vegetative cover decreases from the south to the north. The areal extent of the three perturbations in vegetative cover are similar, each of them replaces the vegetative cover by a desert belt (for deforestation experiment, a savanna belt) that extends for about 10° latitude. However, due to the different densities of the vegetation that existed initially at the three different locations, the intensities of the three perturbations are different. For example, the desertification (from 15°N) in fact only replaces the vegetative cover of 5° in width (from 15°N to 20°N) by the desert. In order to test the robustness of our results, the same four experiments were repeated assuming that the distribution of vegetation in the control case is a uniform coverage by tropical forests (of course now the control case does not bear very much resemblance to reality). These results were not affected to any significant degree, i.e., the model response is still sensitive to the location of the vegetation perturbation.

Clearly the model's quantitative response to the vegetation perturbation has to do with the latitudinal width of the perturbation as well as the magnitude of the perturbation. Here we conduct two experiments which correspond to the standard deforestation and desertification (from 10°N) experiments (Fig. 4.12c and Fig. 4.12d) respectively. The only difference is that the areal extent of the perturbation now is 5° instead of 10°. For the deforestation experiment, the perturbation is from 5°N to 10°N (assigning dryness index the same as the standard deforestation experiment 1.75). For the desertification experiment, the perturbation is from 10°N to 15°N with all the vegetative cover replaced by desert (i.e., D = 3.0).

The total rainfall for experiments with perturbations of 5 degree latitudinal width is shown in Figure 4.29. The deforestation (from 5°N to 10°N) experiment still shows substantial decrease of rainfall everywhere over the land area. However, the magnitude of rainfall decrease is smaller compared to the standard deforestation (from 5°N

to 15°N) experiment. In this case, it seems that a somewhat weaker monsoon circulation still exists. The ITCZ is pushed slightly northward. The desertification (from 10°N to 15°N) experiment, on the other hand, shows a similar dramatic decrease of rainfall within the perturbation region. The ITCZ again is pushed southward to be around 6°N to 8°N.
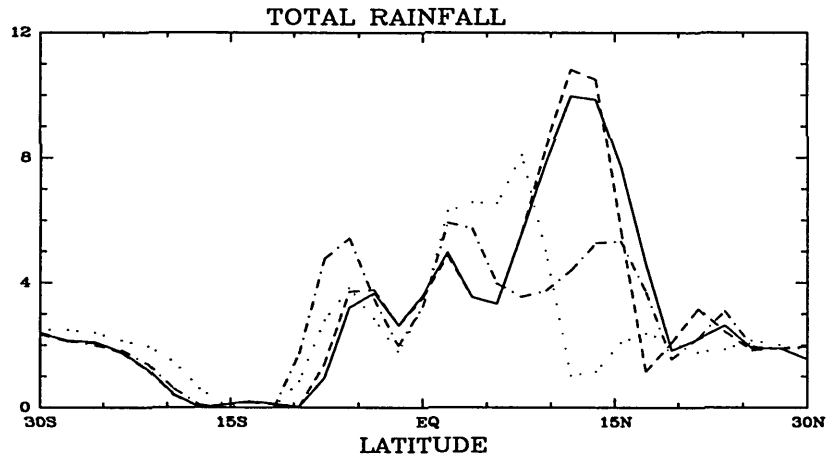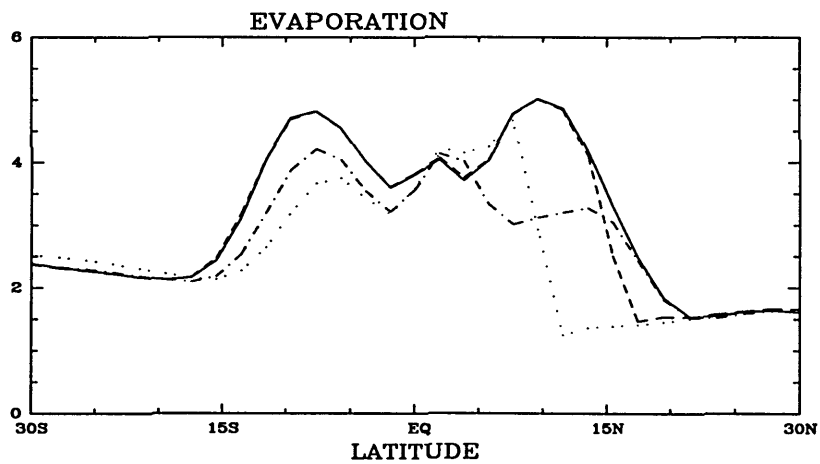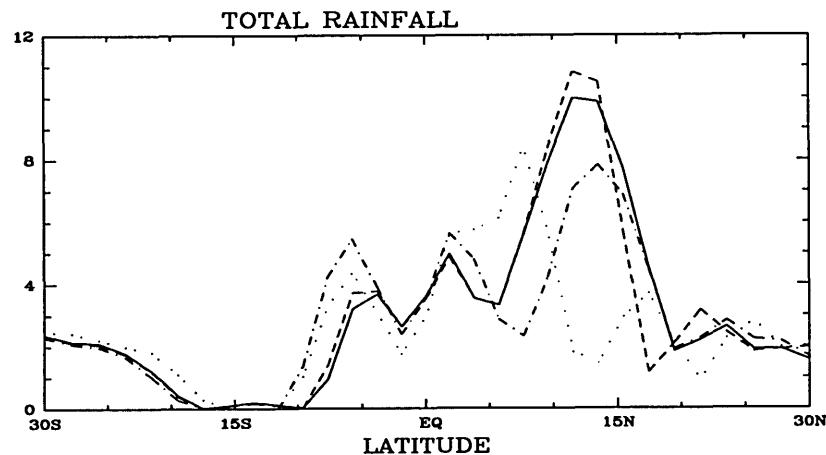

Figure 4.29: The meridional distribution of rainfall in (mm/day), for the control (solid line), desertification (from 15°N to 20°N, dashed line), deforestation (from 5°N to 10°N, dashed-dotted line) and desertification (from 10°N to 15°N, dotted line).

Other experiments using different magnitudes of vegetation perturbation have also been performed to examine the robustness of our results. Although quantitative differences exist as we expect, the experiments in general suggest that tropical deforestation is capable of producing substantial regional rainfall decrease over West Africa, just as the sub-Saharan desertification. In addition, it seems that the dynamics of West African monsoons are more susceptible to the vegetative cover near the tropical coastal region than that near the southern desert border. In what follows, we will summarize the results of the experiments we described and point out some important implications.

4.5   Discussion

The results of the numerical experiments of the previous section shed some light on the role of vegetation in the dynamics of West African monsoons. The vegetative cover along the coast of West Africa seems to be able to influence the simulated monsoons more significantly than vegetative cover near the desert border (north of 15°N). It is interesting to compare the response of the model to deforestation and desertification. Given the limitations of the model the results of this exercise should be interpreted carefully, especially in comparison with the dynamics in the real atmosphere. However, comparison of the results for the different cases considered suggests that the dynamics of the monsoon in this region is indeed more sensitive to changes in land cover that may occur along the coast (deforestation, Fig. 4.12a) than changes in land cover that occur at the desert border (desertification, Fig. 4.12b).

These results are particularly interesting if we consider them in conjunction with the observed patterns of land cover change in West Africa. This region has been experiencing very intense changes in land cover throughout this century. The nature of land cover change in West Africa varies from desertification at the northern border to deforestation at the southern border. These changes in land cover are driven primarily by the increase in population. The demand for agricultural land is satisfied by clearing of natural vegetation, and the quality of vegetation cover is degraded by overgrazing in several regions. The timber industry flourishes along the coast of the Atlantic Ocean at the expense of continuous clearing of vast areas of the humid forests. The dry woodlands are popular sources of wood for domestic use. The combination of all these factors drives some of the most intense changes of land cover compared to any other regions.

During the early years of this century, rain forests covered a significant area, about 500,000 square kilometers, along the Atlantic coast. Today, less than 10% of the primary rain forest is left, see Figure 4.30. These estimates of tropical deforestation in West Africa were reported in Gornitz (1985) and Myers (1991). The highest annual
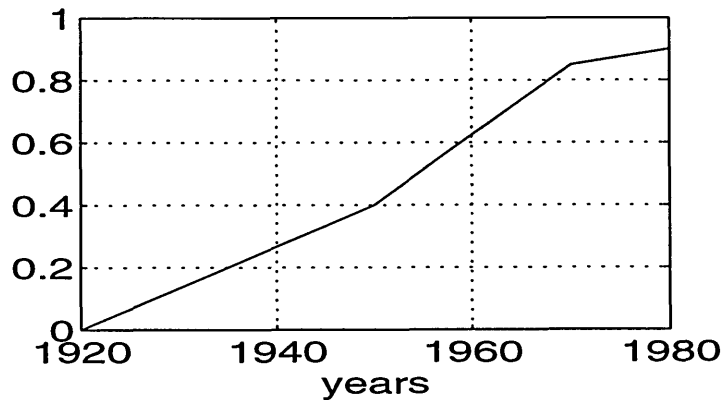
Figure 4.30: The time evolution of the ratio of the deforested area to the total area of the forest in 1920 ($\sim$ 500,000 km^2) in West Africa estimated based on the data reported by Gornitz (1985) and Myers (1991).

rates of deforestation are in the Ivory Coast, Nigeria, and Ghana. The study of Myers (1991) estimates that the current annual rate of deforestation is 16% for Ivory Coast and 14% in Nigeria. Indeed, these are the highest annual rates of deforestation in the world. These estimates led Myers (1991) to conclude that little primary forest is likely to be left in West Africa by about the year 2000.

Charney (1975) proposed a mechanism for describing the feedbacks between desertification and droughts. This theory is based on the basic concept that deserts work as radiative sinks of heat where the loss of heat due to the emission of planetary radiation is balanced by adiabatic warming due to subsidence. Under these conditions, removal of vegetation, such as that caused by overgrazing at the desert border, increases surface albedo causing an additional radiative cooling. The latter can only be balanced by additional adiabatic warming and enhancement of sinking motion. Charney (1975) argued that this enhancement of the sinking motion could push the ITCZ southward. While our simulations for the desertification show anomalous sinking motion, the decrease of rainfall over the new desert is associated with changes in $P - E$ (circulation change), and a decrease in evaporation (local effect),

see Figure 4.17, Figure 4.18 and Figure 4.19. These kind of feedbacks cannot be addressed in the dry model of Charney (1975).

The same classical paper by Charney (1975) argues that *"To my knowledge we do not yet have an explanation for the location of the ITCZ over the African continent, nor do we understand the nature of its interaction with the desert circulation"*. However, the simulations described in the previous section may throw some light on the dynamics of the monsoon circulation, and the factors that govern the movement of the ITCZ onto the African continent. These results suggest that the distribution of vegetation may play a significant role in these processes. In particular, the type of vegetation that occupies the coastal region is important to the movement of the ITCZ onto the African continent. The mechanism by which vegetation in this zone interacts with the atmospheric circulation can be described by the theory of Eltahir (1996). Vegetation in the form of dense forests enhances net radiation at the surface, and the total flux of heat including sensible and latent forms. These fluxes supply energy as well as entropy in the boundary layer, and create a significant gradient of entropy between land and ocean. The theory mentioned in Chapter 1 describes how this gradient is critical to the dynamics of monsoons. The deforestation experiment illustrates how the removal of this vegetation would weaken the meridional gradient of the boundary layer entropy between land and ocean and thus weaken the monsoon circulation and cause less rainfall over West Africa. For some extreme cases, like the vegetation perturbation we assumed in Figure 4.12c, the monsoon can collapse as shown in Figure 4.17. Figure 4.22 indicates that the radiative flux (therefore the entropy flux) decreases substantially over the perturbed region. For the case of the deforestation from 5°N to 15°N, the total heat flux over the coastal region happens to be smaller than the oceanic value causing the collapse of the monsoon.

A comparison of the results of the four primary numerical experiments would suggest that the location of the simulated ITCZ is rather insensitive to the distribution of vegetation northward (to a lesser extent southward) relative to the location of ITCZ

in the control experiment. In the desertification (from 15°N) experiment, although the magnitude of local rainfall is reduced relative to the control case, the location of ITCZ does not change significantly compared to the control case. The same can be said to the deforestation (from 5°N to 10°N) experiment. However, in the other experiments which involved changes in vegetation distribution within the vicinity of the ITCZ in the control experiment, the location of the ITCZ changes dramatically. This has important implications for GCM studies regarding effects of land surface transformation on the location of the ITCZ. That is that, the response of different models to the same specified vegetation perturbation (e.g., desertification, which is the topic for most previous studies) might be different simply because different models have different control states. In general, for sub-Saharan desertification (degradation of the vegetative cover starts from the desert border southward), if the ITCZ for the control experiment lies within the region of perturbation, we expect a southward shift of the ITCZ as in the desertification (from 10°N) experiment. On the other hand, if the region of perturbation lies north of the ITCZ for the control case, we do not expect substantial change of the ITCZ position as in the desertification (from 15°N) experiment we have shown above. As far as deforestation (degradation of the vegetative cover starts from the coast northward) is concerned, the deforestation from 5°N to 10°N has a tendency of pushing ITCZ northward but not significant. For the worst scenario of deforestation (from 5°N to 15°N), monsoon collapses. The dynamics of West African monsoons seem to depend more on the vegetative cover from the location of the ITCZ (for the control run) southward than that from the location of the ITCZ (for the control run) northward. This again is consistent with the notion that the gradient of boundary layer entropy (which regulates the monsoon circulation) cares more about the vegetative cover closer to the coast line and less about the vegetative cover further inland.

In particular, we have shown that the tropical deforestation may be a potentially important factor in modulating the West African rainfall variabilities. This study

suggests that the tropical deforestation may be another possible drought mechanism in West Africa besides the well documented sub-Saharan desertification proposed first by Charney (1975). From Figure 4.1, 1950-1969 were relatively wet years in Sahel and 1970-1990 were relatively dry years. From the data of Nicholson (1994), we plot out the latitudinal distribution of normalized rainfall departures in West Africa for the dry (1970-1990) and wet (1950-1969) periods. It is very clear that for the period of 1970-1990 the rainfall is relatively low compared to the period 1950-1969 over the whole West Africa (Fig. 4.31). If the actual rainfall variability has anything to do with the land surface transformation (which may not be the case since SST could be another factor among others), Figure 4.31 favors the deforestation since the effect of desertification on West African rainfall presents a dipole pattern (positive deviation south of the perturbation region and negative within the perturbation region, see Fig. 4.17) whereas the deforestation creates a universal negative deviation over the whole of West Africa.
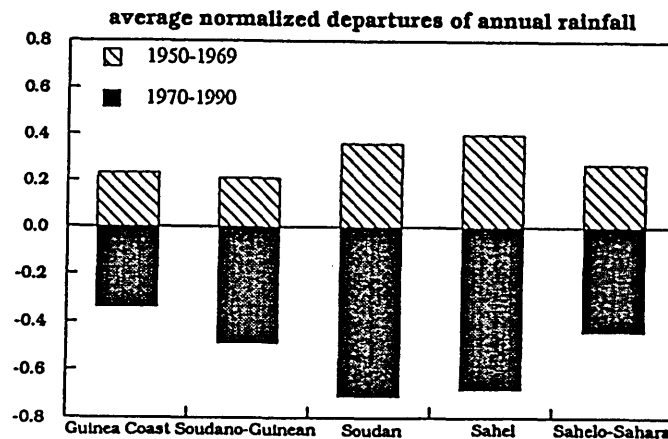
Figure 4.31: The normalized annual departures of African rainfall averaged for periods 1950-1969 and 1970-1990 for different West African regions. The five regions are Guinea Coast (5), Soudano-Guinean (4), Soudan (3), Sahel (2) and Sahelo-Sahara, as defined in Nicholson (1994).

Furthermore, the basic difference between desertification near the desert border and deforestation near the coastal region is that the regrowth of grass is much easier than the regrowth of forest. While human activities (such as overgrazing) may easily cause desertification near the desert border, the natural variability of the whole climate system makes the recovery of the grassland possible by bringing more rainfall (for other reasons). The time scale to regrow the grassland is on the order of months. This implies that it is unlikely that the desertification is responsible for the long-lasting (decades) deficient rainfall over the Sahel. On the other hand, the tropical forest, once it is deforested, is much harder to recover. The time scale for recovery is of years to a decade. Therefore, it is more likely that the tropical deforestation may be responsible for the long-term rainfall variability, such as the decadal time scale drought near the Sahel region.

We have to warn that there is little empirical evidence regarding the effect of land cover transformation on the West African monsoons (Nicholson, 1988). Most studies of West African monsoons on land cover modification are based on models. In order to get significant response due to land cover change, large perturbation of the land surface properties (e.g., surface albedo) has been assumed. The magnitude of the perturbation is very often unjustified. This is the main caveat of all the modeling studies (including this study). Nevertheless, this study shows the critical importance of the location of the vegetation perturbation in the dynamics of West African monsoons.

4.6 Summary

From the discussion we presented above, we can conclude:

(1). Several numerical experiments were performed using a zonally-symmetric model of the atmosphere with the vegetation distribution described by a simple parameterization. The objective of these experiments is to investigate the role of vegetation

distribution in the atmospheric dynamics of West African monsoons and to determine how the atmosphere responds to changes in the lower boundary conditions. The results of the experiments suggest that the meridional distribution of vegetation plays a significant role in the dynamics of West African monsoons. The response of the atmosphere to any perturbation in the distribution of vegetation depends critically on the location of this perturbation.

(2). Changes in vegetative cover along the border between the Sahara desert and West Africa (desertification) leave a minor impact on the simulated monsoon circulation. These changes merely reduce the amount of rainfall at the desert border, but a healthy monsoon circulation still develops over the region.

(3). Changes in vegetative cover along the southern coast of West Africa (deforestation) could have a dramatic impact on the simulated atmospheric response. Deforestation excites a significant response in the model atmosphere and results in the collapse of the monsoon circulation for the worst case scenario. The physics of this response can be described by the mechanism of Eltahir (1996) with deforestation resulting in reducing surface net radiation, total flux of heat from the surface, and hence reducing boundary layer entropy. The response of the simulated monsoon circulation to the reduction of boundary layer entropy is consistent with the observations and theories of Eltahir and Gong (1996), Plumb and Hou (1992), and Emanuel (1995). The coastal deforestation is suggested as another drought mechanism of West Africa besides well-documented desertification.

(4). While the magnitude of local rainfall is sensitive to changes in local vegetation, the location of the ITCZ is not sensitive to changes in the vegetation northward or southward from the location of the ITCZ (control case). However, the location of the ITCZ is sensitive to changes of the vegetation distribution in the immediate vicinity of the location of the ITCZ (control case).

(5). The results of the numerical simulations shed some light on the relation between the dynamics of West African monsoons and the distribution of vegetation. However,

extension of these results to describe the response of the real atmosphere to changes in the distribution of vegetation should be approached carefully due to the limitations of this simple model. In particular, the model was not designed to simulate the three dimensional aspects of the relevant atmospheric dynamics, and does not treat the less understood processes regarding cloud feedbacks. Some of our future research will focus on these important issues.

Chapter 5

The Influence of Spring SST Anomalies on West African Rainfall

5.1 Introduction

West Africa, especially the Sahel region, experienced a long episode of deficient rainfall from late 1960s until recently (e.g., Nicholson and Palao, 1993, see Fig. 4.1). Whether or not this trend will continue remains to be seen. In 1994, the West African Sahel region observed the wettest year since 1969. Although the 1994 rainfall in the Sahel is only slightly above the long-term climatology (1901-1994), 1994 is still a year worthy of investigation (Nicholson *et al.*, 1996). On the other hand, 1992 is the driest year in West Africa in the 1990s. Here we would like to compare these two relatively close years and investigate possible reasons behind the interannual variability of West African rainfall.

The investigation of interannual variability of the West African (Sahelian in particular) rainfall in general consists of two groups of studies, i.e., the local land forcing (Chapter 4 belongs to this group) and the remote oceanic forcing (mainly the

tropical Atlantic SST). The land forcing includes changes of land surface boundary conditions, such as surface albedo and soil moisture level. The pioneering study on land-atmosphere interaction in West Africa is that of Charney (1975), which presented a hypothesis for describing the mechanisms of droughts. This study, along with other subsequent ones (e.g., Charney *et al.*, 1975; Charney *et al.*, 1977; Cunnington and Rowntree, 1986; Walker and Rowntree, 1977; Xue and Shukla, 1993; Yeh *et al.*, 1977), suggests that the local land surface forcing may play an important role in the dynamics of West African monsoon and rainfall. Our study in Chapter 4 suggests another possible mechanism of the African drought, i.e., tropical West African deforestation. It is worth noting that for studies of the effects of land surface transformations (e.g., deforestation and desertification) on West African rainfall variability, most of them are modeling efforts (which is, however, the only way to identify mechanisms). There is very little empirical evidence to support these modeling results, except the influence of local irrigation (Nicholson, 1988). One of the major reasons is that few measurements have been made of the changes of land surface properties (e.g., albedo, soil moisture) associated with land cover changes.

The second group of studies is concerned with the role of the ocean, and in particular the distribution of SST, in the regional climate over West Africa. The relation between the SST, especially the tropical Atlantic SST, and the Sahel rainfall has been the focus of several studies. At the regional scale, Lamb (1978a) presented a case study which shows that the deficient sub-Saharan summer rainfall is associated with warm summer (July-September) SST anomalies and vice versa. He further studied the composite large-scale tropical Atlantic surface circulation patterns associated with sub-Saharan dry and wet years (Lamb, 1978b). The dry composite shows negative SST anomalies during April-June and positive SST anomalies during July-September. In contrast to this, the wet composite displays positive SST anomalies during April-June and negative SST anomalies during July-September. His result is shown in Figure 5.1. A similar study by Lamb and Peppler (1992) basically con-

firmed the above results. Lough (1986) identified the dominant spatial patterns of normalized SST departures in the tropical Atlantic Ocean using principal component analysis, and then correlated these different patterns to the rainfall anomaly in the Sahel region. There are also numerous studies regarding the correlation between the Sahel rainfall and the global SST anomalies (e.g., Glantz *et al.*, 1991; Nicholson and Entekhabi, 1986; Semazzi *et al.*, 1988). All these statistical studies demonstrate that there is strong association between West African rainfall and SST both regionally and globally. However, most of the studies focus on the concurrent correlation between the summer rainfall and the summer SST and therefore do not elucidate any causal relations.

General circulation models (GCMs) have been used to investigate the impact of the regional and global SST anomalies on West African rainfall variations (Folland *et al.*, 1986; Druyan and Hasternrath, 1991; Owen and Folland, 1988; Palmer, 1986; Palmer *et al.*, 1992; Rowell *et al.*, 1992; Rowell, *et al.*, 1995). In particular, the study by Rowell *et al.* (1995) showed that the model they used was able to simulate the magnitude and pattern of the summer rainfall anomalies across tropical north Africa. In addition, global SST variations were shown to be responsible for most of the variability of the summer rainfall. All these model studies seem to have established a solid physical basis for the connection between SST and rainfall. However, GCMs are too complicated to study detailed physical mechanisms linking SST and Sahel rainfall.

While most statistical and modeling studies we discussed above are concerned with the simultaneous correlation between summer SST and summer rainfall, there have been attempts trying to predict the sub-Saharan rainfall from SST anomaly several months in advance (Lamb and Peppler, 1991; Parker *et al.*, 1988). Owen and Ward (1989) explored the possibility of forecasting the Sahel rainfall using spring SST observations by statistical methods. However, much remains to be understood about the physical links between spring SST and Sahel rainfall.
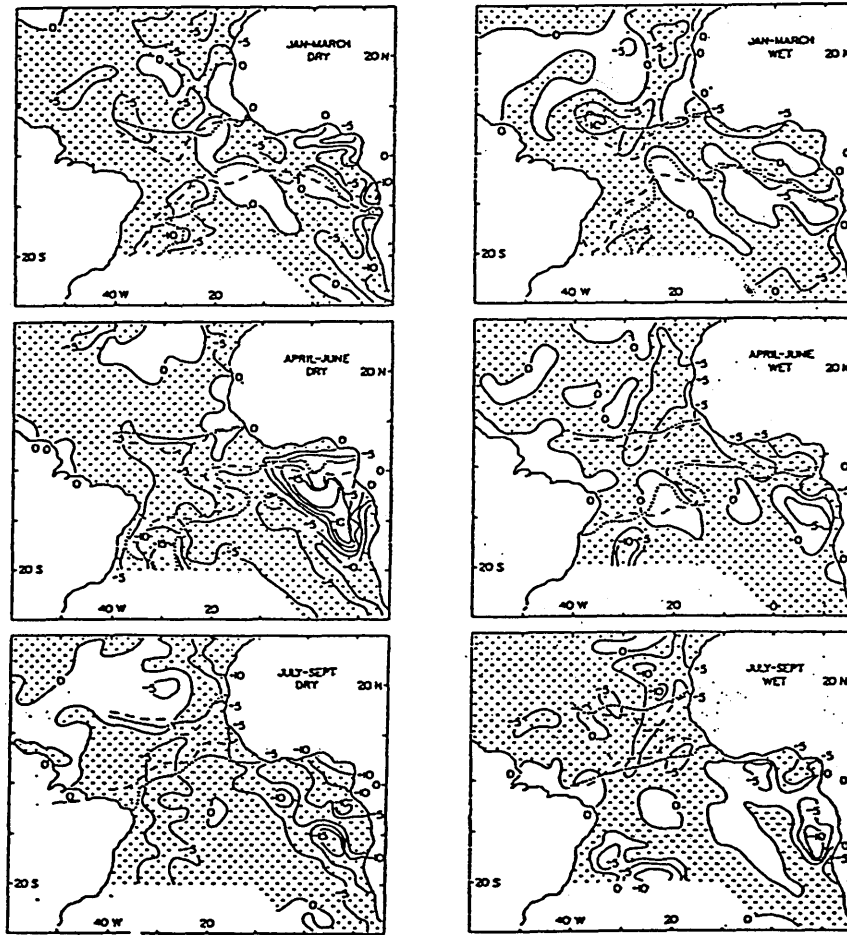
Figure 5.1: April-June and July-September SST anomaly fields for the dry (left side) and wet (right side) composites, expressed as departures from the 1911-1970 average patterns. Solid lines are departure isotherms (tenths of 1°C), positive values shaded; dotted lines enclose area of maximum SST east of 40°W (>27.2°C for April-June, >26.7°C for July-September), with broken lines doing likewise for the 1911-1970 mean, adopted from Lamb (1978b).

In general, both local land surface forcing and remote SST forcing are responsible for the Sahel rainfall variabilities. Besides these boundary forcings, other internal atmospheric variability may also play some role. The model we use here is two-dimensional and therefore does not include synoptic disturbances which are responsible for the internal atmospheric variabilities. However, as pointed out by Rowell *et al.* (1995), regarding the seasonal rainfall variability, the internal variability is secondary compared to the boundary layer forcing such as SST variability. Our goal here is to use our model to investigate mechanisms related to SST anomalies in the tropical Atlantic. We compare the recent extreme years of 1992 (dry) and 1994 (wet) first. Then from what the observations show, we hypothesize that the spring SST anomaly may be one of the important factors for the observed rainfall variability. While our model is too simple to simulate the real atmospheric variability, it does allow us to explore physical mechanisms in detail. The reasons to choose 1992 are as follows. First, 1992 is the driest year in the 1990s so that we are comparing the driest and wettest years in the 1990s so far. Secondly, the ECMWF methods of analyzing data are never homogeneous due to the constant updating of the ECMWF model. By choosing relatively close years, this problem may be somewhat avoided. Thirdly, the long-term effect of land-cover transformation such as deforestation and desertification may be minimized due to the closeness of 1992 and 1994 (This does not mean that the short-term land surface conditions such as soil moisture are the same for the two years). Our hypothesis here is that the unique SST anomaly pattern may be an important factor in shaping the West African interannual rainfall variabilities. We are looking at the effect of SST interannual variability on the rainfall interannual variability. While the land surface properties are unavailable from observations, the SST measurement is very reliable. We would like to identify the major differences between the two years and use our model to examine the validity of our hypothesis. Our major concern will be the mechanisms associated with the impact of SST anomalies on West African rainfall.

5.2 Comparison Between 1994 and 1992 — Observations

In this section, we present a case study of 1992 and 1994. Our emphasis here is to identify the patterns of the difference for various variables between the two years.

5.2.1 Rainfall

The rainfall data set we use here is that of the Global Precipitation Climatology Project (GPCP), which is administered by the Global Energy Water Cycle Experiment (GEWEX). This data set provides monthly mean $2.5° \times 2.5°$ gridded precipitation data for the period July 1987 through December 1994 (December of 1987 is missing). The data set has been produced by blending rain gauge analysis, satellite-based (infrared and microwave) estimates of precipitation and NWP (National Weather Prediction) model precipitation information (Huffman *et al.*, 1995). The data set tries to use rain gauge analysis wherever possible to minimize any artificial component. The gauge data are analyses from the Global Precipitation Climatology Centre and reflect approximately 6700 gauges which have been carefully quality controlled.

Our aim here is to identify the rainfall difference pattern between 1994 and 1992. Figure 5.2 describes the annual mean rainfall from 30°S to 30°N and from 25°W to 25°E for 1994 (Fig. 5.2a), 1992 (Fig. 5.2b) and the difference between 1994 and 1992 (Fig. 5.2c). We see that the annual rainfall in 1994 is larger than that in 1992 over the whole West African region (defined as the region from 15°W to 15°E), ranging from 50mm to 300mm. By averaging rainfall longitudinally from 15°W to 15°E, Figure 5.3a and Figure 5.3b depict the seasonal migration of the rainbelt (ITCZ) for 1994 and 1992 respectively. Figure 5.3c shows the difference between 1994 and 1992. We observe that the larger annual rainfall over West Africa is mainly due to the positive rainfall anomaly starting from July up to November, maximizing in October. As a matter of fact, the October of 1994 is quite unusual in terms of the rainfall anomalies because

often October is near the end of the Sahel rainy season. The unusually abundant rainfall in October of 1994 is a manifestation of the fact that the ITCZ maintains a northward position for an anomalously long period of time in 1994 (see Fig. 5.3a). Note also that the rainfall over land is actually less in 1994 from May to July. At the same time, over the ocean we observe heavier rainfall. This spring positive rainfall anomaly pattern over the ocean follows a positive rainfall anomaly from January to February and a negative rainfall anomaly from February to April, all over the ocean and coastal regions.

5.2.2 SST

The SST data used here are taken from the monthly optimum interpolation (OI) SST analysis, which uses *in situ* and satellite SSTs plus SSTs simulated by sea-ice cover (Reynolds and Smith, 1994). The *in situ* data were obtained from radio messages carried on the Global Telecommunication System. The satellite observations were obtained from operational data produced by the National Environmental Satellite Data and Information Service (NESDIS). The data cover the whole globe and has a spatial resolution of $1° \times 1°$. The time coverage is from January of 1981 to December of 1995.

Figure 5.4 shows the longitudinally averaged (15°W to 10°E) SST difference between 1994 and 1992. We see that in general the SST in 1994 is warmer than that in 1992. Some features should be pointed out. First of all, the warm SST anomaly maximizes in May with the magnitude of 1.5°C. Secondly, the summer SST (from July to September) is also warmer in 1994 but the magnitude is only around one-third of the spring SST difference. This SST difference pattern agrees with Lamb (1978b) (see Fig. 5.1) in spring SST difference pattern between wet and dry composites but differs in summer SST difference pattern. As we will demonstrate later, the spring SST may be very important in terms of the impact on West African rainfall.
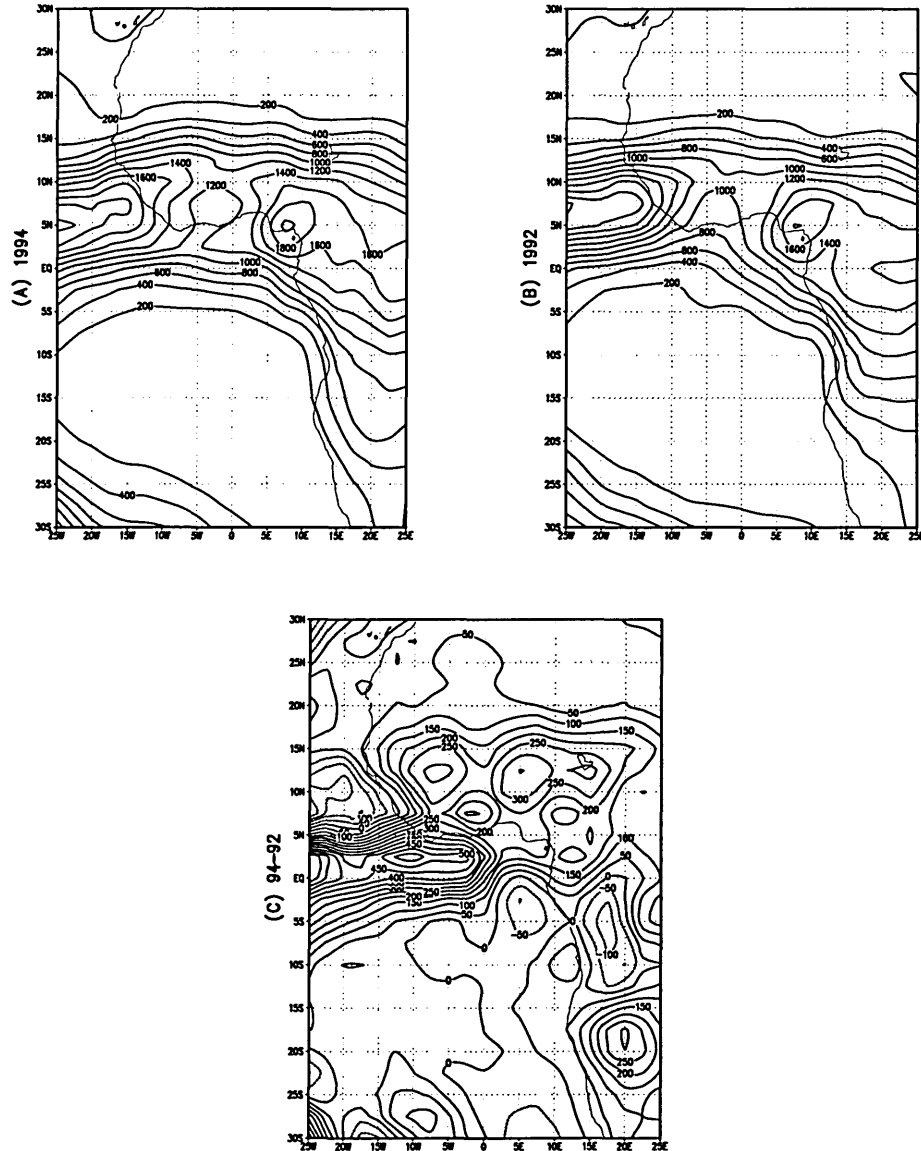
Figure 5.2: The annual mean rainfall (mm) in the region from 25°W to 25°E and from 30°S to 30°N for (a) 1994, (b) 1992 and (c) 1994-1992. The contour intervals are 100 mm for (a) and (b), and 50 mm for (c), from GPCP rainfall data set.
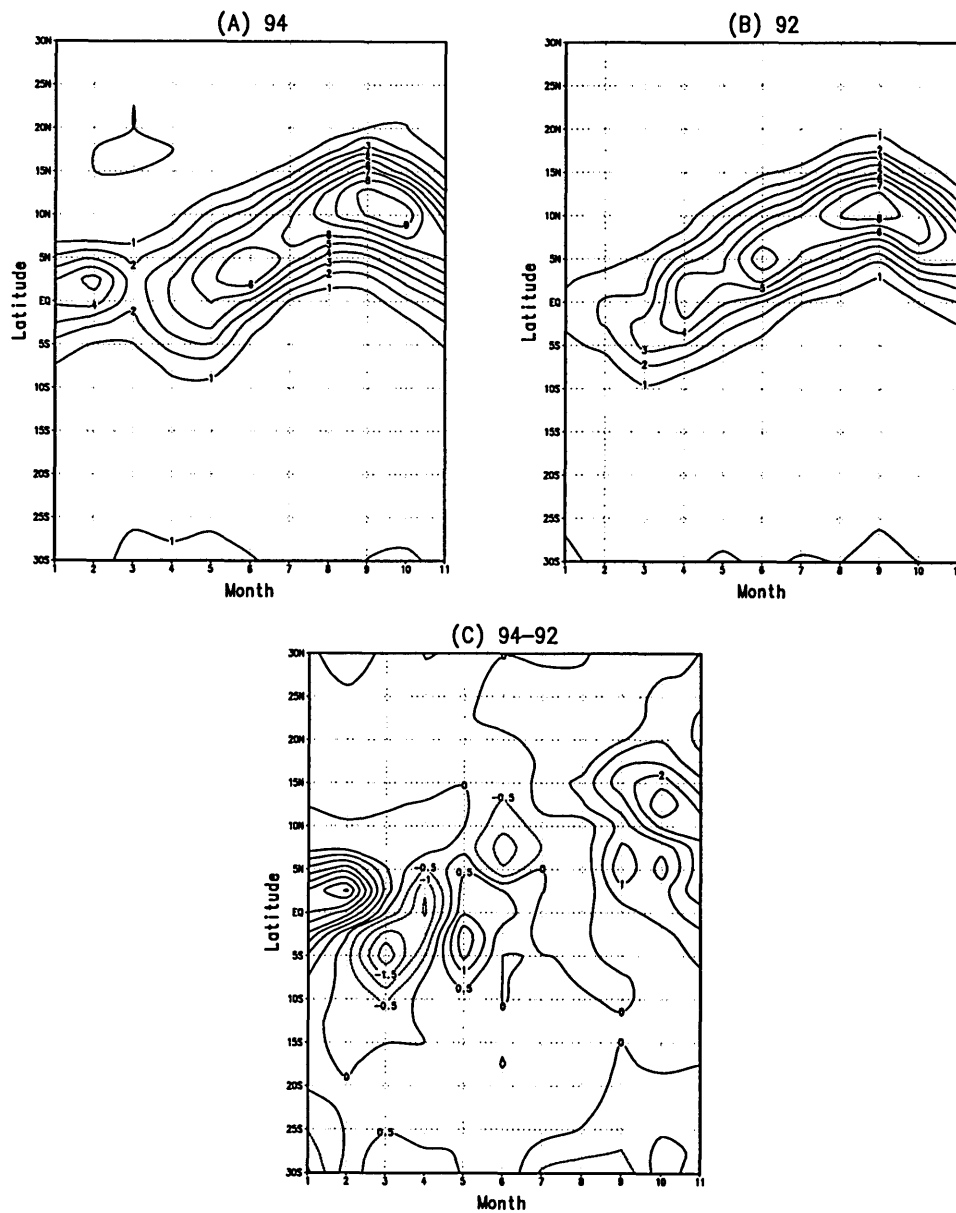
Figure 5.3: The longitudinally averaged (from 15°W to 15°E, West African region) rainfall latitude-month cross sections for (a) 1994, (b) 1992 and (c) 1994-1992. The contour intervals are 1 mm/day for (a) and (b) but 0.5 mm/day for (c). Note that the time coverage is only up to November because the rainfall data of December of 1994 are missing.

128
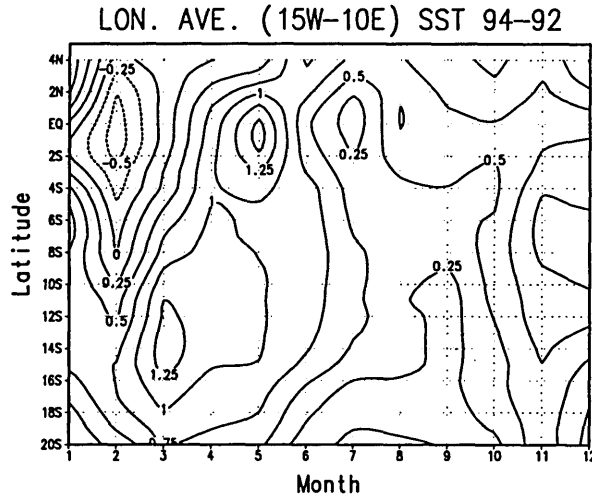
Figure 5.4: The longitudinally averaged (from 15°W to 10°E) SST difference between 1994 and 1992. The contour interval is 0.25°C.

5.2.3 Wind

We use the ECMWF analyzed observational data set. The spatial resolution is 2.5°×2.5°. The daily data expand from January 1985 to December 1995, with two observations available everyday: 0:00 UTC and 12:00 UTC. We use the monthly average, and also average the data between the day time and night time. During this eleven year period, the method used to analyze the observational data has been updated several times, so the data set is not homogeneous. However, for years of our interest, namely, 1992 and 1994, we can reasonably assume homogeneity during this relatively short period of time.

The meridional wind (Fig. 5.5) for the summer months (July-September) shows strong southerlies near the surface and northerlies near the tropopause for both 1994 and 1992. The picture agrees with the notion that West African monsoons can be viewed as thermally-direct meridional circulations (Chapter 1). The difference of the meridional wind between these two years (Fig. 5.5c) indeed shows a stronger meridional circulation in 1994. In addition, the low-level southerly extends further northward in 1994. As we have seen from the rainfall analysis, October of 1994 is very unique. Therefore, we single out the month of October here (Fig. 5.6). The

low-level southerly wind extends up to 15°N in October of 1994 but only up to 12°N in 1992. Again, Figure 5.6 indicates stronger October meridional circulation in 1994. Furthermore, the anomalous southerlies are very deep in October (up to 400 mb). These anomalies are not only deeper but also stronger than those of the summer months (Fig. 5.5c, Fig. 5.6c).

The zonal wind shows a stronger upper-level easterly jet (Fig. 5.7) and stronger surface wind (Fig. 5.8) in 1994. In addition, the low-level easterly jet in the Northern Hemisphere (15°N) is stronger for the dry year of 1992. This in general agrees with the analyses by Newell and Kidson (1984) for their wet (1958-1963) and dry (1969-1973) composites.

Furthermore, the horizontal divergence (Fig. 5.9) at the tropopause (250 mb) displays a good correspondence with the rainfall pattern (Fig. 5.3). The upper-level divergence pattern should reflect that of the vertical motion which in turn is closely related to rainfall. The difference of the upper-level divergence between 1994 and 1992 is given by Figure 5.9c. Comparing to Figure 5.3c, we observe resemblance between the two. The positive (difference) divergence over ocean from January to March coincides with the positive rainfall anomaly during the same period of time. What is more important to notice is the migration of positive divergence belt from over the ocean onto land as the season passes. The positive anomalous divergence seems to originate in May and then propagate onto the land, maximizing in October, agreeing with rainfall anomalies. The negative anomalous divergence persists from January to June over the land area from about 5°N to 17.5°N, consistent with the deficient rainfall over the land during the same period of time as shown in Figure 5.3c.

5.2.4 Boundary Layer Entropy

Because of the critical importance of boundary layer entropy in the dynamics of moist atmospheres, we here present some analysis regarding boundary layer entropy (expressed as equivalent potential temperature θ_e, averaged over the two lowest pressure

130
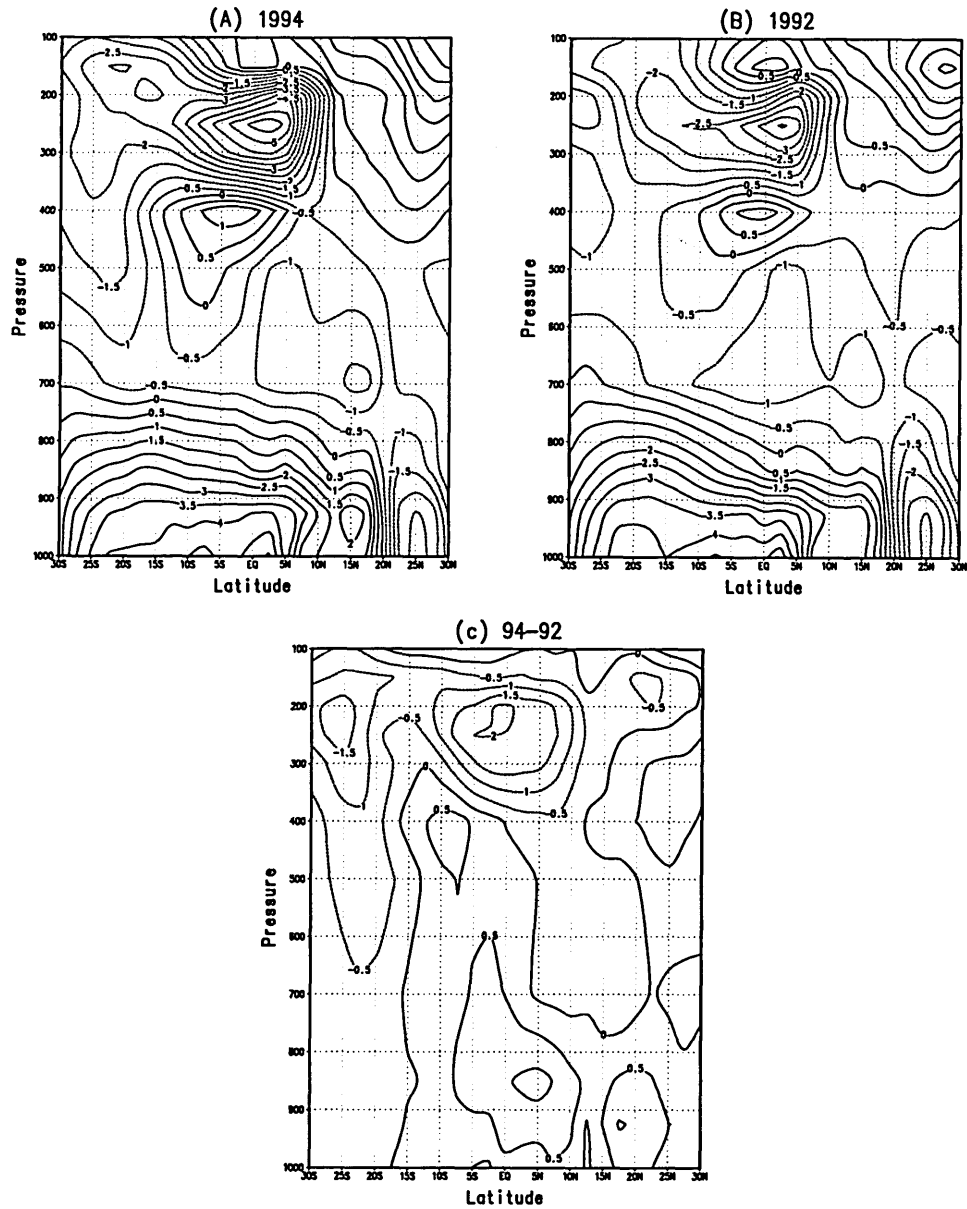
Figure 5.5: The longitudinally averaged (from 15°W to 15°E) summer (July-September) meridional wind pressure-latitude cross section for (a) 1994, (b) 1992 and (c) 1994-1992, contour interval 0.5 ms^{-1}.
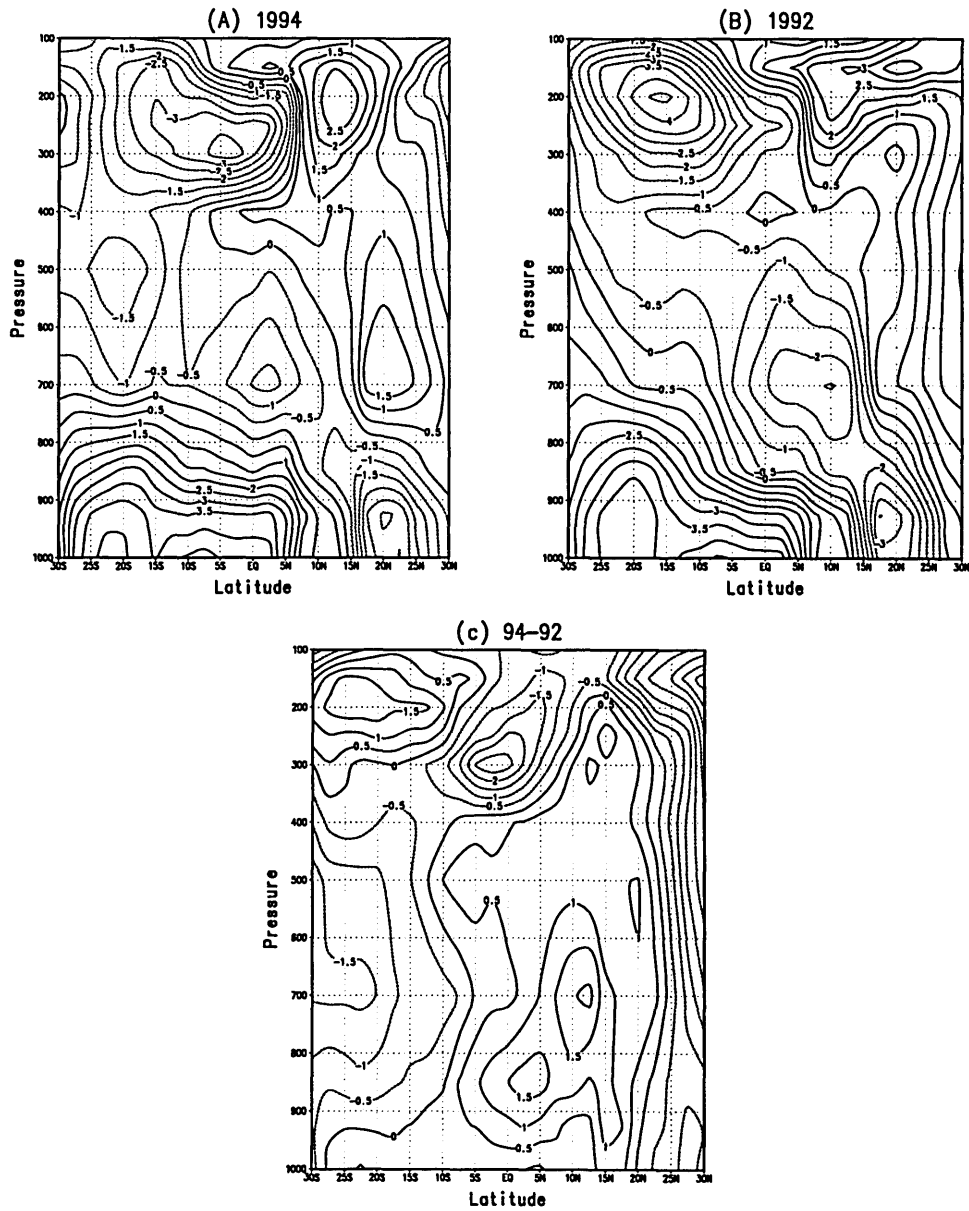
Figure 5.6: The longitudinally averaged (from 15°W to 15°E) October meridional wind pressure-latitude cross section for (a) 1994, (b) 1992 and (c) 1994-1992, contour interval 0.5 ms^{-1}.
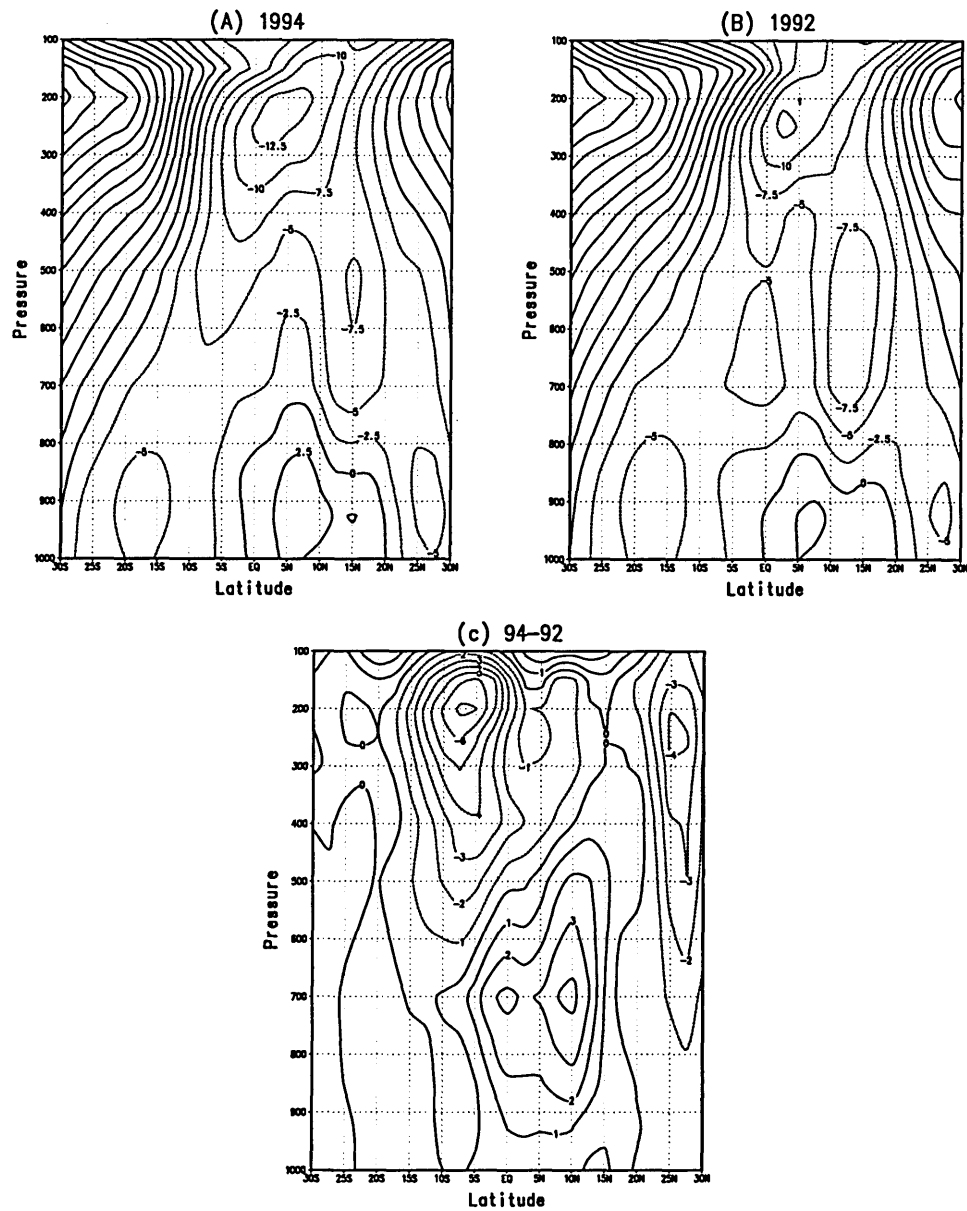
Figure 5.7: The longitudinally averaged (from 15°W to 15°E) summer (July-September) zonal wind pressure-latitude cross section for (a) 1994, (b) 1992 and (c) 1994-1992, contour interval 2.5 ms^{-1} for (a) and (b), 1.0 ms^{-1} for (c).
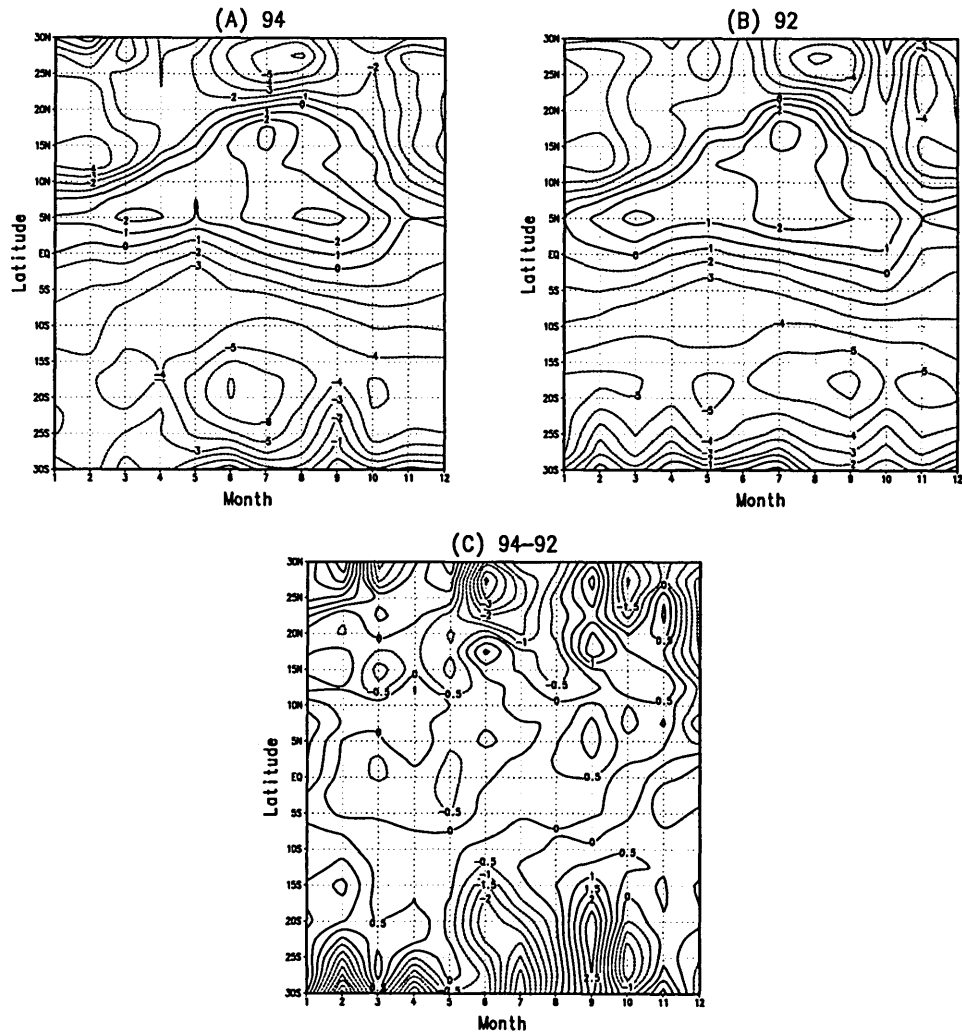
Figure 5.8: The longitudinally averaged (from 15°W to 15°E) 1000 mb zonal wind for (a) 1994, (b) 1992 and (c) 1994-1992, contour interval 1 ms⁻¹ for (a) and (b), 0.5 ms⁻¹ for (c).
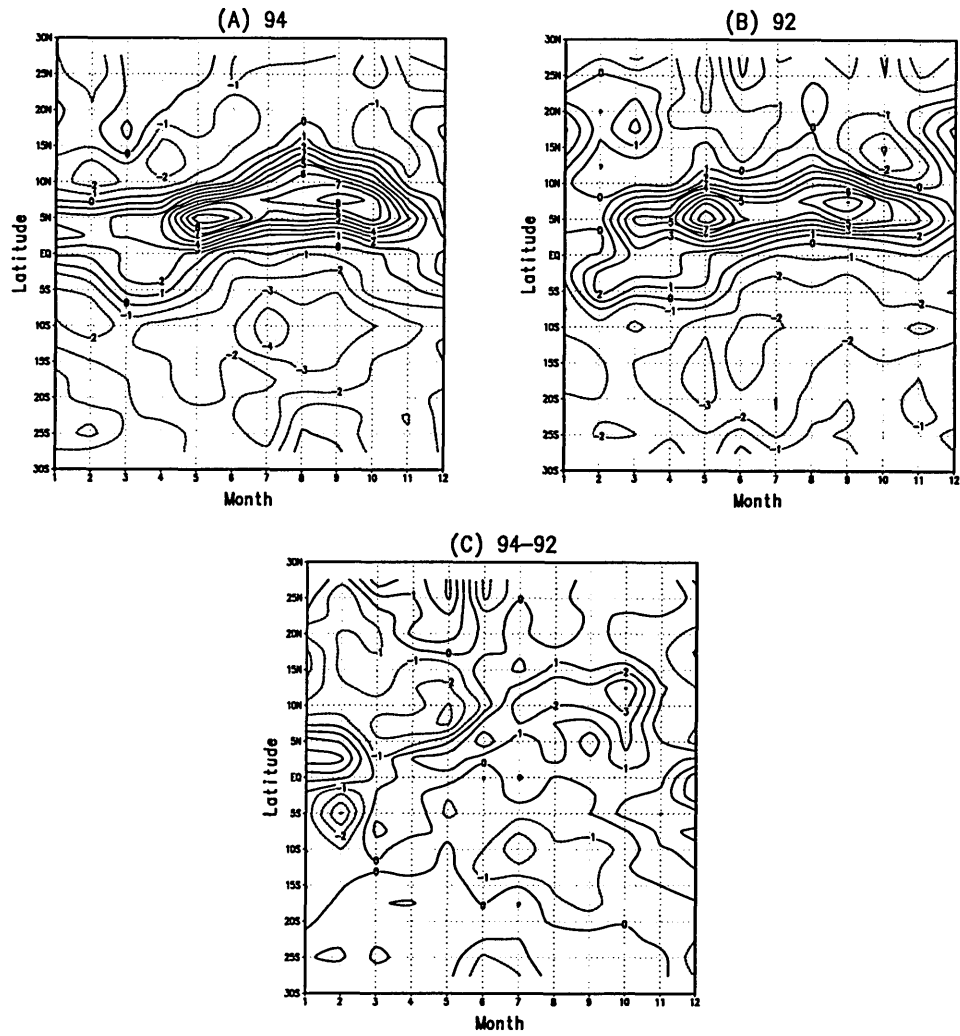
Figure 5.9: The longitudinally averaged (from 15°W to 15°E) horizontal divergence (250 mb, unit $10^{-6}s^{-1}$) for (a) 1994, (b) 1992 and (c) 1994-1992, contour interval $1\times10^{-6}s^{-1}$.
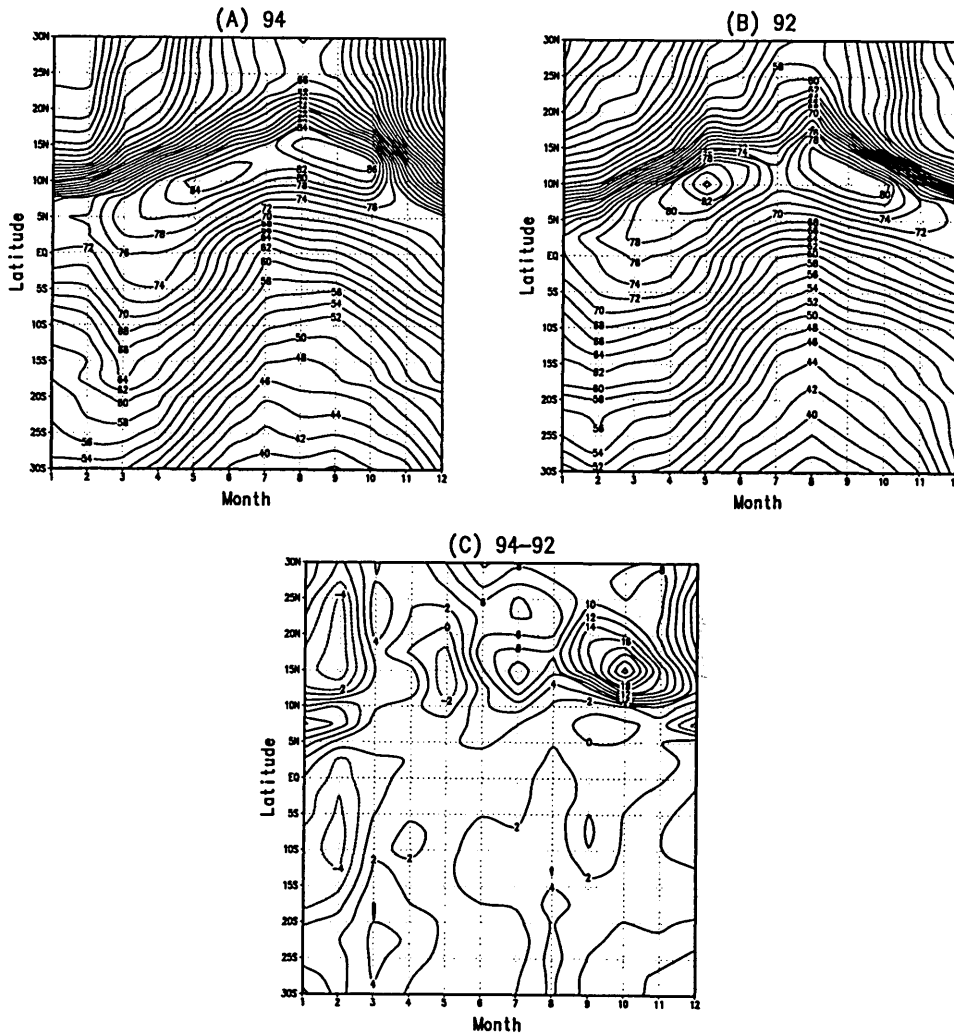
Figure 5.10: The boundary layer θ_e (°C) averaged from 15°W to 15°E and 1000 mb to 925 mb for (a) 1994, (b) 1992 and (c) 1994-1992, contour interval is 2°C.
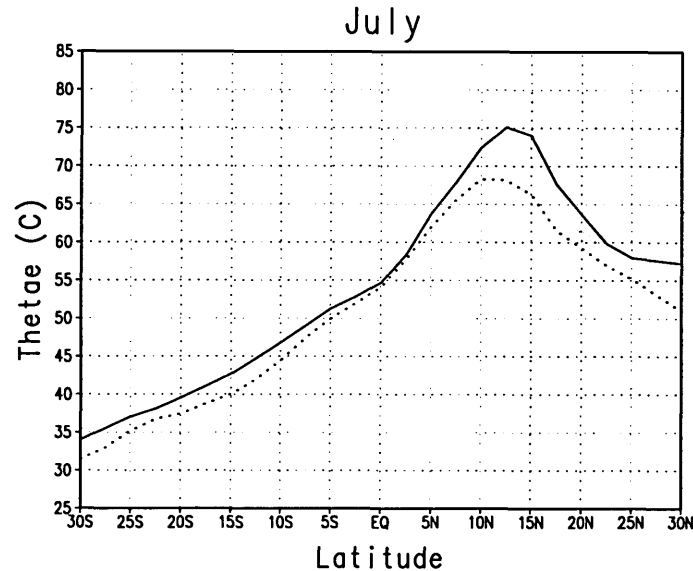
Figure 5.11: The latitudinal profile of boundary layer θ_e (°C) averaged from 15°W to 15°E and 1000 mb to 925 mb) for July of 1994 (solid) and 1992 (dotted).

levels 1000 mb and 925 mb). As we can see from Figure 5.10c, which is the difference between 1994 and 1992, θ_e over the ocean is generally higher in 1994 than in 1992, except January and February. This is consistent with the SST difference pattern (Fig. 5.4). This also confirms the notion that the boundary layer θ_e over the ocean basically follows the SST. What's striking in Figure 5.10c is that over the land area, the boundary layer θ_e displays huge difference between the two years. In particular, the θ_e starts to build up a positive anomaly in June that maximizes in October, consistent with both the rainfall anomaly pattern (Fig. 5.3c) and the upper-level divergence pattern (Fig. 5.9c). In fact, before the onset of the strong rainfall over Sahel, the boundary layer θ_e shows substantially stronger meridional gradient in 1994 than in 1992 (Fig. 5.11). Similar results were obtained by Eltahir and Gong (1996) in their analysis of the 1958 wet year and the 1960 dry year. Other notable difference patterns of boundary layer θ_e include a positive anomaly in the coastal region for January and

February and a negative anomaly for the month of May over the Sahel region ($10°N$ to $20°N$). All these coincide remarkably well with the rainfall difference pattern.

The positive boundary layer θ_e anomaly over the land area is mainly associated with the positive specific humidity anomaly, as can be seen in Figure 5.12. The surface air temperature is warmer during spring (up to June) but cooler for the rainy season, presumably due to larger evaporation caused by heavier rainfall in 1994 (Fig. 5.13).

5.2.5 Summary

The above analyses reveal remarkable consistencies among rainfall, wind, boundary layer entropy in spite of independent sources of data. It appears that the 1994 wet year in West Africa is closely associated with a stronger monsoon in 1994 compared to 1992. The rainfall anomaly pattern Figure 5.3c and the upper-level divergence anomaly pattern Figure 5.9c are very similar, showing the migration of anomaly from over the ocean during the spring onto the continent during the summer. The May positive rainfall anomaly over the ocean is consistent with the warm SST at that time (Fig. 5.4). This leads us to speculate that the spring SST anomaly may be important in shaping the observed interannual variability. In what follows, we will use a numerical model to address the possible impact of SST on the West African rainfall. While our model is designed as a process model, it does capture the essential features of the observed West African monsoon (e.g., rainfall and wind patterns), as we will see later on. Because of the simplicity of the model, the model is expected to deviate from the observations, in particular, in the magnitude of variability. On the other hand, the advantage of this model is that it allows us to explore the mechanisms in great detail.
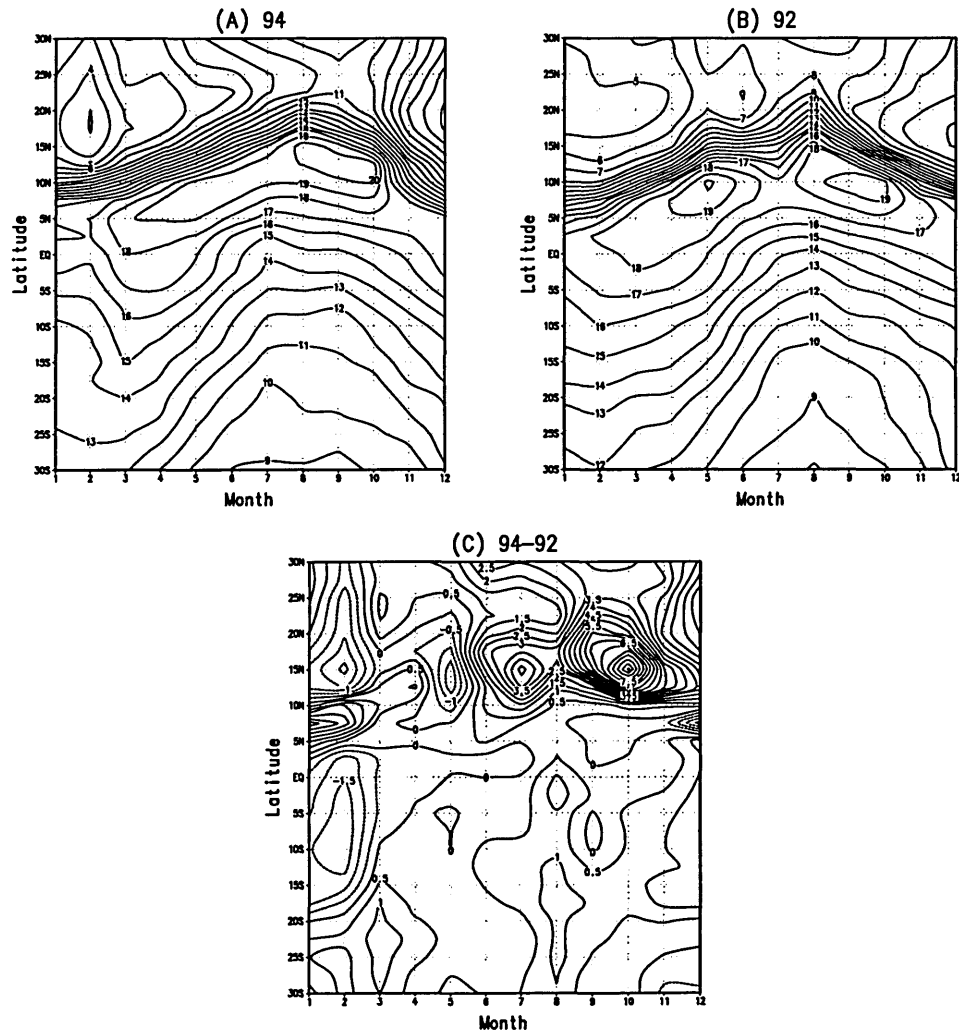
Figure 5.12: The boundary layer specific humidity (g/kg) averaged from 15°W to 15°E and 1000 mb to 925 mb for (a) 1994, (b) 1992 and (c) 1994-1992, contour interval is 1 g/kg for (a) and (b) but 0.5 g/kg for (c).
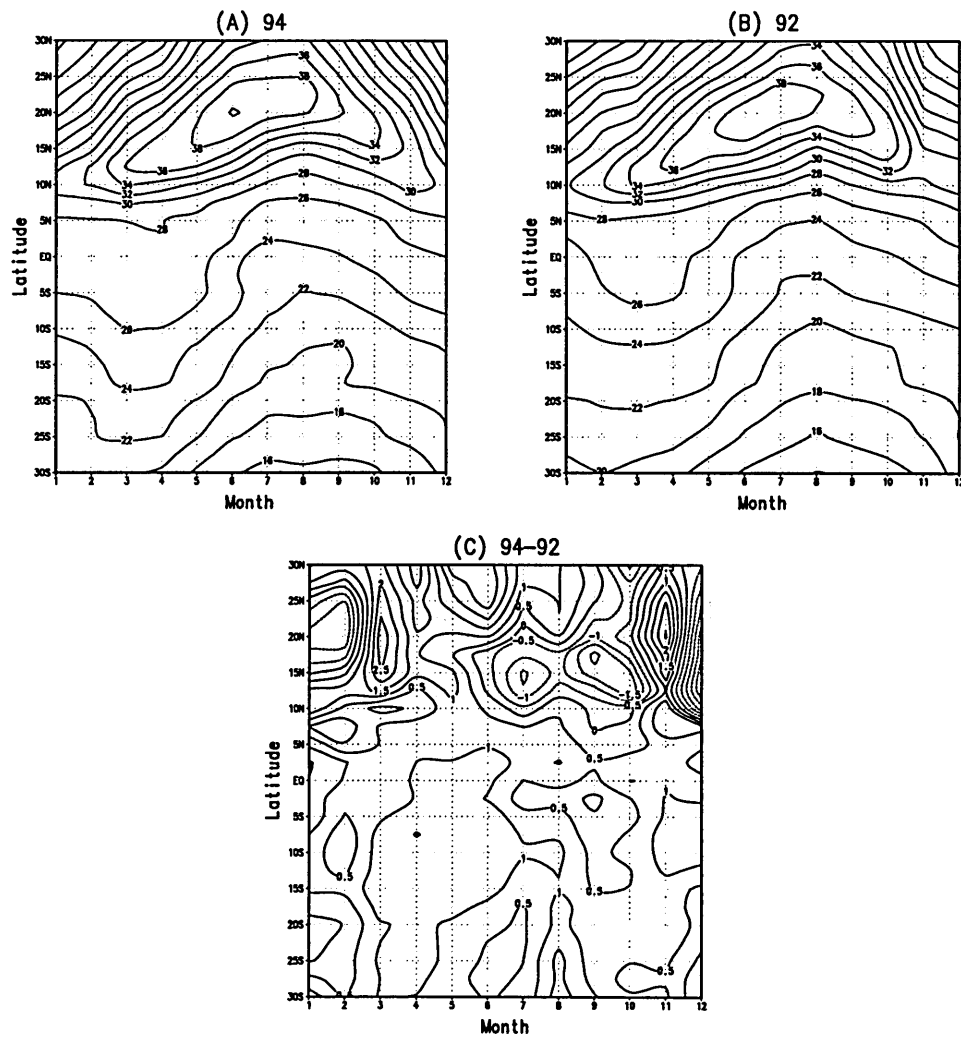
Figure 5.13: The boundary layer temperature (°C) averaged from 15°W to 15°E and 1000 mb to 925 mb for (a) 1994, (b) 1992 and (c) 1994-1992, contour interval is 2°C for (a) and (b) but 0.5°C for (c).

5.3   Control Experiment

5.3.1   Model Details

The observations indicate that the vegetation, temperature, specific humidity and rainfall in West Africa are approximately uniform in the zonal direction for a time scale substantially longer than several days (e.g., > monthly time scale, see Fig. 5.2). More importantly, our quantitative estimates in Section 4.2 show that the effect of zonal asymmetries is of second importance for the West African region we are interested. Therefore, our adoption of the zonally-symmetric dynamical framework as described in Chapter 2 is reasonably well justified in West Africa. The model is designed as a process model so that we are not trying to simulate the detailed variabilities in the natural system. Instead, a limited set of essential processes is included in order to investigate the essential physical processes that may be important for simulating realistic monsoons. Our purpose here is to use this relatively simpler model to identify some potentially important mechanisms, which in turn should be tested in more complicated models (e.g., GCMs) and against observations in the future.

The model used here is very similar to that used for the studies in Chapter 4, with some important modifications. These are described as follows.

The model domain is global horizontally and extends from the surface up to 25 km in log-pressure coordinates. The grid points are evenly spaced in sine latitude horizontally with 46 increments (about 2.5° resolution in terms of latitude in tropics), and also equally spaced vertically with 25 increments (1 km vertical resolution). The numerical schemes are identical to those in Chapter 4. In addition, we use the same diffusion scheme and diffusion coefficient as in Chapter 4.

The model convective scheme remains unchanged as of Chapter 4. However, while using the same Chou radiative scheme, we allow a seasonal cycle of the solar insolation in this chapter. Again, no diurnal cycle is included. Moreover, cloud processes, which

are poorly understood and may be important in nature, are excluded throughout this chapter.

The model domain represents a longitudinally-averaged (from 15°W to 15°E) latitude-height cross section. Therefore, our model results should be compared with the longitudinally-averaged values from 15°W to 15°E. The model surface consists of a land surface north of 5°N (which is assumed to be the location of southern Atlantic coast) and a ocean surface south of 5°N. SST is taken from the OI data set we mentioned in Section 5.2.2. The control experiment uses the SST climatology from 1981-1995. Since the data set only provides monthly averaged value, we apply linear interpolation within the time domain. We assume that the monthly SST represents the SST at the mid-month day (e.g., January SST is set equal to the SST on January 15). The SST at any time between two consecutive mid-month days (e.g., April 15 to May 15) is based on linear interpolation. Since our model is zonally-symmetric, we have to ignore zonal variation of SST. Nevertheless, the typical SST pattern in the southern tropical Atlantic Ocean shows that the meridional gradient is dominant over the zonal gradient (see Fig. 5.14). We use the longitudinally averaged value from 3°W to 3°E as model input. By doing so, the climatological (1981-1995) model control SST is shown in Figure 5.15. The SST pattern is not sensitive to the averaging longitude range, the difference between 3°W to 3°E and 5°W to 5°E is quite small, as can be seen from Figure 5.16.

The major difference between our present model and the model we used in Chapter 4 is the treatment of the land surface processes. The land surface temperature was assumed to be determined by the surface energy balance in Chapter 4. In other words, the land had zero heat capacity. This assumption is in general valid because the land heat capacity is much smaller than that of the ocean. In fact, this assumption does not influence the results in Chapter 4 since we only considered steady state solutions there. Here we are concerned with the seasonal migration of West African rainfall; we therefore assume a finite heat capacity of land. This modification is not essential but
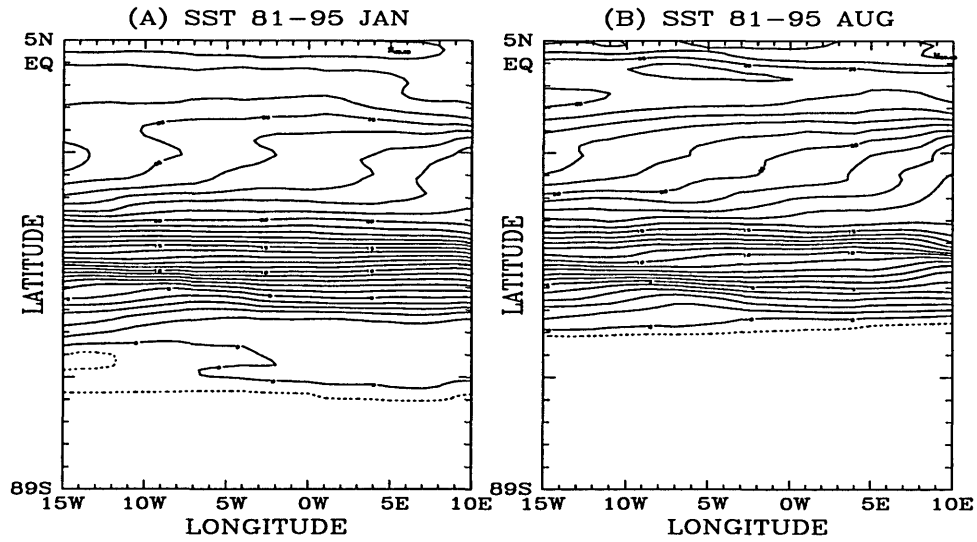
Figure 5.14: The climatological SST for 1981-1995, (a) January and (b) August, contour interval 1°C.
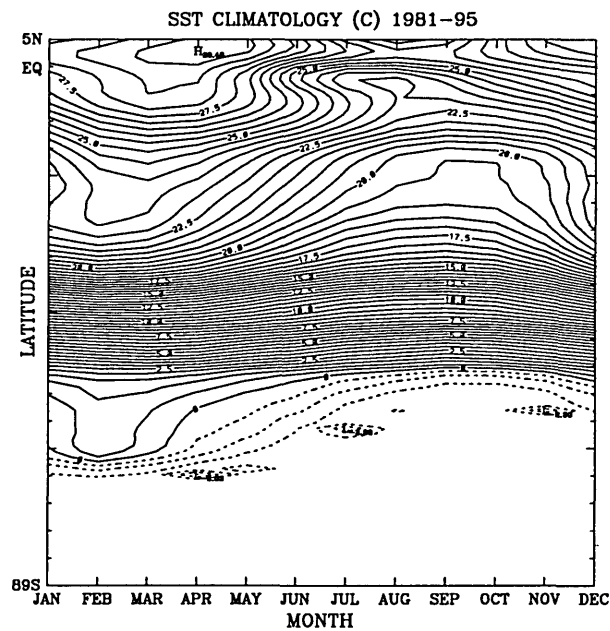
Figure 5.15: The longitudinally averaged (from 5°W to 5°E) SST (contour interval 0.5°C) climatology for 1981-1995.
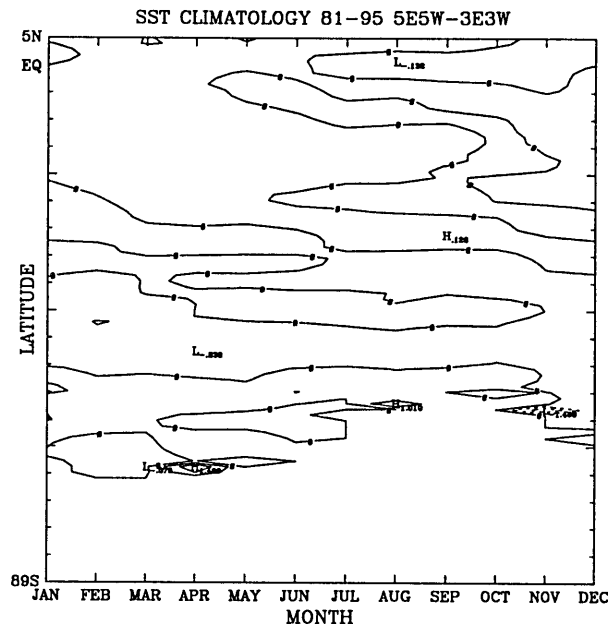
Figure 5.16: The difference of SST for two different longitude averaging ranges: 5°W-5°E minus 3°W-3°E, for 1981-1995 climatology.

the inclusion of the finite land heat capacity does have an impact on multi-day time scales as we will see later. We follow Srinivasan *et al.* (1993) and use the effective volumetric heat capacity of the soil per unit area $C_E = 4.5 \times 10^6$ Jm^{-2}K^{-1}. The land surface temperature equation is:

$$C_E \frac{\partial T_g}{\partial t} = R_{net} - H - L_v E,$$

where T_g is ground temperature; t time; R_{net} surface net radiative flux; H surface sensible heat flux; $L_v E$ surface latent heat flux, with L_v latent heat of vaporization and E surface evaporation.

Following Chapter 4, we also use the Budyko (1974) climate index of dryness as the indicator of the vegetation type. The vegetation type basically determines the depth of the root zone and therefore the field capacity (the maximum soil moisture

144

the soil can hold). We assume a latitudinal profile of the dryness index of West Africa (see Figure 5.17) which is similar but not identical to Chapter 4. This profile is meant to mimic the distribution of the actual natural vegetation in West Africa qualitatively. In general, the dryness index has a small value (less than 1) within the tropical forest region and increases northward, achieving maximum (greater than 3) in the desert region. This dryness index pattern roughly depicts the transition of the vegetation type in West Africa, from tropical forest near the southern Atlantic coast to the semi-arid plants (grasslands, shrubs) in Sahel and Sahara desert. The analytical form of the assumed dryness index is:

$$D = \begin{cases} 0.5 & \phi_0 \leq \phi \leq \phi_1, \\ 3.7 + (3.7 - 0.5)\frac{\phi - \phi_2}{\phi_2 - \phi_1} & \phi_1 < \phi \leq \phi_2, \\ 3.7 & \phi > \phi_2, \end{cases} \tag{5.1}$$

where ϕ is latitude; $\phi_0 = 5°N$ (coast line); $\phi_1 = 10°N$; $\phi_2 = 20°N$.
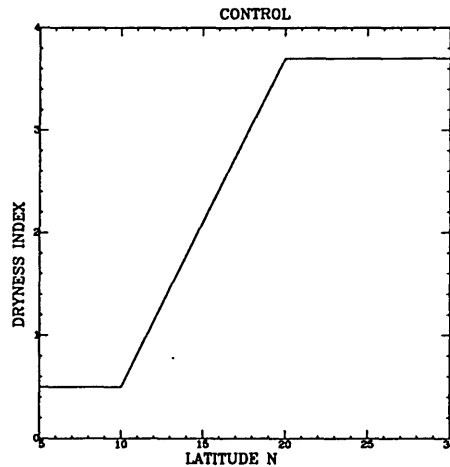
Figure 5.17: The distribution of the dryness index for the control experiment.

We follow Gutman et al. (1984) and relate the field capacity (W_c) to the dryness

index (D):

$$W_c = W_0 \frac{\tanh D}{D} \qquad D \geq 0,$$

where $W_0 = 80$ cm (Dickinson *et al.*, 1986). This simply means that the maximum soil moisture depends on the vegetation type (depth of the root zone), as indicated by the dryness index here. The latitudinal profile of the field capacity is shown in Figure 5.18.
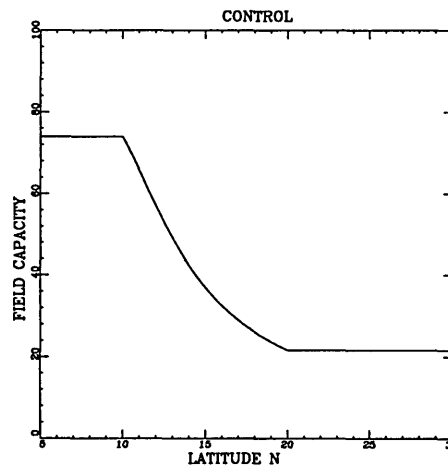
Figure 5.18: The distribution of the field capacity in centimeter for the control experiment.

A simple soil hydrology scheme is added in this model, we use the simplest bucket model (Manabe, 1969). What's different here is that our field capacity has latitudinal variation whereas in Manabe (1969) the field capacity was held constant. The soil moisture W prognostic equation is:

146
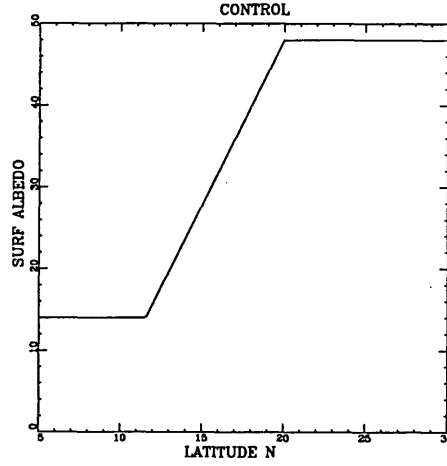
Figure 5.19: The distribution of the surface albedo in percentage for the control experiment.

$$\frac{\partial W}{\partial t} = \begin{cases} 0 & W \geq W_c \text{ and } P \geq E, \\ P - E & \text{otherwise,} \end{cases} \tag{5.2}$$

where P is precipitation, E evaporation. Any excessive soil moisture above field capacity is considered as runoff. The evaporation is evaluated according to the relative saturation of soil moisture $\frac{W}{W_c}$ and potential evaporation (E_p) which is parameterized by a bulk formula (drag coefficients are 1.0×10^{-3} for the ocean and 2.0×10^{-3} for the land):

$$E = E_p \left(\frac{W}{W_c}\right)^\beta .$$

β is generally taken as 1.0. However, in our model, we take into account the fact that it is easier to evaporate in less vegetated region than in densely vegetated region. Therefore, we assume $\beta = 1.2$ for forest region (defined as the region in which $D \leq 1$), $\beta = 1.0$ for savanna region (defined as $2 \geq D > 1$) and $\beta = 0.8$ for semi-arid and

desert region (defined as $D > 2$).

The recent ERBE (Earth Radiation Budget Experiment) observed that the surface albedo (α) of West Africa has a quite zonally-uniform distribution (Darnell et al., 1995), supporting our use of the zonally-symmetric model. In addition, the surface albedo was found to be highly reflective (as high as 48%). Here we assume an analytical form of albedo versus dryness index to mimic the observed albedo pattern, shown in Figure 5.19:

$$\alpha = \begin{cases} \min(0.48, 0.014 + 0.126D) & D \geq 1, \\ 0.14 & 0 < D < 1. \end{cases} \tag{5.3}$$

Note that within the tropical forest region (defined as $0 < D < 1$), there is no dependence of the surface albedo on the dryness index (Gutman et al., 1984). Moreover, we also take account the effect of soil moisture on the surface albedo by multiplying the surface albedo defined above by a factor $(1 - 0.5\frac{W}{W_c})$ for all regions except tropical forest region where the albedo is held as 0.14. This means that the saturation of the soil can decrease the albedo defined in equation (5.3) by a half for fully saturated soil. The oceanic surface albedo is taken as 0.06.

5.3.2 Control Run

The control run is forced by the observed 1981-1995 climatological SST as shown in Figure 5.15. The solar forcing has a seasonal cycle (no diurnal cycle). The model is first integrated for 300 days by fixing the solar insolation at the spring equinox. This produces the initial state for subsequent runs with seasonally varying solar insolation. This model is integrated long enough (about two to three years) to get a statistically-equilibrated annual cycle, which is used as our control atmosphere. Multi-year model integration shows that the equilibrated annual cycle has very little variance (Fig. 5.20).
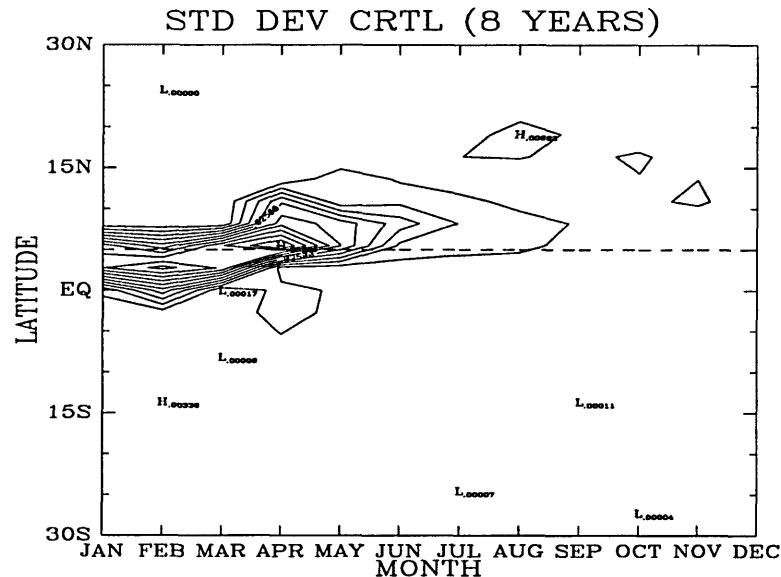
Figure 5.20: The rainfall standard deviation for the 8 year model control run, the contour interval is 0.005 mm/day.

The total rainfall of the control experiment shows the migration of rainband from over the ocean in winter onto the land in summer (Fig. 5.21). Compared to the observation (see Fig. 5.22), the model does simulate the gross features of the seasonal cycle of the West African rainfall. For example, the ITCZ (location of the maximum rainfall) achieves its northern-most position in September, as observed (Fig. 5.22). In addition, the latitude of this position is roughly the same as that of the observation. Also, as can be seen from the latitudinal profile of the total rainfall in September (Fig. 5.23), there is a sharp gradient of rainfall from the position of ITCZ (12°N) northward to the desert (20°N), presumably due to the constraint of the Sahara desert on the ITCZ northward propagation. The comparison of the rainfall latitudinal profiles between the model and the observation indicates a generally good agreement in terms of the location of the ITCZ and the north-south gradient of the rainfall. In addition, the seasonal cycle of the rainfall over the region from 10°N to 20°N displays similarity to the observations, although the model overestimates the rainfall magnitude, especially for June and July (about 3 mm/day), as can be seen

in Figure 5.24. This may have to do with the neglecting of zonal asymmetries. As we have seen from Section 4.2, the zonal asymmetries result in a net moisture divergence out of the West African region. In other words, the zonally-symmetric models tend to exaggerate moisture convergence into the region (others being the same).
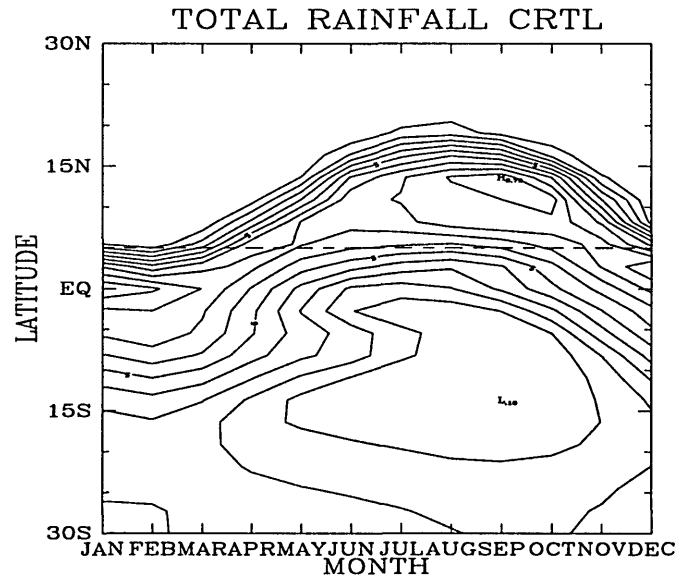
Figure 5.21: The total rainfall of the control experiment, the contour interval is 1 mm/day.

On the other hand, the winter rainfall (December, January, February) over the ocean is much heavier than the observations. This has to do with the assumption of zonal symmetry. For one thing, the model lacks the meridional heat transport due to zonally-asymmetric eddies (dominant in winter), and the surface temperature gradient between the warm ocean and the cold land is unrealistically large, producing strong updraft over the warm ocean. Secondly, the observed maximum winter rainfall actually occurs in the southern African land region instead of over the Atlantic Ocean (Fig. 5.25). This would produce subsidence elsewhere and hence is unfavorable for the development of rainfall over the Atlantic Ocean. Obviously, this mechanism is missing in our two-dimensional model.

The soil moisture shows a smooth seasonal cycle (Fig. 5.26). In combination with
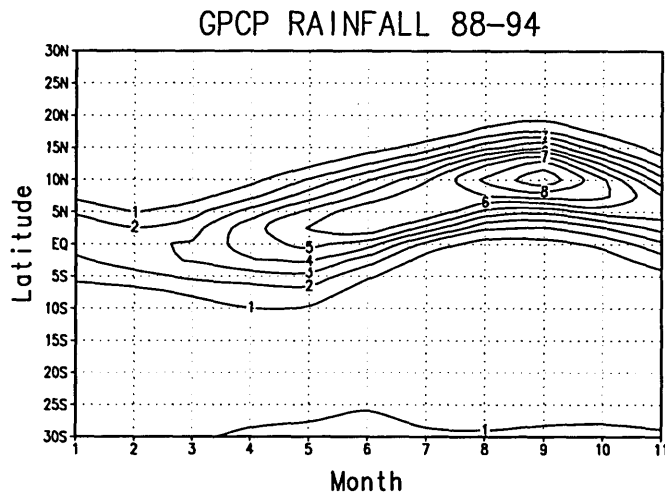
Figure 5.22: The GPCP rainfall climatology from 1988-1994, averaged from 15°W to 15°E, the contour interval is 1 mm/day.
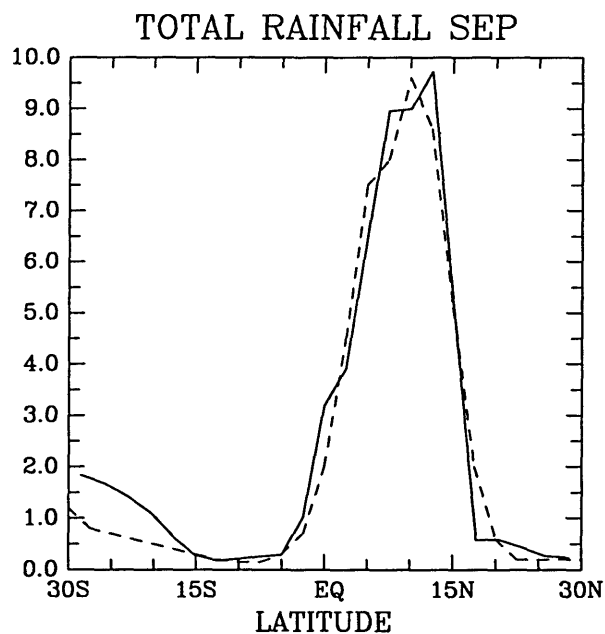
Figure 5.23: The latitudinal profile of the total rainfall in September for control experiment (solid line) versus the observed 1987-1994 GPCP September climatology (dashed line), averaged from 15°W to 15°E.
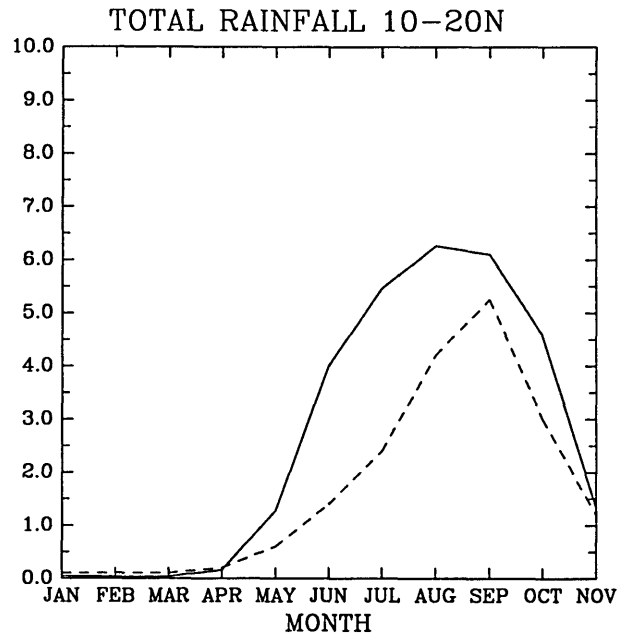
Figure 5.24: The time series of the total rainfall over the region from 10°N to 20°N for the control run (solid line) and the observed 1988-1994 GPCP rainfall climatology climatology (dashed line).
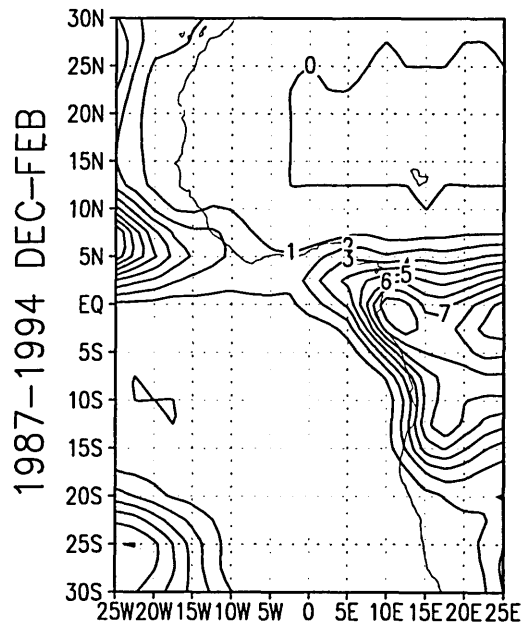
Figure 5.25: The GPCP rainfall in West African region from December to February, climatology from 1987-1994, contour interval 1 mm/day.

the seasonal cycle of large-scale moisture convergence (Fig. 5.27), we see that the soil moisture follows the pattern of the large-scale moisture convergence, as indicated by equation (5.2). Because the large-scale moisture convergence is negative over the land in winter, the soil moisture decreases and achieves minimum in spring. Likewise, the rainfall maximum occurs in September and the maximum soil moisture occurs in late October.
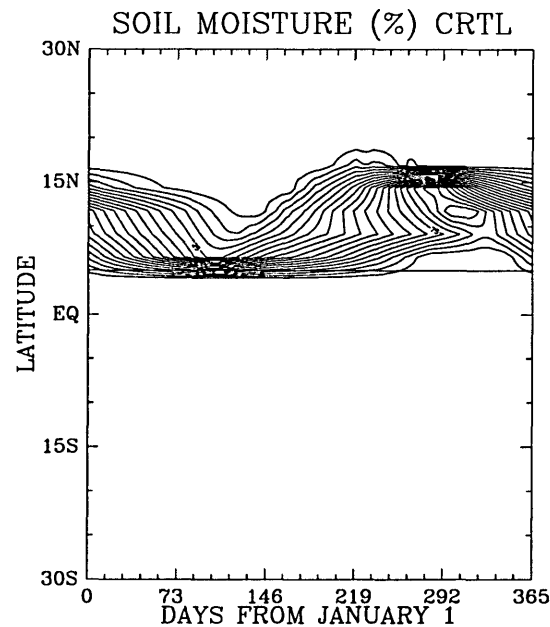
SOIL MOISTURE (%) CRTL

Figure 5.26: The relative soil moisture (ratio between soil moisture and field capacity) latitude-time cross section for the control case, contour interval 5.

We emphasized that the boundary layer entropy is the key variable in the dynamics of moist atmospheres (Emanuel, 1995; Eltahir and Gong, 1996). The model surface air moist entropy expressed in terms of θ_e is shown in Figure 5.28. The distribution of boundary layer θ_e is by no means simulating the details of the observations (e.g., Fig. 5.10). For example, the observed maxima of θ_e in September and October at the latitude of around 12°N (see Fig. 5.10) are not well simulated. But if we look at the line of maximum θ_e, we do see the tendency of achieving a maximum in September and October for the model. The difference is largely due to an unrealistic model winter simulation, which is what we should expect due to lack of northward heat
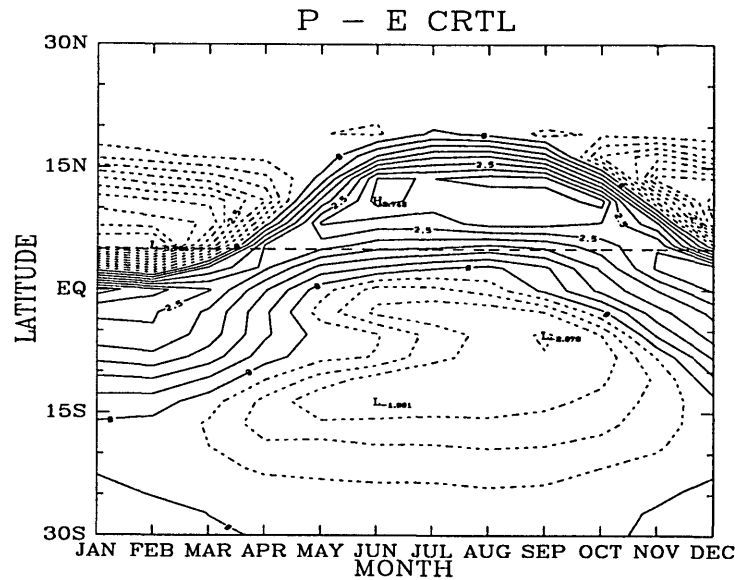
Figure 5.27: The large-scale convergence expressed as the difference between total rainfall and local evaporation for the control experiment, contour interval 0.5 mm/day.

transport by eddies. The surface air temperature and specific humidity are shown in Figure 5.29 and Figure 5.30 respectively. They also show similar patterns as those of observations (Fig. 5.13 and Fig. 5.12), although quantitative differences exist. The major caveat of the control experiment is still the unrealistic winter scenario, as we mentioned earlier.

Although the overall pattern of the surface air θ_e bears resemblance to the observations, our model control experiment does deviate substantially from the observations quantitatively. This implies that our model sensitivity to surface anomalies might be different from that of the ECMWF data. In other words, for the same surface anomaly such as SST anomaly, the model may have a different response from the observations, especially in terms of the magnitude. Remember that the model is developed as a process model. The understanding of mechanisms is our goal here. Since the model is able to capture the essential rainfall spatial and temporal patterns over West Africa, it allows us to investigate the physical mechanisms that might be relevant to real West African rainfall variability. In order to get significant model
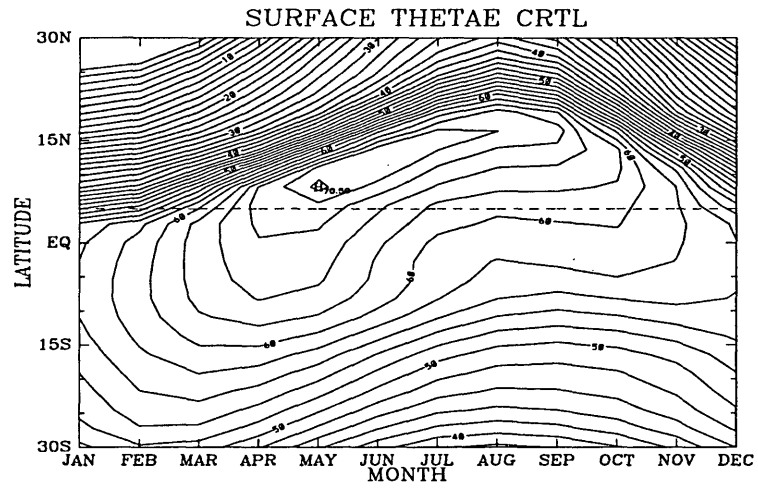
Figure 5.28: The boundary layer θ_e (°C) for the control experiment, contour interval 2°C.
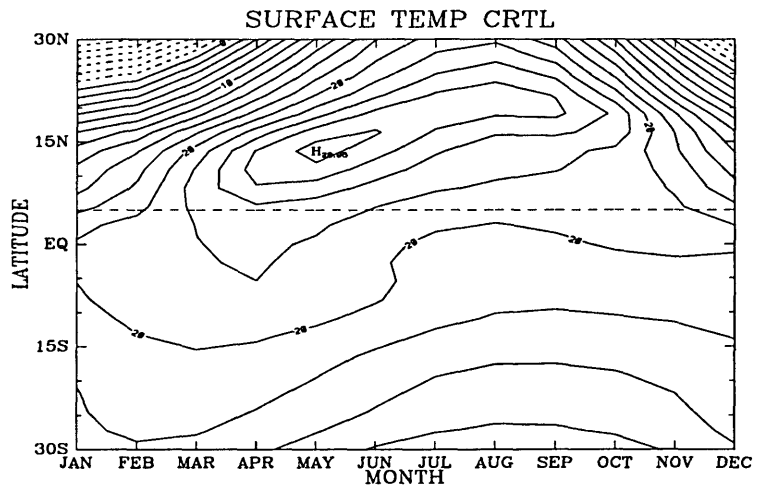
Figure 5.29: The surface air temperature for the control experiment, control interval 2°C.
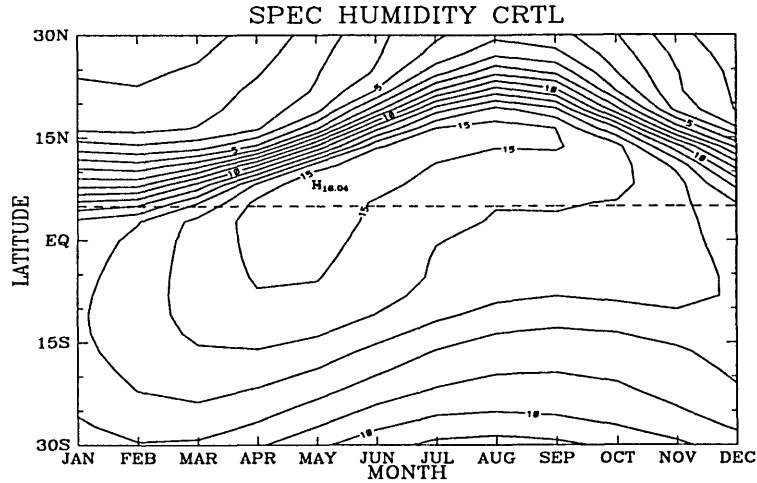
Figure 5.30: The surface specific humidity (g/kg) for the control experiment, control interval 1 g/kg.

anomaly patterns, we sometimes specify a larger magnitude of SST anomalies. We do not expect the model to be able to simulate the variability (e.g., magnitude) of the real world, we do expect that the model gives us correct anomaly patterns.

5.4 Hypothetical Anomaly Experiments

Now we apply hypothetical SST anomalies (superimposed on the monthly SST of the 1981-1995 climatology) to the control experiment. We specify the anomaly as a Gaussian distribution:

$$T' = T_{max}e^{-(\frac{\phi-\phi_c}{\delta\phi})^2} \tag{5.4}$$

where T' is the monthly SST anomaly; T_{max} the magnitude; ϕ latitude; ϕ_c latitude of the maximum T'; $\delta\phi$ half width in latitude. We take $\phi_c = 10°S$ and $\delta\phi = 30°$. The assumed SST anomaly pattern loosely mimics that of Lough (1986). Note that the SST anomaly is interpreted as the value at the mid-month day (e.g., the January SST

anomaly is set at January 15), just as what we did for the control experiment. The SST anomaly between any two mid-month days is calculated by linear interpolation.

We divide a year into four quarters: January to March, April to June, July to September, October to December. We first discuss a set of four SST anomaly experiments. These four experiments include imposing the SST anomaly given by equation (5.4) to January-March, April-June, July-September, October-December respectively. This set of experiments is designed to explore the role of the timing of SST anomalies. For each experiment, the model is integrated long enough (about two years) to get a statistically equilibrated annual cycle. This is compared with the control experiment. The rainfall anomaly caused by January-March SST anomaly is shown in Figure 5.31. For October-December SST anomaly, the rainfall anomaly is shown in Figure 5.32. It is very clear that SST anomalies imposed in winter months (October-March) have the least influence on the summer rainfall. On the other hand, the spring (April-June) SST anomaly (Fig. 5.33) induces a substantial summer rainfall anomaly, see Figure 5.34. In particular, we note that the rainfall anomaly pattern caused by the spring SST anomaly is very similar to the observed rainfall difference pattern between 1994 and 1992. This experiment suggests that spring SST anomaly is able to produce the observed rainfall anomaly pattern. That is, a positive rainfall anomaly emerges over the ocean in spring in response to the warm SST anomaly; in the mean time, a negative rainfall anomaly is observed over the land; then the positive rainfall anomaly appears to propagate onto the land as summer comes. This experiment will be referred to *standard spring SST anomaly experiment* hereafter. Finally, the summer (July-September) SST anomaly causes negative summer rainfall anomaly over the land but we do see a similar positive rainfall anomaly propagation from the ocean onto the land (Fig. 5.35). As a result, the rainfall in late summer and early fall has a positive anomaly over the land, although the anomaly is confined south of 10°N.

The above experiments suggest that Atlantic spring SST anomalies are positively
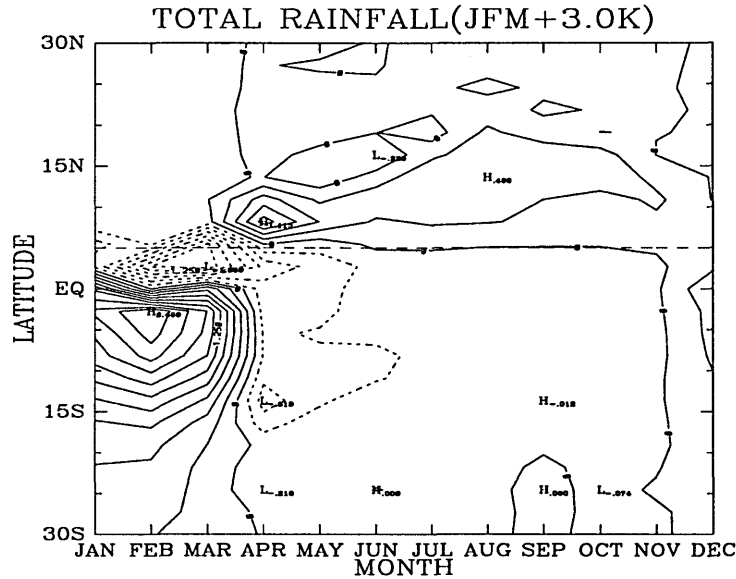
Figure 5.31: The total rainfall anomaly caused by the specified SST anomaly (magnitude $T_{max} = 3.0$ K) for January-March, the contour interval is 0.25 mm/day.
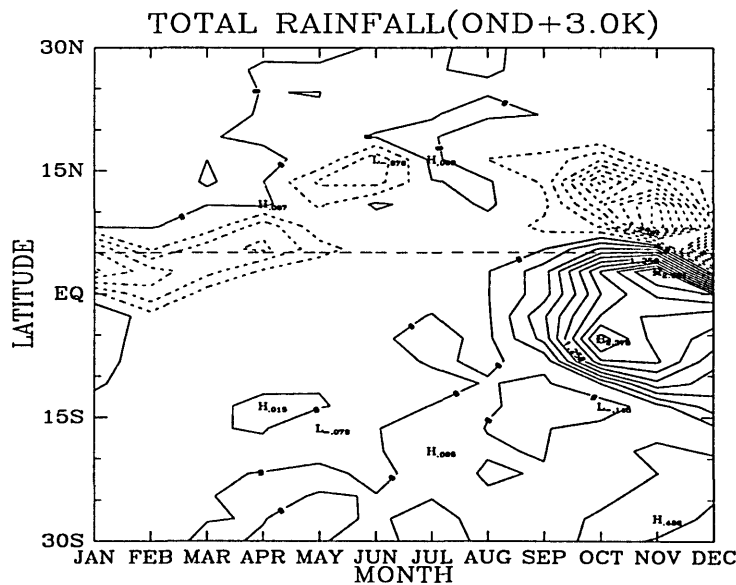
Figure 5.32: The total rainfall anomaly caused by the specified SST anomaly (magnitude $T_{max} = 3.0$ K) for October-December, the contour interval is 0.25 mm/day.

158
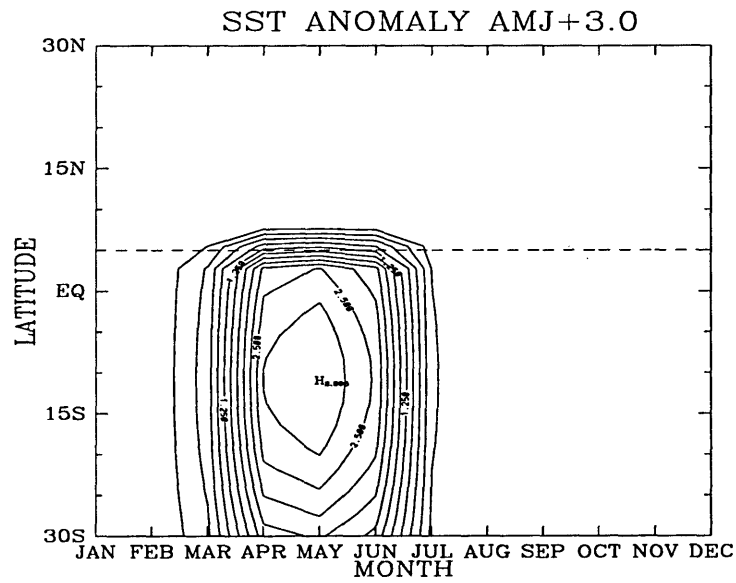
Figure 5.33: The imposed spring SST anomaly, the contour interval is 0.5 K.
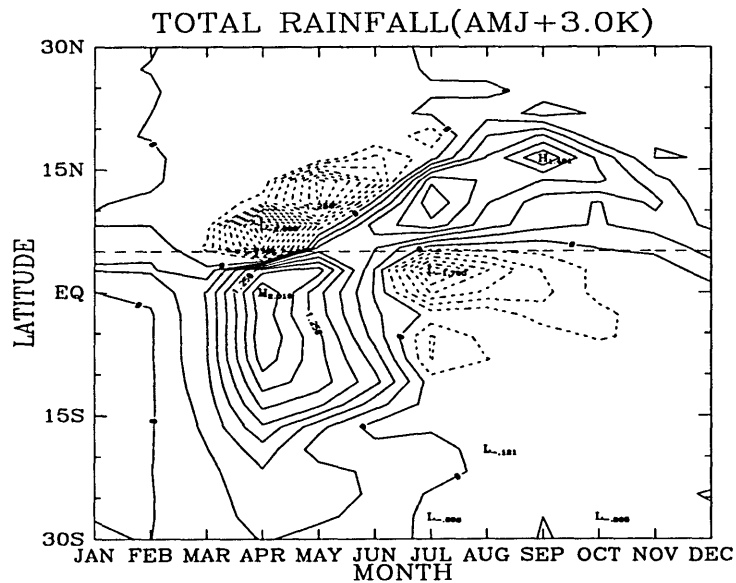
Figure 5.34: The total rainfall anomaly caused by the specified SST anomaly (magnitude T_{max} = 3.0 K) for April-June, the contour interval is 0.25 mm/day.
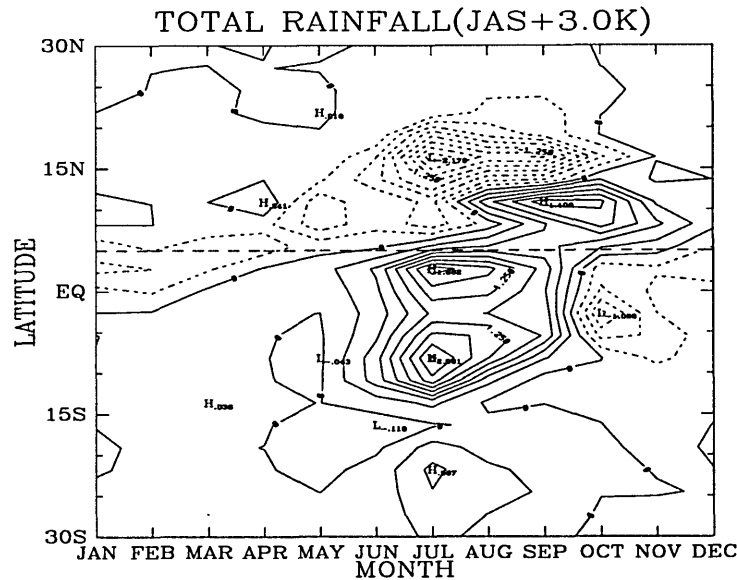
Figure 5.35: The total rainfall anomaly caused by the specified SST anomaly (magnitude $T_{max} = 3.0$ K) for July-September, the contour interval is 0.25 mm/day.

correlated with the West African summer rainfall whereas the summer SST anomaly is negatively correlated with the summer rainfall. Therefore, a positive spring SST anomaly plus a negative summer SST anomaly are favorable for abundant summer rainfall in West Africa and vice versa. This finding is qualitatively consistent with the composite study of Lamb (1978b), see Figure 5.1. The winter SST anomalies in general have relatively minor impact on the summer rainfall. In what follows, we will look into the mechanisms behind these results, within the context of our model. In particular, our main focus will be on the mechanisms of rainfall anomaly pattern caused by the spring SST anomaly.

5.5 Mechanisms

5.5.1 Other Details of the Standard Spring SST Anomaly Experiment

We have seen from Figure 5.34 that the spring SST anomaly first produces positive rainfall anomaly over the ocean and negative rainfall anomaly over the land. This is what we expected from the theory. Since the dynamics of the thermally-direct circulation in moist atmospheres is regulated by the gradient of the boundary layer entropy, the warm SST anomaly decreases the land-ocean contrast and therefore causes less rainfall over the land in spring. What is interesting in our experiment is that the SST anomaly not only influences the atmosphere over the ocean, but also changes the atmosphere over the land. This results in the apparent positive rainfall anomaly propagation onto the land. In addition, we see the rainfall anomaly persists about two to three months after the SST anomaly vanishes and maximizes in September.

The rainfall anomaly pattern caused by the spring SST anomaly is mainly associated with the change of circulation as can be seen from the anomaly pattern of large-scale moisture convergence (Fig. 5.36). Following the anomaly pattern of the moisture convergence, the soil moisture gets drier over the land during spring and early summer and then gets wetter as the rainfall arrives later on (Fig. 5.37). The moister soil in late summer produces more evaporation (Fig. 5.38) and therefore cooler land surface temperature (Fig. 5.39). The boundary layer entropy (expressed by θ_e) anomaly is basically consistent with the rainfall anomaly pattern, confirming the notion that the gradient of entropy dictates the intensity of monsoon circulations (Fig. 5.40). Next we will examine in more detail the role of individual processes in the development of the rainfall anomaly pattern shown in Figure 5.34.
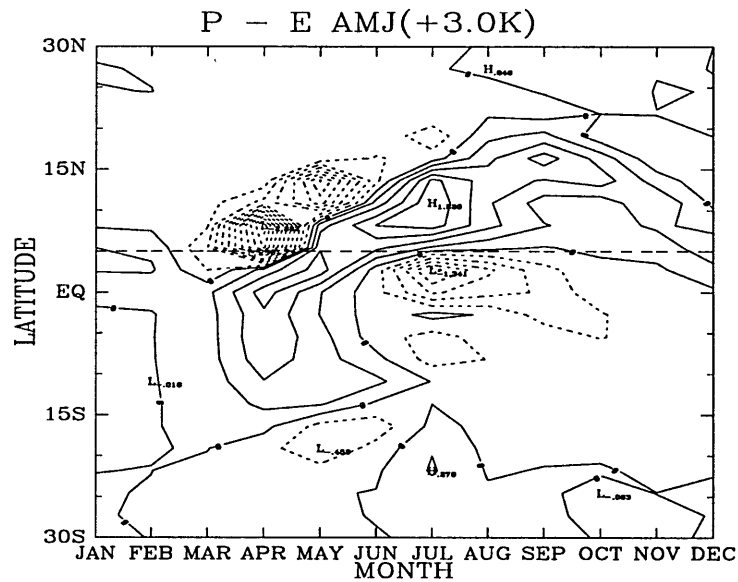
Figure 5.36: The moisture convergence $P - E$ anomaly caused by the specified SST anomaly (magnitude $T_{max} = 3.0$ K) for April-June, the contour interval is 0.25 mm/day.
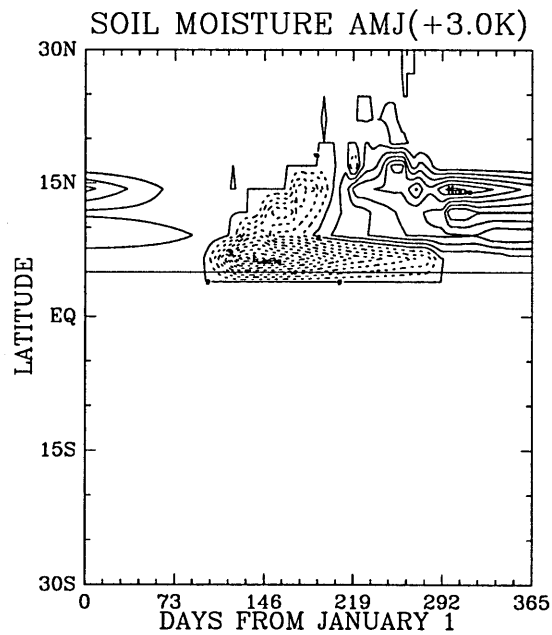
Figure 5.37: The relative soil moisture (in percentage) anomaly caused by the specified SST anomaly (magnitude $T_{max} = 3.0$ K) for April-June, the contour interval is 2.
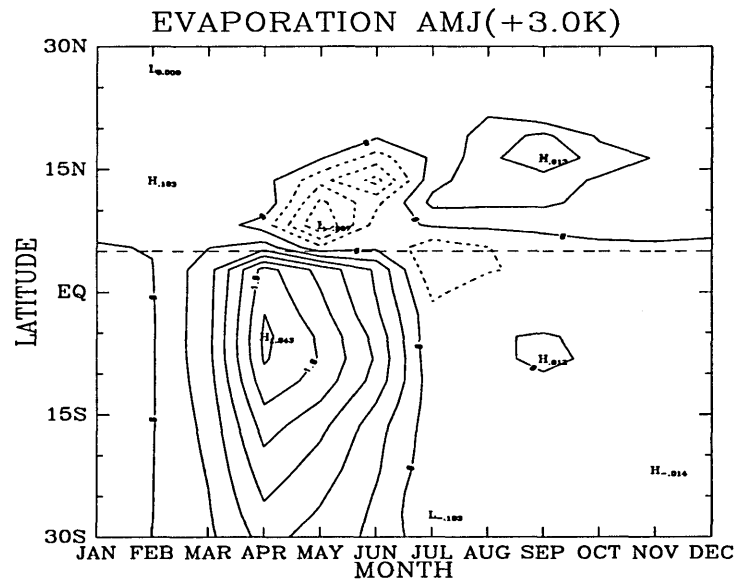
Figure 5.38: The surface evaporation anomaly caused by the specified SST anomaly (magnitude $T_{max} = 3.0$ K) for April-June, the contour interval is 0.2 mm/day.
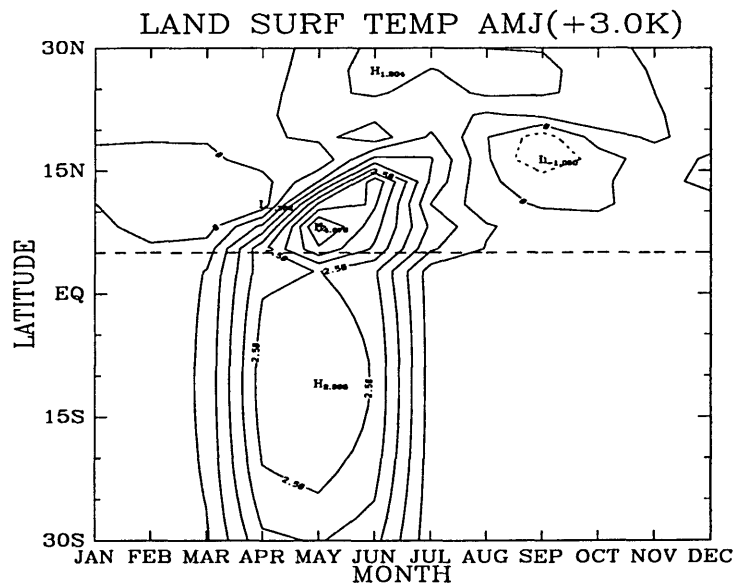
Figure 5.39: The land surface temperature anomaly (Kelvin) caused by the specified SST anomaly (magnitude $T_{max} = 3.0$ K) for April-June, the contour interval is 0.5 K.
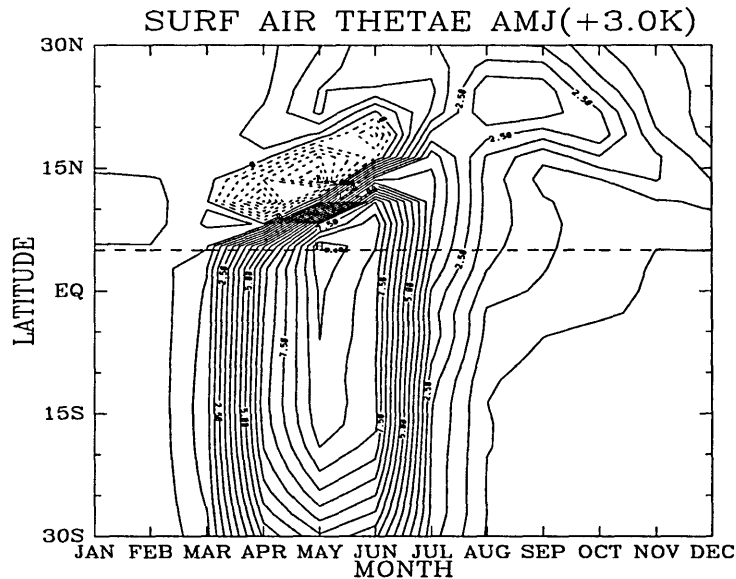
Figure 5.40: The boundary layer entropy anomaly (Kelvin) caused by the specified SST anomaly (magnitude $T_{max} = 3.0$ K) for April-June, the contour interval is 0.5 K.

5.5.2 Role of Soil Moisture

Soil moisture in our model has an effect on both surface albedo and evaporation. In general, other things being unchanged, the wetter the soil, the smaller the surface albedo and the more the surface evaporation. For the standard spring SST anomaly experiment we described above, soil moisture interacts with the atmospheric rainfall, i.e., the more the rainfall, the moister the soil. The moister soil can then provide more evaporation, feeding more rainfall. We can see that this soil moisture feedback is likely a positive one. To confirm this, we perform an experiment in which this feedback is artificially suppressed. In other words, the soil moisture is fixed the same as the control experiment through the model run — we don't allow the change of rainfall to change the soil moisture. We here describe an anomaly experiment with exactly the same SST anomaly (Fig. 5.33) as the standard spring SST anomaly experiment but with soil moisture fixed at the values of the control experiment. The resulting rainfall anomaly is shown in Figure 5.41. Apparently the rainfall anomaly cannot last

RAINFALL FIX SOIL AMJ(+3.0K)
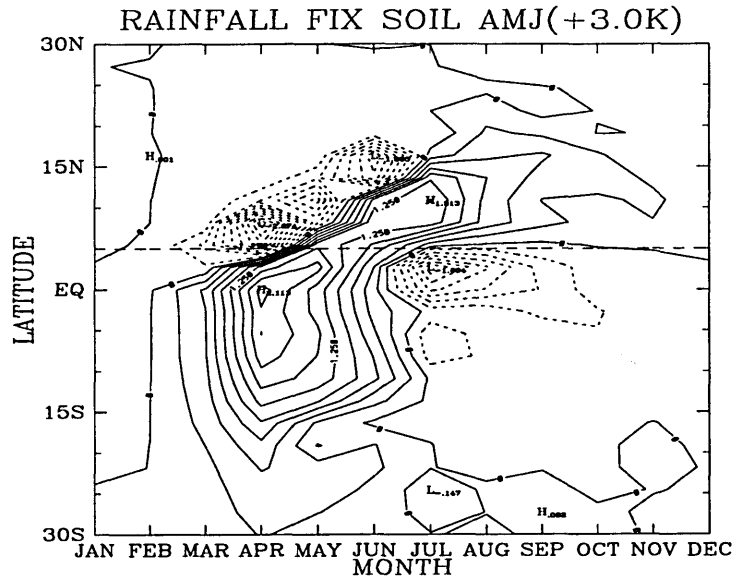
Figure 5.41: The total rainfall anomaly caused by the specified SST anomaly (magnitude $T_{max} = 3.0$ K) for April-June. The soil moisture is fixed the same as in the control experiment. The contour interval is 0.25 mm/day.

that long compared to the standard spring SST anomaly experiment (Fig. 5.34). For example, the rainfall anomaly maximum in September observed in the standard spring SST anomaly experiment disappears. By fixing the soil moisture, the rainfall anomaly vanishes effectively before September whereas for the standard anomaly experiment the rainfall anomaly lasts up to November. On the other hand, the rainfall anomaly migration pattern still exists. That is, the initial positive rainfall anomaly propagates onto the land after some time (about one to two months). The difference between this experiment and the standard spring SST anomaly experiment indicates the net effect of soil moisture-rainfall feedback, as shown in Figure 5.42. It is clear that the soil moisture-rainfall feedback sustains the initial rainfall anomaly two to three months longer than otherwise.

The time scale that the soil moisture anomaly is sustained can be estimated as follows. The soil moisture equation can be written as, following equation (5.2):
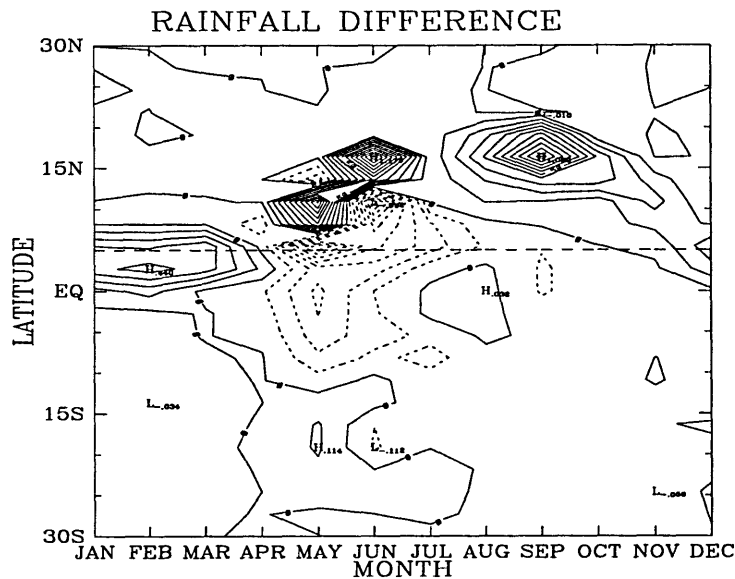
Figure 5.42: The net effect of soil moisture-rainfall feedback on rainfall, which is the difference between the standard spring SST anomaly experiment and the experiment in which the soil moisture is fixed as the control experiment. The contour interval is 0.10 mm/day.

$$\frac{\partial W}{\partial t} = P - \frac{E_p}{W_c}W.$$

From this, we see that the decay time scale of soil moisture can be approximated as $\frac{W_c}{E_p}$ (the precipitation P is a forcing mechanism instead). This time scale can be interpreted as the time scale the soil moisture anomaly is sustained (see Delworth and Manabe, 1988). Figure 5.43 shows the time scale estimated from this method. Although the damping time scale of soil moisture has large spatial and temporal variabilities, it ranges from one month to three months for the region south of 15°N. Roughly speaking, the soil moisture anomaly can be sustained for about two months on average in our model. This time scale explains why for the standard spring SST anomaly experiment, in which interactive soil moisture feedback is included, the rainfall anomaly lasts about two to three months longer than the experiment we described

in this section, in which the soil moisture is fixed. Notice that for the desert region (north of 20°N), the soil moisture damping time scale is a lot shorter because of much greater potential evaporation due to high surface temperature there.
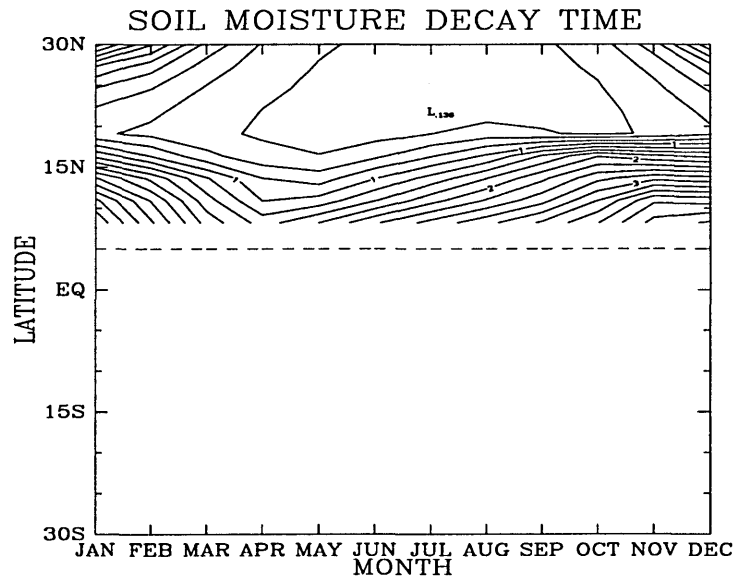
Figure 5.43: The damping time scale of soil moisture, contour interval is 0.25 months.

The experiment we described in this section suggests that the interactive soil moisture is essential for sustaining the rainfall anomaly. Without the feedback between rainfall and soil moisture, the rainfall anomaly caused by the imposed spring SST anomaly cannot sustain itself long enough to have substantial impact on the summer rainfall (especially late summer). However, the rainfall anomaly propagation pattern does not depend on whether soil moisture interacts with the atmosphere or not. The mechanisms for the initial rainfall anomaly propagation from over the ocean onto the land are our main focus below.

5.5.3   Role of Radiation

We have concluded that fixing soil moisture does not affect the rainfall anomaly propagation pattern observed in our standard spring SST experiment. Now let's examine if the radiative processes are relevant. We deliberately fix all the radiatively-

related variables exactly the same as the control experiment while imposing the same spring SST anomaly as in the standard anomaly experiment. The radiatively-related quantities are atmospheric cooling rates and surface fluxes, including longwave and shortwave components. By doing so, we do not allow the atmosphere to "feel" the SST anomaly radiatively. The rainfall pattern against that of the control experiment is displayed in Figure 5.44. We see that the essential pattern of rainfall anomaly is still there. Furthermore, the rainfall anomaly in this experiment seems to last longer than that in the standard spring SST anomaly experiment. For example, we even observe another rainfall anomaly maximum in October. Physically, the internal atmospheric anomaly caused by the imposed SST anomaly can only be eliminated by the radiative damping process. When the atmosphere gets warmer, it should emit more longwave radiation and vice versa. Not allowing this negative feedback makes it impossible to get rid of the atmospheric anomaly. Therefore, it is not surprising that rainfall anomaly lasts longer.
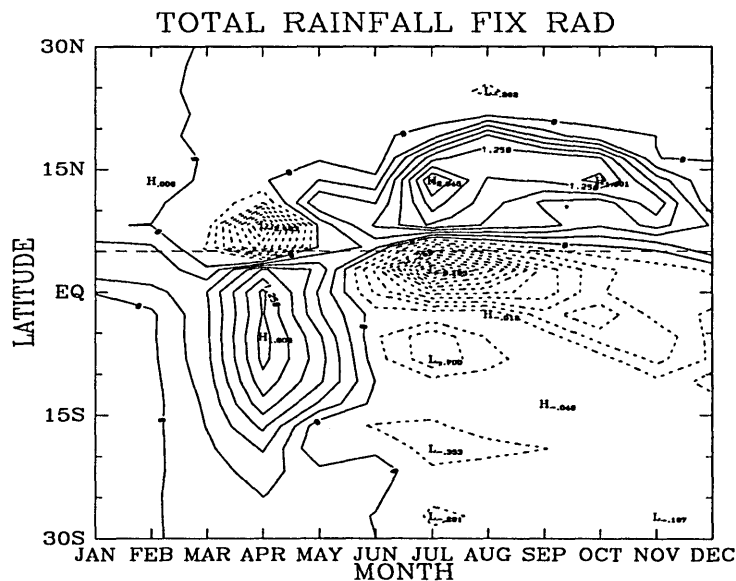
Figure 5.44: The total rainfall anomaly caused by the specified SST anomaly (magnitude $T_{max} = 3.0$ K) for April-June. The radiation is fixed the same as in the control experiment. The contour interval is 0.25 mm/day.

We know from the fixed soil moisture experiment that without interactive soil

moisture, the rainfall anomaly cannot last beyond September if we allow interactive radiative feedback. However, if we fix both radiation and soil moisture, as shown in Figure 5.45, the rainfall anomaly can persist up to November. This just confirms that radiative damping is crucial for eliminating the atmospheric anomaly.
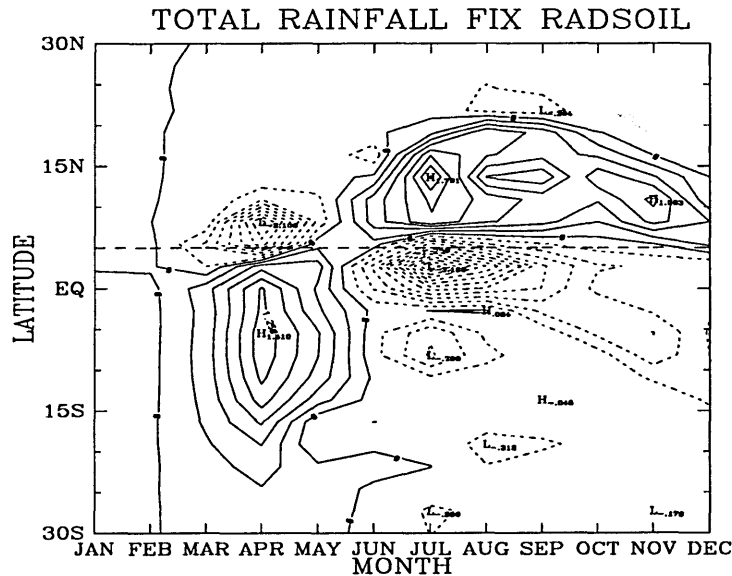
Figure 5.45: The total rainfall anomaly caused by the specified SST anomaly (magnitude $T_{max} = 3.0$ K) for April-June. The radiation and soil moisture are fixed the same as in the control experiment. The contour interval is 0.25 mm/day.

In summary, by fixing both radiation and soil moisture we still cannot shut down the rainfall anomaly propagation. Moreover, the rainfall anomaly propagation still exists even if we further turn off wind-flux feedback, i.e., setting the surface latent and sensible heat fluxes independent of wind speed. These experiments will serve as the basis for our subsequent theoretical analysis.

5.5.4 Role of Land Surface Temperature

The rainfall anomaly pattern caused by the spring SST anomaly appears to be very robust, even if we have fixed both radiation and soil moisture as we have discussed above. Now the question is: what exactly is the reason for the development of this

rainfall anomaly pattern?
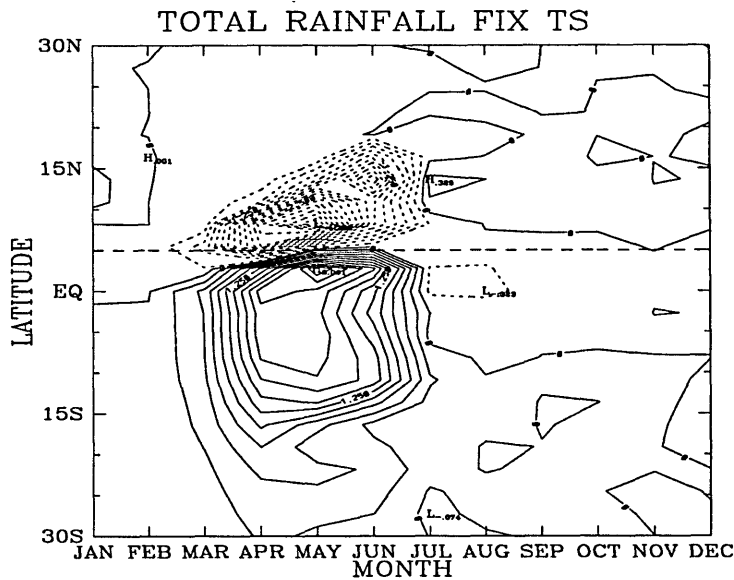
Figure 5.46: The total rainfall anomaly caused by the specified SST anomaly (magnitude $T_{max} = 3.0$ K) for April-June. The land surface temperature is fixed the same as the control experiment. The contour interval is 0.25 mm/day.

The following experiment gives us some clues. By fixing the land surface temperature the same as the control experiment, we can essentially shut down the rainfall anomaly pattern in the standard spring SST anomaly experiment, see Figure 5.46. This implies that whatever the mechanism is, it has to go through the land surface temperature. This leads us to consider the land surface temperature evolution. For theoretical simplicity, we consider the case where the surface net radiation, soil moisture remain unchanged. In addition, no wind-flux feedback is included. We know that the rainfall anomaly pattern does not depend critically on these constraints, as we have demonstrated through numerical experiments. Therefore, the essential mechanisms for the development of the rainfall anomaly should not be affected by these assumptions. The land surface temperature perturbation can then be expressed as follows:

$$C_E \frac{\partial T_s'}{\partial t} = -L_v \bar{w} \rho_s C_D V_0 \left(q_s(\bar{T}_s + T_s') - q_s(\bar{T}_s) - q_a' \right) - C_p \rho_s C_D V_0 (T_s' - T_a'), \quad (5.5)$$

where quantities with overbars denote the control state; quantities with primes denote perturbation with respect to the control state. To be specific, L_v is latent heat of vaporization; $\bar{w}$ relative soil saturation for the control state; ρ_s surface air density; C_D drag coefficient; V_0 surface wind magnitude; $q_s()$ surface saturation specific humidity for a given temperature; $\bar{T}_s$ land surface temperature for the control state; T_s' perturbation land surface temperature; q_a' surface air humidity perturbation; T_a' surface air temperature perturbation. Since T_s' is much smaller than $\bar{T}_s$, equation (5.5) can be approximated as:

$$C_E \frac{\partial T_s'}{\partial t} = -L_v \bar{w} \rho_s C_D V_0 \left(\frac{dq_s}{dT_s}\bigg|_{\bar{T}_s} T_s' - q_a' \right) - C_p \rho_s C_D V_0 (T_s' - T_a'). \quad (5.6)$$

By using Clausius-Clapeyron equation, we have:

$$\frac{dq_s}{dT_s} = \frac{L_v q_s}{R_v T_s^2},$$

where R_v is the gas constant for water vapor. Thus, equation (5.6) can be rewritten as:

$$\frac{\partial T_s'}{\partial t} = -\left(\frac{L_v^2 \bar{w}}{C_p R_v} \frac{\bar{q}_s}{\bar{T}_s^2} + 1 \right) \frac{T_s'}{\tau} + \left(\frac{L_v}{C_p} \bar{w} q_a' + T_a' \right) \frac{1}{\tau}, \quad (5.7)$$

where $\tau = \frac{C_E}{\rho_s C_D C_p V_0}$. For our model parameter values, $\tau \simeq 5$ days. In other words, the land surface temperature damping time scale is shorter than 5 days. On the other hand, the model rainfall anomaly (Fig. 5.34) and the accompanying land surface temperature anomaly pattern (Fig. 5.39) obviously have a much longer time scale (~ 1 month). It appears that this longer time scale can only be explained by the atmo-

spheric anomalies caused by the imposed SST anomaly. The atmospheric anomalies (e.g., T'_a and q'_a) can be viewed as forcing factors of the land surface temperature anomaly, as indicated by equation (5.7).

Since the land surface temperature damping time scale (about 5 days) is much shorter than the rainfall anomaly propagation time scale we are concerned with (~ 1 month), we can then assume zero heat capacity for the land surface for simplicity. This gives us an instantaneous balance between the land surface temperature anomaly and the anomalies of near surface atmospheric temperature and humidity (atmospheric forcings):

$$\left(\frac{L_v^2 \bar{w}}{C_p R_v} \frac{\bar{q}_s}{\bar{T}_s^2} + 1 \right) T'_s = \left(\frac{L_v}{C_p} \bar{w} q'_a + T'_a \right). \tag{5.8}$$

Equation (5.8) makes it clear that the time variation of the land surface temperature anomaly is dictated by the time variations of the atmospheric anomalies (q'_a and T'_a). The atmospheric adjustment time scale to the imposed SST anomaly will be discussed in the next section.

Rewriting equation (5.8), we have:

$$H'_a = C_p T'_a + L_v q'_a = \left(\frac{L_v^2 \bar{w} \bar{q}_s}{R_v \bar{T}_s^2} + C_p \right) T'_s + (1 - \bar{w}) L_v q'_a, \tag{5.9}$$

where H'_a is the surface air moist static energy perturbation.

From the definition, we know that H'_a has essentially the same pattern as that of the perturbation of boundary layer entropy (θ'_e). Therefore, like θ'_e, H'_a is also the key quantity in moist atmospheres. Figure 5.47 shows the anomaly pattern of H'_a/C_p (this quantity has the same dimension as θ'_e in Kelvin) for the standard spring SST anomaly pattern. It is evident that H'_a/C_p pattern is almost identical to θ'_e (see Fig. 5.40).

Now referring to equation (5.9), we see that H'_a is closely related to the land surface temperature perturbation T'_s, which in turn is closely related to atmospheric

172
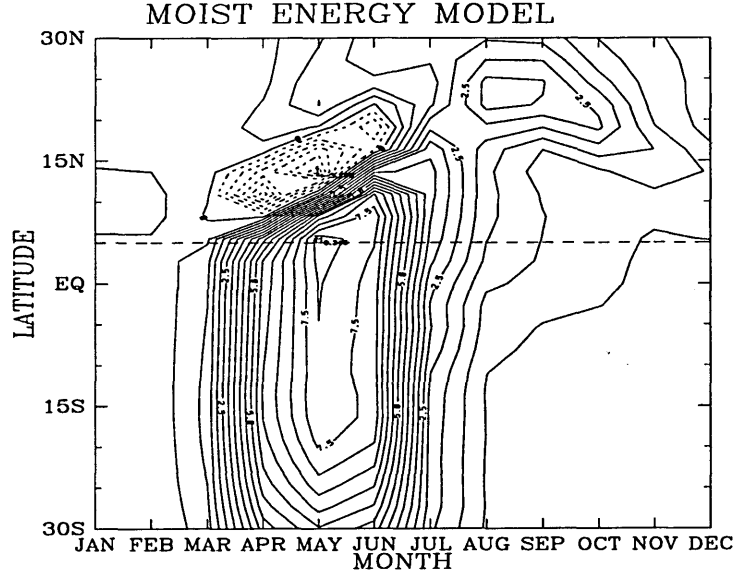
Figure 5.47: The H'_a/C_p anomaly (Kelvin) caused by the specified SST anomaly (magnitude $T_{max} = 3.0$ K) for April-June, the contour interval is 0.5 K.

anomalies (eq. (5.8)). Since soil moisture has been proved not to be critical for the rainfall anomaly propagation, we consider the case where the soil is saturated (like ocean surface) so that H'_a is totally determined by T'_s. In fact, our experiments show that T'_s and T'_a have very similar spatial and temporal pattern. Furthermore, the magnitude of T'_a is generally smaller than that of T'_s. So if we assume that $T'_a = \gamma T'_s$ $(0 < \gamma < 1)$, from equation (5.8) and equation (5.9), we have

$$\frac{H'_a}{C_p} = \left[\frac{L_v^2 \bar{q}_s}{C_p R_v \bar{T}_s^2} + \frac{1 - \gamma(1 - \bar{w})}{\bar{w}} \right] T'_s. \tag{5.10}$$

Now we see the importance of an interactive land surface temperature perturbation.

In this section, we identified that the land surface temperature has to "feel" the imposed SST anomaly for the rainfall anomaly propagation. Since the time scale of this propagation is of the order of one month or so and the land surface temperature damping time scale is less than 5 days, we concluded that the atmospheric anomalies must be the reason for the rainfall anomaly propagation. The land surface temperature almost instantly responds to changes of the near surface atmospheric temperature

and specific humidity (eq. (5.8)). The change of the land surface temperature then sustains the atmospheric anomalies caused initially by the SST anomaly. We see that the interaction between the atmosphere and the underlying land surface is crucial for the rainfall anomaly propagation. In our hypothetical experiment in which we artificially fixed the land surface temperature as the control experiment, we essentially shut down this land-atmosphere interaction, therefore the rainfall propagation pattern vanishes.

In what follows, we will conduct a hypothetical numerical experiment just to look at the atmospheric response time scale to the imposed SST anomaly.

5.5.5   The Atmospheric Response to SST Anomaly

For an imposed SST anomaly, the atmosphere over the ocean feels it immediately. This can be illustrated as follows. The SST anomaly influences the surface air moist static energy through turbulent fluxes. The change of the boundary layer moist static energy perturbation (H') due to surface fluxes can be expressed as:

$$\frac{\partial H'}{\partial t} = C_D V_0 (H'_s - H')/\Delta z, \qquad (5.11)$$

where $H'_s = C_p T'_s + L_v q'_s$ is the perturbation of oceanic saturation moist static energy due to the imposed SST anomaly T'_s; Δz is the depth of the boundary layer. All other notations are defined in the last section. Following similar manipulations, we have:

$$\frac{\partial H'}{\partial t} = \frac{H'_s - H'}{\tau_o} = \frac{\left(C_p + \frac{L_v^2 \bar{q}_s}{R_v T_s^2}\right) T'_s}{\tau_o} - \frac{H'}{\tau_o}. \qquad (5.12)$$

The above equation can be rewritten as:

$$\frac{\partial \left(\frac{H'}{C_p}\right)}{\partial t} = \frac{1}{\tau_o}\left(1 + \frac{L_v^2 \bar{q}_s}{C_p R_v \bar{T}_s^2}\right) T'_s - \frac{\frac{H'}{C_p}}{\tau_o}, \qquad (5.13)$$

where $\tau_o = \frac{\Delta z}{C_D V_0}$. This is the oceanic boundary layer air response time scale to the imposed SST anomaly T_s'. For typical values: $\Delta z \sim 500\text{m}$; $C_D \sim 10^{-3}$; $V_0 \sim 5\text{ms}^{-1}$; we get $\tau_o \sim 1$ day. Now we see that the oceanic surface air responds to the imposed SST anomaly almost immediately by the turbulent mixing.

In order to isolate the remote (land) atmospheric response time scale from the seasonal time scale of the solar forcing, we perform an experiment using the steady-state model of Chapter 4. The control state there was a steady-state solution using the solar insolation of August. On top of this control experiment, we switched on an SST anomaly at time zero with the form: $T_s' = T_{max} e^{-(\frac{\phi-\phi_c}{\delta\phi})^2}$, where T_{max} is the magnitude; ϕ latitude; ϕ_c latitude of the maximum T_s'; $\delta\phi$ half width in latitude. Here we take $T_{max} = 3.0\text{K}$; $\phi_c = 10°\text{S}$; $\delta\phi = 30°$. The spatial pattern of the SST anomaly is exactly the same as anomaly experiments we have discussed above. However, once the SST anomaly is switched on from the beginning of the experiment, it stays there forever. In other words, no time variation of SST anomaly is included. The rainfall anomaly (against the control state) is shown in Figure 5.48. It is obvious that the system takes 40-50 days to adjust the SST anomaly to the final steady state. Initially, with the switch-on of the warm SST anomaly, the land area experiences anomalous subsidence like all the other experiments we have shown in this chapter. But after about 40-50 days, a strip of positive rainfall anomaly centered at around 15°N emerges. South of this strip of positive rainfall anomaly, a band of negative rainfall anomaly is observed.

The moist static energy anomaly shows that the oceanic air almost instantly adjust to the imposed the SST anomaly whereas it takes substantial amount of time (tens of days) for the remote land air to "feel" the SST anomaly (see Fig. 5.49). The atmospheric adjustment time scale seems to be consistent with the time scale we observed for the rainfall anomaly pattern to propagate onto the land for the standard spring SST anomaly experiment.
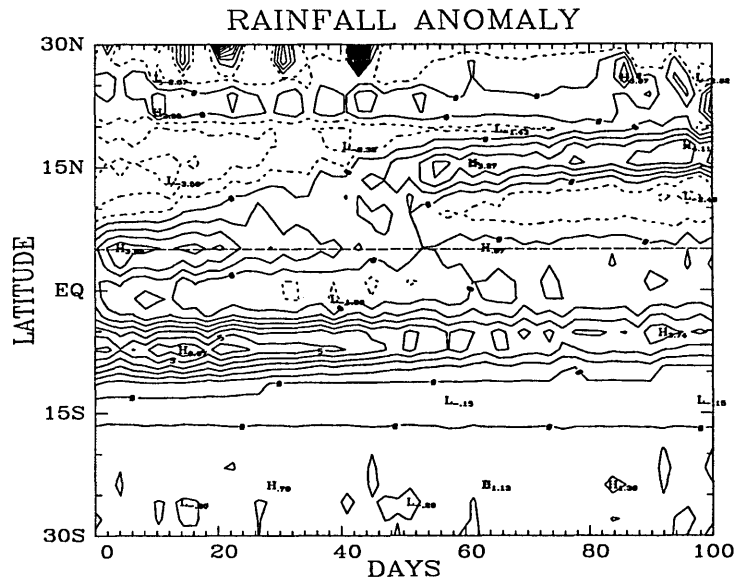
Figure 5.48: The rainfall anomaly evolution for a time-invariant SST anomaly. The contour interval is 1 mm/day.
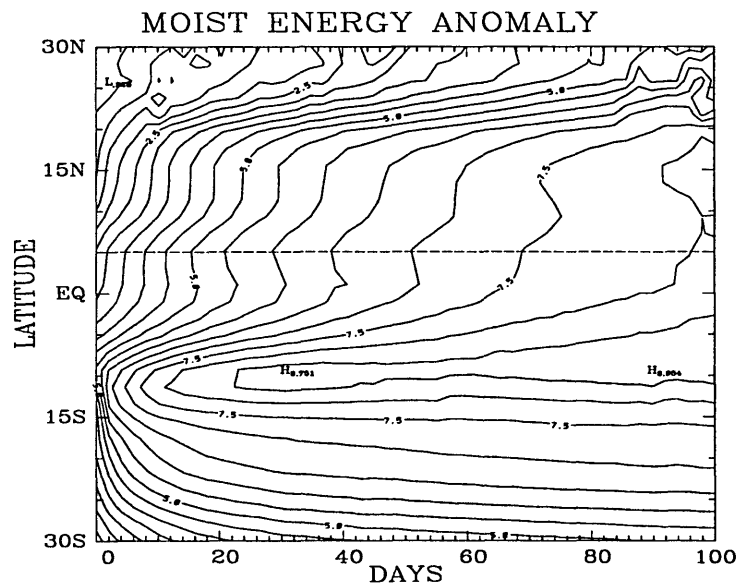
Figure 5.49: The surface moist static energy anomaly (H'/C_p) evolution for a time-invariant SST anomaly. The contour interval is 0.5 K.

5.5.6 Discussion

From what we have discussed in previous sections, we see clearly that in our model the spring SST anomaly can produce the observed rainfall anomaly pattern. That is, the propagation of rainfall anomaly from over the ocean onto the land, which is evidenced by the comparison between 1992 and 1994 based on observations, can be caused by the imposed spring SST anomaly. While we know that the West African monsoon and rainfall are influenced by both land and oceanic processes, it is obvious that land and ocean cannot be considered separately. Our imposed SST anomaly not only influences the atmosphere over the ocean, but also influences the atmosphere over the remote land area through complicated processes. Our focus here is to identify these processes.
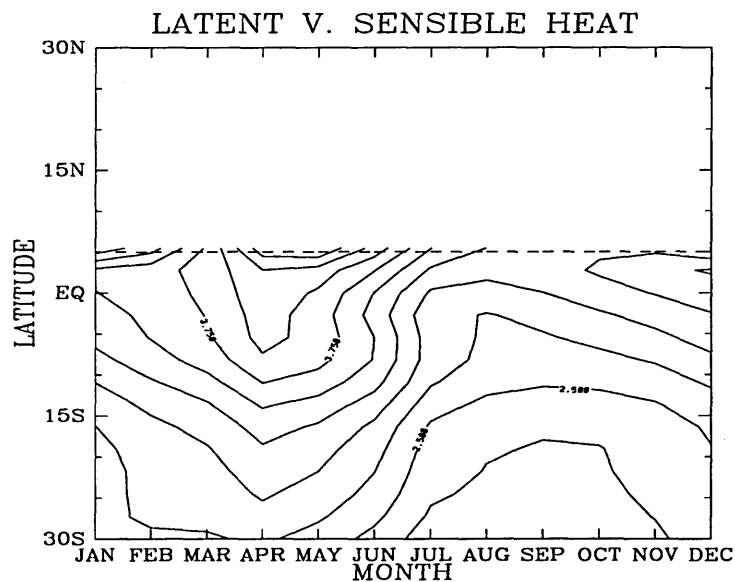
Figure 5.50: The relative contribution to the oceanic boundary layer moist static energy caused by the imposed SST anomaly, expressed as the ratio between the effect of the latent heat flux and that of the sensible heat flux. The contour interval is 0.25.

The three-way interactions among ocean, land and atmosphere have been proved to be crucial for the rainfall anomaly pattern, as shown in Figure 5.34. With the imposed warm SST anomaly, the boundary layer entropy or moist static energy over

the ocean increases immediately (Section 5.5.5). The increase of the moist static energy (or entropy) within the oceanic boundary layer is due to the increase of both latent heat and sensible heat fluxes. From equation (5.13), we know that the ratio between the relative contribution of latent heat flux and sensible heat flux can be approximately expressed by $\frac{L_v^2 \bar{q}_s}{C_p R_v T_s^2}$, shown in Figure 5.50. This shows that the oceanic evaporation plays a more important role in enhancing the oceanic boundary layer moist static energy (or entropy). Since the increase of oceanic boundary layer entropy is achieved within much shorter time than that of the land boundary layer entropy (Fig. 5.49), the meridional gradient of entropy between land and ocean at early stage (before the land surface air entropy anomaly becomes significant) reduces. As a result, an anomalous subsidence over the land and an anomalous updraft over the ocean are expected.

In order to have the rainfall anomaly propagation, the boundary layer entropy or moist static energy over the land (especially coastal land) has to increase enough to overcome the already enhanced oceanic boundary layer entropy or moist static energy. The only way to achieve this is through the dynamical transport of moist static energy from the ocean, where there is an increase of energy due to warm SST anomaly, onto the land. That is, a low-level southerly is needed to advect the enhanced moist static energy over the ocean onto the land. Therefore, a suitable match between the timing of SST anomaly and the timing of the monsoon onset is crucial for the anomalously larger oceanic boundary layer entropy to influence the land boundary layer entropy and rainfall. We showed in Section 5.4 that the winter (October-March) SST anomaly has the least influence on summer rainfall simply because of the mismatch between the timing of the SST anomaly and the timing of the monsoon onset for the control run (see Fig. 5.31 and Fig. 5.32). The greatest latitudinal extent that the rainfall anomaly can propagate is regulated by the circulation in the control experiment. This is evident in the summer SST anomaly experiment (Fig. 5.35) where the rainfall anomaly cannot propagate as far as that of the standard spring SST anomaly experiment (Fig. 5.34)

since the monsoon circulation starts to retreat during late summer and early fall.

We also see that the interaction between the atmosphere and the underlying land surface is critical for the rainfall anomaly propagation (Section 5.5.4). The land surface temperature responds to changes of the atmosphere quickly ($\sim$ 5 days) and can be thought as in balance with the atmosphere (eq. (5.8)). The land surface temperature anomaly in turn sustains the atmospheric anomalies. We have shown that the land boundary layer moist static energy is closely related to the land surface temperature, explaining why not allowing the change of the land surface temperature denies the rainfall anomaly propagation (eq. (5.10)). Since the time scale ($40-50$ day from Section 5.5.5) of the rainfall anomaly propagation cannot be explained by the land surface, it has to be inherent in the atmosphere itself. It seems that the observed time scale of $\sim$ 40 days should be related to the overturning time scale of the monsoon circulation, which in turn is controlled by the atmospheric radiative damping time scale ($\sim$ 10-30 days). The characteristic time scale of atmospheric adjustment to the switch-on of an SST anomaly we found in Section 5.5.5 should also be the same as the the adjustment time scale of the switch-off of an SST anomaly. In other words, the atmospheric memory of an SST anomaly can only last as long as a month or so. This is what we have seen in the experiment of fixing soil moisture (Fig 5.41). The soil moisture and rainfall feedback is able to sustain the rainfall anomaly to another two to three months (Section 5.5.2).

The changes of the boundary layer water vapor and temperature can be ultimately traced to the imposed warm SST anomaly. The increase of SST basically injects more moisture and sensible heat content into the oceanic boundary layer, contributing to the increase of the moist static energy within the boundary layer. The land boundary layer feels this anomalous moist energy through the overturning monsoon circulation. From Figure 5.50, we know that the input of higher water vapor is substantially more important than the input of wamer temperature, in terms of their relative role in contributing the overall increase of moist energy. In fact, if we artificially turn

off the anomalous oceanic evaporation due to the warm SST anomaly, the rainfall anomaly pattern vanishes. On the other hand, if we allow the anomalous oceanic evaporation, no matter whether we shut down the anomalous land evaporation or not, the rainfall anomaly propagation still exists. These experiments suggest that the input of more moisture into the atmosphere by the imposed warm SST anomaly is the dominant factor for the increase of moist static energy (or entropy) over the land later on. The observations also confirm that the boundary layer entropy anomaly is largely determined by the surface air humidity anomaly (comparing Fig. 5.10 with Fig. 5.12). For the standard spring SST anomaly experiment, the boundary layer moist static energy anomaly, as shown in Figure 5.47, is also mostly due to the surface air humidity anomaly, as shown in Figure 5.51.
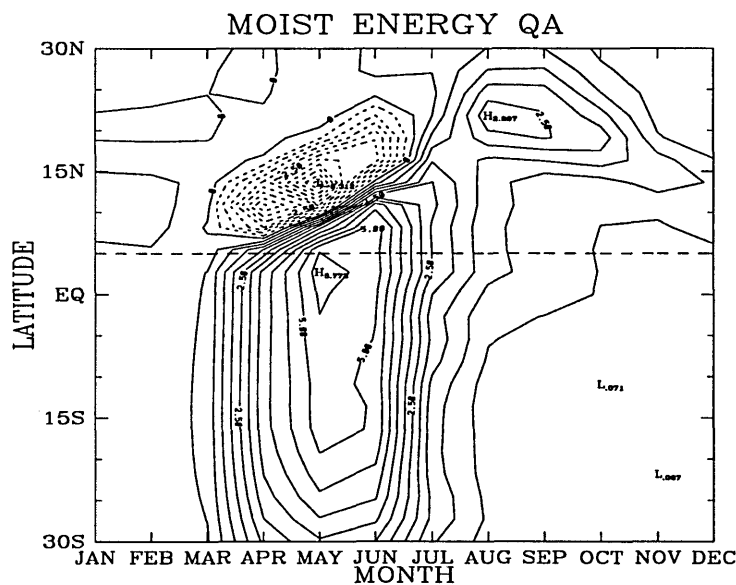
Figure 5.51: The $\frac{L_v}{C_p}q_a'$ anomaly (Kelvin) caused by the specified SST anomaly (magnitude $T_{max} = 3.0$ K) for April-June, the contour interval is 0.5 K.

5.6 Model Response to the Observed SST Anomaly Pattern

So far we have mainly concentrated on the model response to hypothetical SST anomalies because our main goal here is to use the model as a tool to explore mechanisms. In this section, we are particularly interested in comparing the model responses to the 1992 and 1994 SSTs. As revealed by the observation, the rainfall difference pattern between 1994 and 1992 shows that the rainfall anomaly seems to originate from the spring SST anomaly, see Figure 5.4 and Figure 5.3c. Two anomaly experiments are performed here. First, we impose an SST anomaly such that the actual SST equals that of 1992 (recall that our control run is forced by the SST climatology from 1981-1995). Secondly, we impose an SST anomaly such that the actual SST equals that of 1994. For both experiments, for the sake of clearness, we set the SST anomalies zero for winter months (October-March), which have been shown to be insignificant for summer rainfall variability.
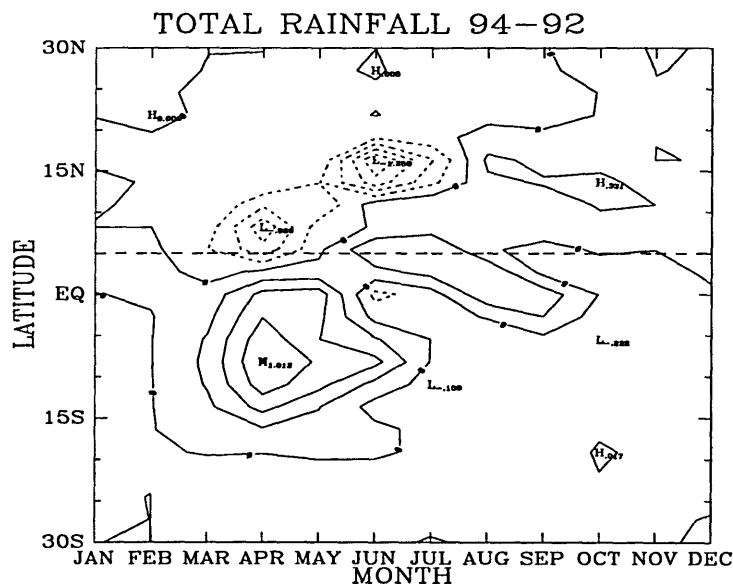
Figure 5.52: The total rainfall difference forced by SST difference between 1992 and 1994. The contour interval is 0.25 mm/day.

The difference between the two anomaly experiments is solely due to the difference of SST between 1994 and 1992, which is shown in Figure 5.4 except that the anomalies in winter months have been set to zero. The model rainfall difference pattern between the two years is shown in Figure 5.52. We see that the observed SST difference between 1992 and 1994 is able to force a similar rainfall difference pattern to that shown in Figure 5.3c. However, the magnitude of the model rainfall difference is a lot smaller than that of the observation. We would like to point out that although the rainfall difference is small, it is significant, comparing with the rainfall variance for the control experiment (Fig. 5.20). There are many reasons why the model rainfall difference is smaller than that of the observation. Among them, the most possible reason might be model deficiencies. For example, the model does not include any zonal asymmetries such as synoptic disturbances. It would be very interesting to see if a GCM can produce the similar rainfall anomaly (against the observation) by the observed SST difference between 1992 and 1994. Other possible reasons include influence of other oceans (Folland *et al.*, 1986; Rowell *et al.*, 1995) and possible differences for other circulation systems (such as Asian monsoons) that may affect the intensity of West African monsoons between 1992 and 1994 (Webster and Chou, 1980a). To reiterate, our model is designed as process model. While it does not simulate the details of the real atmosphere, it does provide us an opportunity to explore physical mechanisms (as we did earlier) which should further be tested against more realistic models and observations.

5.7 Summary

In this chapter, we are mainly concerned with the possible role of SST anomaly (spring SST anomaly in particular) in the dynamics of West African monsoons and rainfall variability, focusing on mechanisms. Our main findings are:

(1). The case study between the 1994 wet year and the 1992 dry year suggests that the

spring SST anomaly might be important for the observed rainfall anomaly pattern (Section 5.2). While most previous studies focus on the instantaneous correlation between the summer SST anomaly and the summer rainfall, we hypothesize that the spring SST anomaly can be a potentially important predictor for the summer rainfall over West Africa. The remarkable consistencies among various independent data sets seem to enhance the robustness of our analyses.

(2). We use a numerical model to explore the mechanisms of how a spring SST anomaly can influence the summer rainfall over West Africa. Our goal here is to identify physical mechanisms that might be relevant in the real world, not to simulate the real monsoon in detail. Nevertheless, the model simulates the observed West African summer rainfall reasonably well. In particular, the location of the model ITCZ and the north-south gradient of the rainfall agree quite well with the observations. The model winter climatology deviates from the observation substantially due to the deficiencies of the model (Section 5.3). For the model control experiment, the boundary layer entropy is similar in spatial and temporal patterns to those of the observation but is quite different from the observation quantitatively. This implies that the model's sensitivity to the surface anomaly such as SST anomaly may be quite different from the reality. However, since the model anomaly *pattern* is our major concern here, the model should be credible enough to address mechanisms of rainfall anomaly patterns.

(3). The rainfall anomaly pattern caused by the imposed spring SST anomaly is similar to that of the observation (Section 5.4). That is, the initial positive rainfall anomaly over the ocean caused by warm SST anomaly propagates onto the land as season marches. This indicates that the spring SST indeed can influence the summer rainfall significantly. In general, the spring SST anomaly is positively correlated with the summer rainfall. This finding suggests that the spring SST can be used as a predictor of the summer rainfall, as done by Owen and Ward (1989).

(4). The rainfall anomaly follows closely to the change of the monsoon circulation

due to the imposed SST anomaly. The rainfall anomaly persists about two to three months even after the SST anomaly is completely turned off. The interaction between soil moisture and rainfall is crucial for sustaining the rainfall anomaly (Section 5.5.2).

(5). The rainfall anomaly propagation is found to be associated with the transport of the anomalously larger oceanic boundary layer entropy due to the warm SST anomaly through the overturning monsoon circulation. Because the spring SST anomaly matches very well with the timing of monsoon onset (for the control experiment), the land surface feels through the land surface temperature. The land surface temperature responds to the atmospheric changes quickly and sustains the atmospheric anomalies. The interaction between the atmosphere and the underlying land surface is critical to the rainfall anomaly propagation. Not allowing this interaction essentially shuts down the rainfall anomaly propagation (Section 5.5.2). Under some assumptions, the land surface temperature perturbation is shown to be directly associated with the land boundary layer moist static energy anomaly (equation (5.10)). This explains the critical importance of an interactive land surface to the rainfall anomaly propagation.

(6). The rainfall anomaly propagation time scale is found to be inherent in the atmosphere. It is found that the time scale is about 40-50 days (Section 5.5.5). We suggest that it is the atmospheric radiative damping time scale that ultimately determines the atmospheric adjustment time scale to the imposed SST anomaly (Section 5.5.6).

(7). The input of more water vapor into the atmosphere due to warm SST anomaly is far more important than the input of more sensible heat into the atmosphere. For given SST anomaly, the contribution to the oceanic boundary layer moist static energy by the evaporation is in general 2-4 times as large as that due to sensible heat flux (see Fig. 5.50). Our numerical experiments also confirm that the boundary layer entropy (or moist static energy) anomaly, which regulates the dynamics of West African monsoons, is largely associated with the surface air humidity anomaly. This is consistent with our case study from the observations (Section 5.2). In addition, if we

do not allow increase of water vapor content due to SST anomaly (by fixing oceanic surface evaporation as the control run), the rainfall anomaly propagation vanishes (Section 5.5.6).

(8). The observed SST difference between 1992 and 1994 can produce the rainfall anomaly pattern but not magnitude (Section 5.6). This may be due to the deficiencies of the model. Studies with more realistic models are needed.

Chapter 6

Conclusions

6.1 Main Results

In this thesis, we adopted the simplest theoretical paradigm of monsoons — zonally-symmetric thermally-direct circulations. This paradigm offered tremendous theoretical simplicity, allowing us to understand the physical processes. We used numerical models to explore the physical mechanisms within the framework of zonal symmetry. The use of of zonally-symmetric models provided computational efficiency. The models were designed to focus on the essential processes in real monsoons.

Since moist processes are critical in real monsoons, we built our models by including an explicit hydrological cycle. In addition, based on theories reviewed in Chapter 1, nonlinear primitive equations were used. These two features are common to all models used in our studies. For applications to West African monsoons, we also included the land surface processes so that the land surface properties (such as land surface temperature and soil moisture) can respond to atmospheric changes. The simplicity of our models makes it possible for detailed study of the physical mechanisms. Our main conclusions are:

I. By including an explicit hydrological cycle, we were able to investigate

how the moisture-dynamics feedback affected the threshold behavior of the atmospheric response to the specified subtropical thermal forcing proposed by Plumb and Hou (1992). We found that even though we allowed the interaction between the large-scale circulation and the moist convection, the threshold behavior of the moist atmospheres to subtropical surface temperature perturbations was not influenced qualitatively. It was argued that the dynamical constraint of upper level absolute vorticity was the reason for the existence of sub-critical and super-critical regimes.

II. We also examined the possible impact of transient surface temperature perturbations with seasonal time scales on the threshold behavior. It was very clear from our numerical experiments that the upper level absolute vorticity regulated the atmospheric response to the forcings. When the forcing magnitude was large enough, the model response (e.g., rainfall and zonal wind) displayed a sudden increase, which coincided with the vanishing of upper level absolute vorticity and marked the onset of the strong thermally-direct circulation. We speculated that the observed abrupt increase of rainfall and wind during the monsoon onset was associated with the pure dynamical constraint of the system — upper level absolute vorticity.

III. For a super-critical regime where a strong meridional circulation emerged, our model boundary layer entropy agreed reasonably well with the theoretical prediction by Emanuel (1995). The onset of the circulation drove the distribution of boundary layer entropy to the theoretical critical state.

IV. We used our model to investigate the role of vegetation in the dynamics of West African monsoons. The West African monsoons were found to

be critically dependent on the location of the vegetation perturbations. Specifically,

(1). Changes in vegetative cover along the southern edge of the Sahara desert (desertification) had a minor impact on the simulated monsoon circulation. These changes merely reduced the local rainfall within the perturbation region, but a healthy monsoon circulation still developed.

(2). Changes in vegetative cover along the tropical Atlantic coast could have a dramatic impact on the simulated atmospheric response. The observations showed ever-growing deforestation in West Africa. Our study suggested that the tropical West African deforestation might be another drought mechanism of West African region, besides generally accepted sub-Saharan desertification. We showed empirical evidence that the tropical deforestation was favored over sub-Saharan desertification in causing the observed African drought.

(3). The location of the ITCZ was found to be sensitive to changes in the vegetation northward or southward from the location of the ITCZ in the control experiment. However, the location of the ITCZ was sensitive to changes of the vegetative cover in the immediate vicinity of the location of the ITCZ. This had important implications to GCM studies, i.e., the model response to the same vegetation perturbation might be different simply because of the difference in model control runs, in particular, the difference of the location of ITCZ in the control experiment for different models.

V. We also explored the possible impact of a tropical Atlantic SST anomaly on the West African monsoon and rainfall, motivated by a case study comparing 1992 and 1994 (the driest and wettest years in 1990s so far). The observations showed remarkable consistencies among rainfall, upper level divergence and boundary layer entropy. We hypothesized that the unique spring SST difference pattern (warm SST anomaly in spring) might be important in causing the rainy year of 1994.

VI. The spring SST anomaly was found to be capable of causing the observed rainfall anomaly pattern. That is, the spring SST anomaly first caused a positive rainfall anomaly locally. Then this positive rainfall anomaly propagated onto the land. Even after the complete turn off of the SST anomaly, the rainfall persisted for another two to three months. This suggested that the spring SST was positively correlated with the summer rainfall and could be an important predictor of the summer rainfall.

VII. The rainfall propagation from ocean to land was found to be associated with the transport of the larger oceanic boundary layer entropy (caused by the imposed SST anomaly) through monsoon circulation. It was found that a responsive land was crucial for the rainfall propagation. Specifically, the land surface temperature had to feel the remote SST anomaly in order to sustain the atmospheric anomalies. Under some assumptions, we demonstrated that the land surface temperature perturbation was related to the boundary layer moist static energy perturbation. This explained why an interactive land surface temperature was crucial for the rainfall propagation. We emphasized the notion that the West African monsoon and rainfall were essentially regulated by three-way interactions between ocean, land and atmosphere. These interactions were critical in creating the rainfall anomaly propagation from over the ocean onto the land. It was clear that the rainfall variability over West Africa could not be studied from either the land or the ocean perspective in insolation, but must be viewed as an interaction between the two.

VIII. The soil moisture and rainfall feedback was found to be a positive one. It was this feedback that sustained the anomalous rainfall even if the

SST anomaly vanished. In general, the soil moisture had a memory time scale of two to three months.

We identified two important West African drought/flood mechanisms using our simple process models. Namely, the role of ever-growing tropical deforestation on the Sahel drought and the impact of spring SST anomaly on the West African wet year in 1994. The simple models also allowed us to explore the mechanisms in great detail. However, what we compromised on was the accurate simulation of real monsoons. For example, the magnitude of rainfall difference forced by the observed SST difference between 1994 and 1992 was substantially smaller than that in the observations (Section 5.6). In what follows, we will discuss an outline of future directions for this research.

6.2 Future Work

The models used in this thesis are much simpler than GCMs in the sense that we have neglected many important processes in the real atmosphere. Most notably, our models simply do not include any zonally-asymmetric disturbances. These disturbances, such as easterly waves in West Africa, are real rain-producing systems. By excluding these synoptic disturbances, we basically shut down most of the model internal variabilities such as dynamical instability that produces observed synoptic eddies. In other words, our models only describe the influence of boundary layer forcings (land surface conditions, SST) on the monsoon and rainfall. In support of our assumptions, Rowell *et al.* (1995) demonstrated that the boundary layer forcing was dominant over the internal variability in terms of interannual variability of seasonal rainfall.

While our models are useful in identifying and understanding physical mechanisms, the simplicity of the model framework presents some serious deficiencies. For example, the model sensitivity to the boundary layer forcing such as an SST anomaly deviates from the reality substantially. One of the important results in this thesis is

that an spring SST anomaly may be able to produce the observed rainfall anomaly pattern. However, our study has not proven that the observed SST anomaly can indeed cause the observed magnitude of rainfall anomaly. In fact, our model in Chapter 5 fails to get the correct magnitude of the rainfall anomaly even if we forced the model with the observed SST anomaly (Section 5.6). In order to resolve this issue, more realistic models are needed. One possible tool is a three-dimensional regional model for West Africa. The Second-Generation Regional Climate Model (RegCM2) of the National Center for Atmospheric Research (NCAR) is a possible choice (e.g., Giorgi *et al.*, 1993a; Giorgi *et al.*, 1993b). We can force the model with the identical lateral boundary conditions but with different SST distributions, one with 1992 SSTs and the other with 1994 SSTs. The study can isolate the effect of the tropical Atlantic SST on the rainfall variability. If the observed SST difference between 1992 and 1994 can produce the observed rainfall anomaly magnitude, we can conclude that the unique SST distribution in 1994 is indeed responsible for the wet year of 1994.

Three dimensional models ought to be more realistic than our two dimensional process models. Unfortunately, no model (including the widely-used GCMs) is perfect. While modeling is definitely useful in understanding mechanisms, some model results can be very misleading. On one hand, we have to depend on models to test our hypotheses. On the other hand, the confirmation from one model does not necessarily mean that our hypotheses are correct. Conversely, a failure from one model may not necessarily mean that our hypotheses are incorrect. For example, Rowell *et al.* (1995) hypothesized that the global SST variability was mainly responsible for the rainfall interannual variability in West Africa. They were able to confirm their hypothesis using an older version of UKMO (United Kingdom Meteorological Office) climate model. However, they also pointed out the more recent version of UKMO climate model failed to simulate the interannual variability of West African rainfall whereas their older version of the model did a decent job.

One of the largest uncertainties in climate models is in the parameterization of

moist convection. Even within the model dynamical framework, the model behavior can be very different depending on the choices of convective schemes. While we use models to perform sensitivity experiments, we have to be very careful in choosing convective schemes. Some of the widely-used convective schemes such as Kuo scheme have been shown to be unphysical and can produce many artificial disturbances (Emanuel *et al.*, 1994). If we plan to use RegCM2 for our future research, we may have to at least include the state-of-the-art physically-based Emanuel scheme in that model. Extensive comparison between several convective schemes may be needed.

Our land surface scheme in the models maybe one of the simplest. We used the dryness index as a surrogate of the actual vegetation type. This introduces some uncertainties in the magnitude of land surface perturbations. Clearly as the next step, we would like to include a more realistic land surface scheme such as the BATS (Biosphere-Atmosphere-Transfer-Scheme, Dickinson *et al.*, 1986). In fact, the RegCM2 we mentioned above has BATS as its land surface scheme.

We have also neglected the cloud-radiation feedback throughout this study. However, the cloud-radiation feedback can be very important (e.g., Stephens and Webster, 1979). The production and destruction of clouds is one of the least understood processes. This cloud-radiation feedback should be included for our future work.

We forced our model with the observed SSTs throughout this study. In other words, we ignored oceanic dynamical processes and the atmospheric feedback on SSTs. In reality, the West African monsoon and the tropical Atlantic Ocean SST are highly coupled, especially during the summer months (Mitchell and Wallace, 1992). In the tropical region, the solar insolation displays strong semiannual cycle. This sets up the observed bimodal rainfall time evolution near the tropical African coastal land (see Fig. 5.22). On the other hand, for the tropical Atlantic Ocean, the SST displays a dominant annual cycle (see Fig. 5.15). It has been generally accepted that the strong coupling between the atmosphere and the ocean plays a key role in creating

such an annual cycle (Chang and Philander, 1994; Liu and Xie, 1994). Ultimately, the simulation of West African monsoons should use coupled models.

Appendix A

Numerics

A.1   Grid Points

The staggered grid points are used, as shown in Figure A.1. Note that Ψ_{jk} is defined at •; U_{jk}, V_{jk} at o; W_{jk}, T_{jk}, Q_{jk} at □. The model grid increments are:

$$\Delta y = \frac{2a}{J},$$
$$\Delta z = \frac{ZMAX}{K},$$

where a is the earth radius; $ZMAX$ is the model top in vertical direction; J is the number of intervals in horizontal direction and K is the number of intervals in vertical direction. The horizontal grids are defined as:

$$\begin{cases} y_j = -a + (j-1)\Delta y & 1 \leq j \leq J+1, \\ \tilde{y}_j = -a + (j-\frac{1}{2})\Delta y & 1 \leq j \leq J. \end{cases}$$

The vertical grids are defined as:

$$
\begin{cases}
z_k = (k-1)\Delta z & 1 \le k \le K+1, \\
\tilde{z}_k = (k - \frac{1}{2}))\Delta z & 1 \le k \le K.
\end{cases}
$$

Finally stability parameters are:

$$
\begin{cases}
N_k^2 \equiv & N^2(z_k), \\
\tilde{N}_k^2 \equiv & N^2(\tilde{z}_k).
\end{cases}
$$
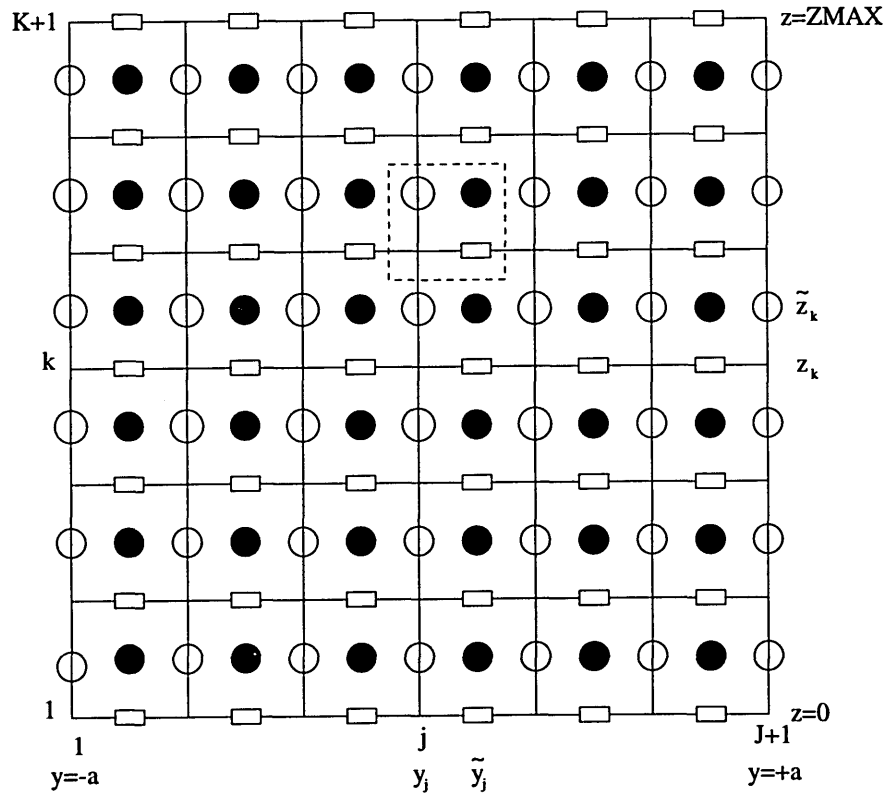
Figure A.1: The distribution of the model grid points.

A.2   Time Integration Scheme

Define a 3-point average in the time domain:

$$\hat{X} = \frac{X^{n+1} + 2X^n + X^{n-1}}{4}, \tag{A.1}$$

where $n-1$, n and $n+1$ denote three consecutive time levels. Then the time derivative can be expressed as:

$$\frac{\partial X}{\partial t} \simeq \frac{2\hat{X} - (X^n + X^{n-1})}{\Delta t}, \tag{A.2}$$

where Δt is time step. The time-finite-difference forms of momentum equations (2.1) and (2.2) can be written as:

$$\frac{2\hat{U}}{\Delta t} - f\hat{V} = AU + DU + FU + \frac{U^n + U^{n-1}}{\Delta t}, \tag{A.3}$$

$$\frac{2\hat{V}}{\Delta t} + f\hat{U} = AV + DV + FV - cos^2\phi\frac{\partial\hat{\Psi}}{\partial y} + \frac{V^n + V^{n-1}}{\Delta t}. \tag{A.4}$$

By defining

$$a = \frac{\Delta t}{2}(AU + DU + FU) + \frac{U^n + U^{n-1}}{2}, \tag{A.5}$$

$$b = \frac{\Delta t}{2}(AV + DV + FV) + \frac{V^n + V^{n-1}}{2}, \tag{A.6}$$

we have:

$$\hat{U} - \frac{f\Delta t}{2}\hat{V} = a, \tag{A.7}$$

$$\hat{V} + \frac{f\Delta t}{2}\hat{U} = b - cos^2\phi\frac{\Delta t}{2}\frac{\partial\hat{\Psi}}{\partial y}, \tag{A.8}$$

where a, b are evaluated explicitly from values at n and $n-1$ time levels. From the above two equations, we can solve $\hat{U}$ and $\hat{V}$:

$$\hat{U} = \left\{ a + \frac{f\Delta t}{2}b - \frac{f\Delta t^2}{4}cos^2\phi\frac{\partial\hat{\Psi}}{\partial y} \right\} \sigma, \qquad (A.9)$$

$$\hat{V} = \left\{ b - \frac{f\Delta t}{2}a - \frac{\Delta t}{2}cos^2\phi\frac{\partial\hat{\Psi}}{\partial y} \right\} \sigma, \qquad (A.10)$$

where $\sigma = (1 + \frac{f^2\Delta t^2}{4})^{-1}$. In addition, from the continuity equation (2.5),

$$M_1(\hat{W}) = -\frac{\partial\hat{V}}{\partial y} = -\frac{\partial}{\partial y}(\sigma q) + \frac{\Delta t}{2}\frac{\partial}{\partial y}\left(\sigma cos^2\phi\frac{\partial\hat{\Psi}}{\partial y} \right), \qquad (A.11)$$

where $q = b - \frac{f\Delta t}{2}a$. Furthermore, from the thermodynamic equation (2.3) and the hydrostatic equation (2.4),

$$\frac{\partial}{\partial t}\left(\frac{M_2(\Psi)}{N^2} \right) + \hat{W} = \frac{1}{N^2}(AT + DT + FT + Q_1), \qquad (A.12)$$

where $Q_1 = e^{-\frac{z}{2H}}\frac{R}{H}Q_d$. Eliminating $\hat{W}$ in above two equations, we have:

$$\mathcal{L}(\hat{\Psi}) + \frac{\Delta t^2}{4}\frac{\partial}{\partial y}\left(\sigma cos^2\phi\frac{\partial\hat{\Psi}}{\partial y} \right) = \frac{\Delta t}{2}M_1\left\{ \frac{1}{N^2}(AT + DT + FT + Q_1) \right\}$$
$$+ \frac{\Delta t}{2}\frac{\partial}{\partial y}(\sigma q) + \frac{1}{2}\mathcal{L}(\Psi^n + \Psi^{n-1}), \qquad (A.13)$$

where $\mathcal{L} = M_1\left\{ \frac{1}{N^2}M_2() \right\}$.

Equation (A.13) solves the $\hat{\Psi}$, given the values at $n-1$ and n time levels. Note that the right hand side of the equation is calculated explicitly. Once $\hat{\Psi}$ is known, $\hat{U}$ and $\hat{V}$ can be obtained from equations (A.9) and (A.10).

The equation for the determination of $\hat{Q}$ is given by:

$$\hat{Q} = \frac{\Delta t}{2}(AQ + e^{-\frac{z}{2H}}S_q + DQ + FQ) + \frac{Q^n + Q^{n-1}}{2}. \qquad (A.14)$$

After all the hat values of U, V, Ψ and Q are obtained, the values at $n+1$ time

level can be solved:

$$X^{n+1} = 4\hat{X} - 2X^n - X^{n-1}, \tag{A.15}$$

where X can be one of U, V, Ψ and Q. Temperature is given by hydrostatic equation (2.4).

In summary, this time integration scheme treats linear terms implicitly (except diffusion terms) while calculates nonlinear terms explicitly. Due to the implicit treatment of the linear terms (including Coriolis terms), the scheme allows longer time step up to 1 hour for dry model (Holton, 1976).

A.3 Spatial Finite Difference

Rewrite the $\hat{\Psi}$ equation (A.13),

$$- \mathcal{L}(\hat{\Psi}) - \frac{\Delta t^2}{4} \frac{\partial}{\partial y}\left(\sigma cos^2\phi \frac{\partial \hat{\Psi}}{\partial y}\right) = \frac{\Delta t}{2} M_1(G) - \frac{\Delta t}{2}\frac{\partial}{\partial y}(\sigma q), \tag{A.16}$$

where

$$G = -\frac{1}{N^2}\left\{AT + DT + Q_1 + FT + \frac{1}{\Delta t}(T^n + T^{n-1})\right\}.$$

The final finite difference equation is:

$$-\frac{\tilde{N}_k^2}{N_{k+1}^2}\hat{\Psi}_{j,k+1} - \frac{\tilde{N}_k^2}{N_k^2}\hat{\Psi}_{j,k} + \left\{\frac{\tilde{N}_k^2(e^-)^2}{N_{k+1}^2} + \frac{\tilde{N}_k^2(e^+)^2}{N_k^2} - A_{j,k} - C_{j,k}\right\}\hat{\Psi}_{j,k}$$

$$+ A_{j,k}\hat{\Psi}_{j-1,k} + C_{j,k}\hat{\Psi}_{j+1,k} = S_{j,k}, \tag{A.17}$$

where $e^+ = e^{\Delta z/4H}$; $e^- = e^{-\Delta z/4H}$; and

$$A_{j,k} = -\frac{\Delta z^2 \Delta t^2}{4\Delta y^2}\tilde{N}_k^2 \sigma_j cos^2 \phi_j, \qquad (A.18)$$

$$C_{j,k} = -\frac{\Delta z^2 \Delta t^2}{4\Delta y^2}\tilde{N}_k^2 \sigma_{j+1} cos^2 \phi_{j+1}, \qquad (A.19)$$

$$S_{j,k} = \frac{\Delta t \Delta z^2}{2}\tilde{N}_k^2 M_1(G)_{j,k} - \frac{\Delta t \Delta z^2}{2}\tilde{N}_k^2 \frac{\partial}{\partial y}(\sigma q)_{j,k}. \qquad (A.20)$$

Appendix B

The Role of Vegetation in the Dynamics of West African Monsoons — with Seasonal Cycle

We now use the model described in Chapter 5 to re-examine the impact of land surface transformations on the West African monsoon and rainfall. The model allows us to investigate the impact of various vegetation degradations on the West African rainfall under the solar insolation with full seasonal cycle. Recall that in Chapter 4, we confined ourselves on perpetual August solar forcing.

B.1 Experiment Set Up

The model details can be found in Section 5.3.1. We describe four experiments with different vegetation patterns. Figure B.1a shows the distribution of the dryness index for the control experiment, which is the same as shown in Figure 5.17. The three perturbation experiments include: the desertification from 15°N (Fig. B.1b); the tropical deforestation from 5°N to 15°N (Fig. B.1c); the desertification from 10°N (Fig. B.1d). The corresponding surface albedo and filed capacity are shown

in Figure B.2 and Figure B.3. Note that the dryness index patterns are similar to the experiments we described in Chapter 4 for the steady-state cases but not exactly the same. For each vegetation distribution, we integrate the model long enough (about 2 years) to achieve the statistically-equilibrated annual cycle. We then compare the output of the three perturbation experiments with that of the control experiment (see Section 5.3).

B.2   Results

We first show the summer (July-September average) rainfall meridional distribution of the four experiments corresponding to four vegetation patterns described in Figure B.1. This is shown in Figure B.4. We have demonstrated in Section 5.3 that the control experiment can reasonably simulate the observed summer rainfall distribution. Comparing to the steady-state experiments described in Chapter 4, the rainfall meridional distribution is more realistic. It is very clear that the essential features of atmospheric response to the imposed vegetation perturbations remain unchanged even though this model has quite a few modifications compared to the steady-state model we used in Chapter 4, such as the inclusion of the surface soil hydrology as well as a finite land surface heat capacity. Specifically, the desertification (from 15°N) has a minor effect on the whole regional rainfall over West Africa. The deforestation along the tropical coastal region does not cause the collapse of the monsoon but still causes substantial rainfall decrease over the West African region, including the Sahel region. The desertification (from 10°N) has the largest effect on the West African rainfall. In addition, the ITCZ is pushed southward from around 10-12°N to around 6°N. These experiments in general confirm the main results in Chapter 4, i.e., the West African monsoon and rainfall are sensitive to the location of the vegetation degradation. The location ITCZ is most sensitive to vegetation perturbation near the vicinity of the ITCZ in the control experiment. The tropical deforestation can be another source of
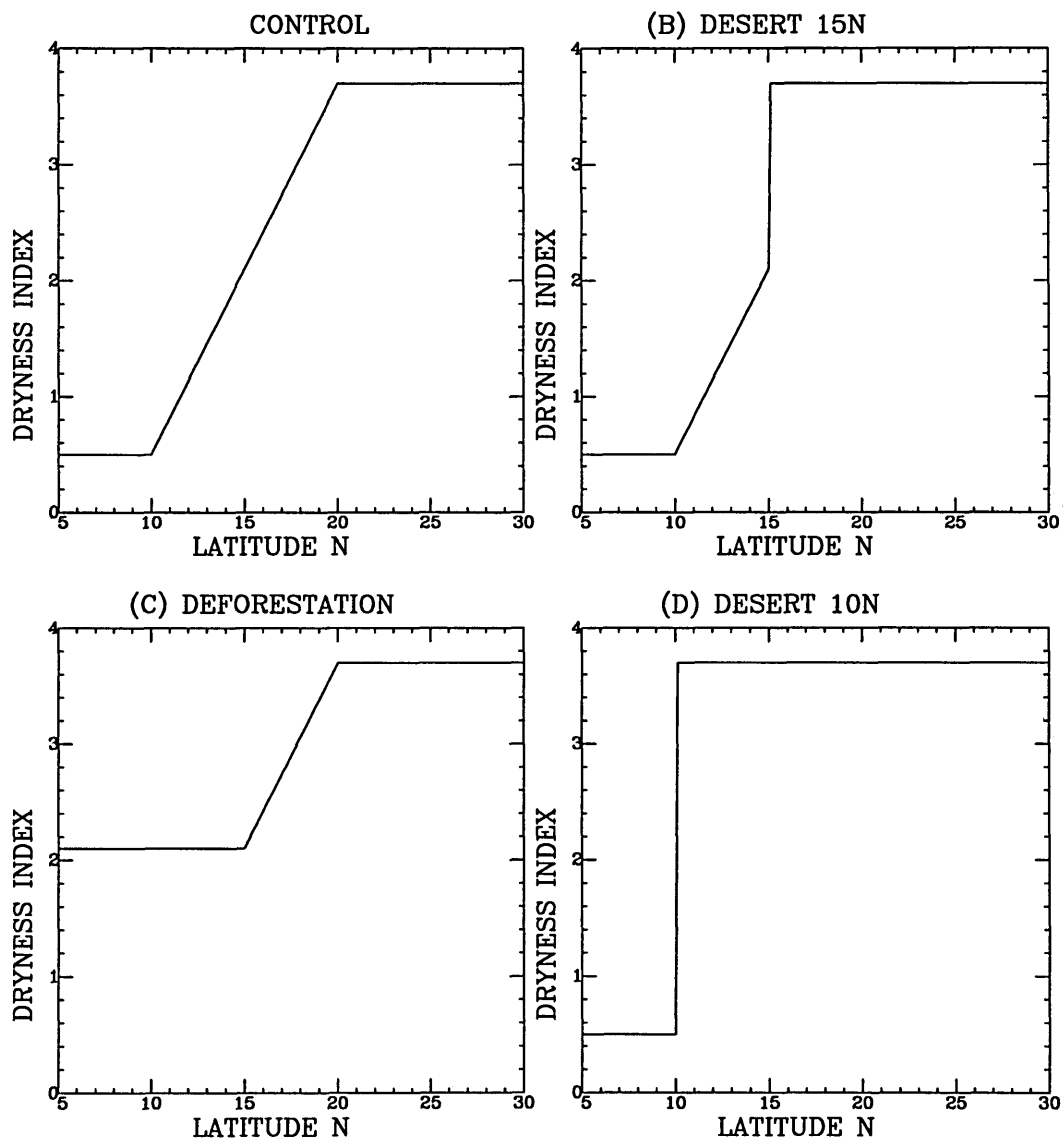
Figure B.1: The distribution of vegetation (described by the dryness index): (a) for the control experiment, (b) the desertification (from 15°N) experiment, (c) the deforestation experiment, and (d) the desertification (from 10°N) experiment.
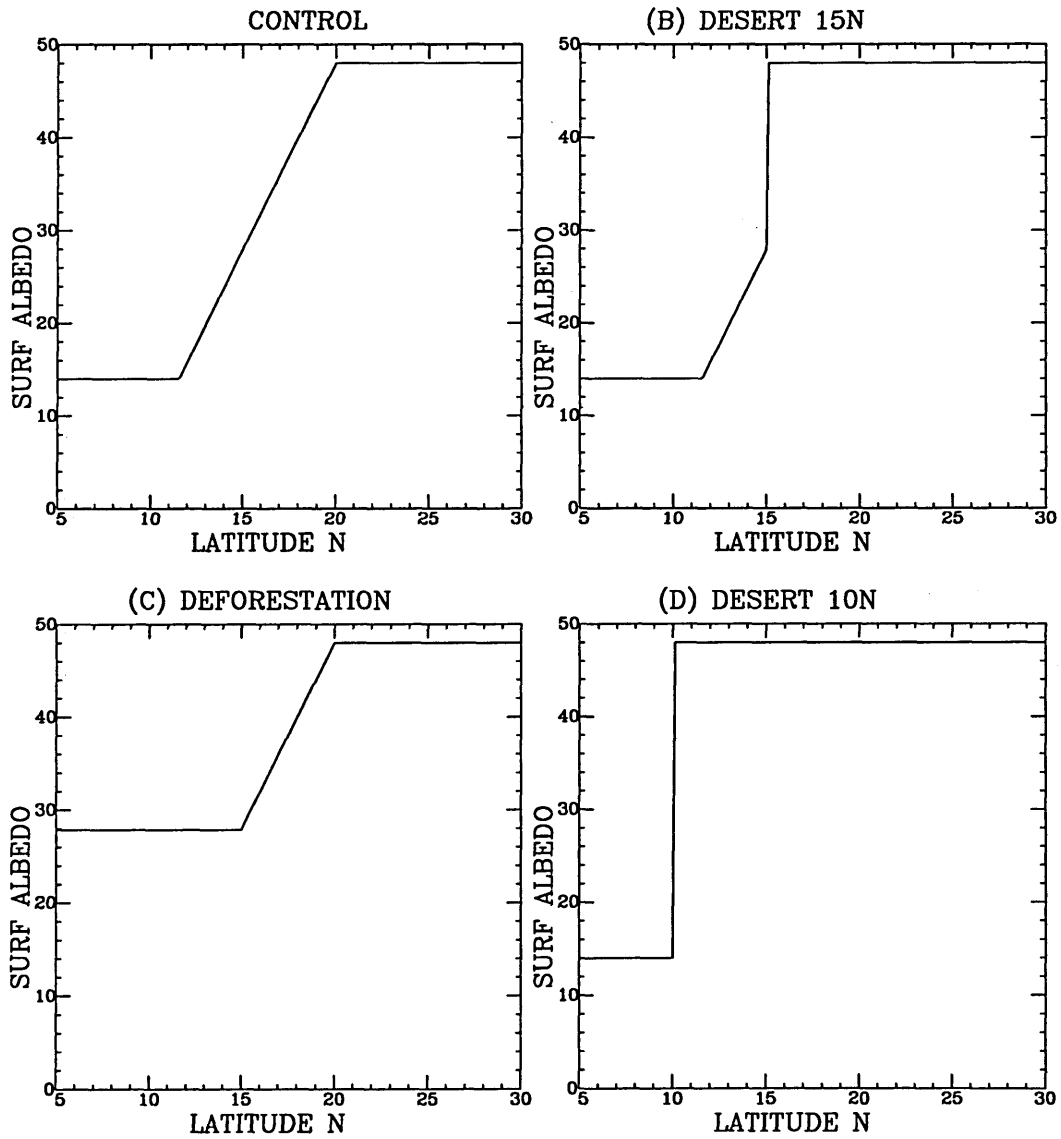
Figure B.2: The distribution of surface albedo in percentage: (a) for the control experiment, (b) the desertification (from 15°N) experiment, (c) the deforestation experiment, and (d) the desertification (from 10°N) experiment.
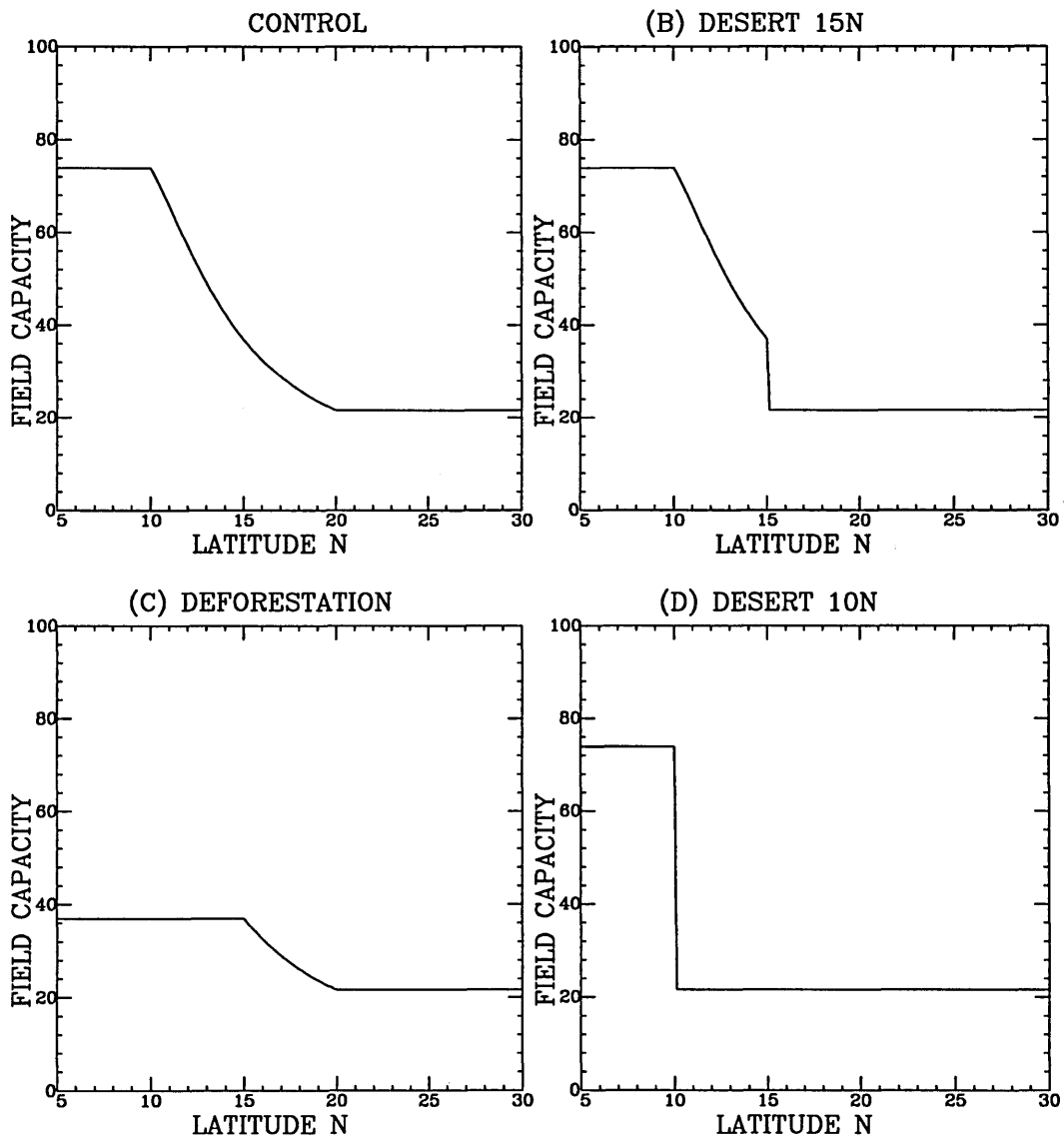
Figure B.3: The distribution of the field capacity (cm) (a) for the control experiment, (b) the desertification (from 15°N) experiment, (c) the deforestation experiment, and (d) the desertification (from 10°N) experiment.

West African drought besides sub-Saharan desertification.
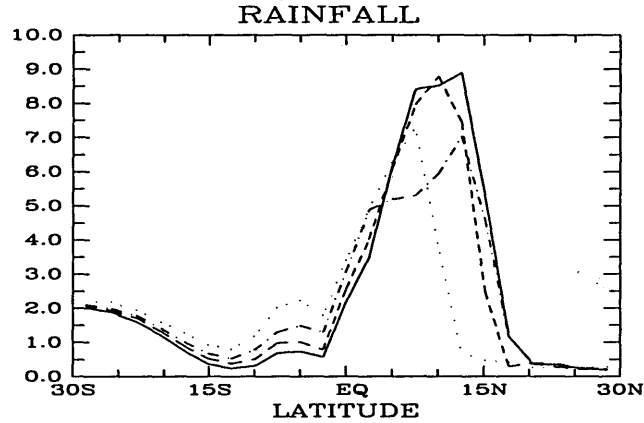
RAINFALL

Figure B.4: The latitudinal profiles of the summer (July-September average) rainfall for the control experiment (solid line), desertification (from 15°N) experiment (dashed line), deforestation experiment (dahed-dotted line) and desertification (from 10°N) experiment (dotted line). The units are mm/day.
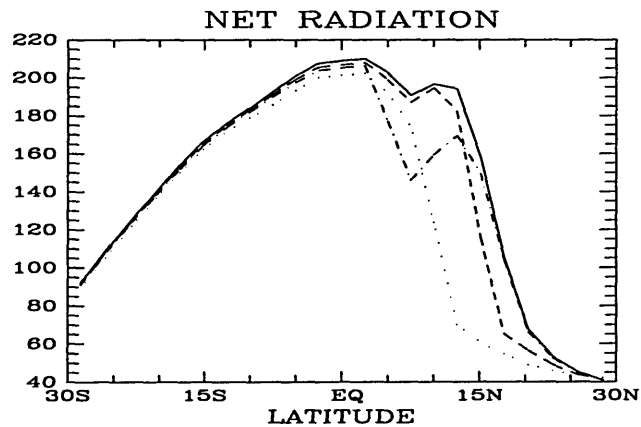
NET RADIATION

Figure B.5: The the same as Fig. B.4 but for the net surface radiation (Wm^{-2}).

The net surface radiation meridional distribution is also shown in Figure B.5. Similar to Chapter 4, the net surface radiation is reduced by the vegetation degradation to some extent. This introduces less total heat flux from the land surface and therefore less boundary layer entropy. As a result, the meridional gradient of

boundary layer entropy, which is critical for the strength of the monsoon circulation, is decreased. Among the three perturbation experiments, the desertification (from 10°N) induces the largest decrease of the net surface radiation. In the mean time, the deforestation also reduces the net radiation substantially. All these essentially verify the reasoning we gave in Chapter 4, i.e., changes in vegetative cover influence the net surface radiation, entropy flux from the surface, meridional distribution of boundary layer entropy and therefore the monsoon circulation and rainfall.

References

[1] Budyko, M.I., 1974: *Climate and Life*. International Geophysical Series, Volume 18, Academic Press, 508pp.

[2] Chang, P., and G.S. Philander, 1994: A coupled ocean-atmosphere instability of relevance to the seasonal cycle. *J. Atmos. Sci.*, **51**, 3627-3648.

[3] Charney, J.G., 1975: Dynamics of desert and drought in the Sahel. *Q. J. Roy. Meteorol. Soc.*, **101**, 193-202.

[4] Charney, J.G., Stone, P.H., Quirk, W.J., 1975: Drought in the Sahara: a biogeophysical feedback mechanism. *Science*, **187**, 434-435.

[5] Charney, J.G., Quirk, W.J., Chow, S.-H., Kornfield, J., 1977: A comparative study of the effects of albedo change on drought in semi-arid regions. *J. Atmos. Sci.*, **34**, 1366-1385.

[6] Chou, Ming-Dah, 1984: Broadband water vapor transmission functions for atmospheric IR flux computations. *J. Atmos. Sci.*, **41**, 1775-1778.

[7] Chou, Ming-Dah, D.P. Kratz and W. Ridgway, 1991: Infrared radiation parameterizations in numerical climate models. *J. Climate*, **4**, 424-437.

[8] Chou, Ming-Dah and L. Peng, 1983: A parameterization of the absorption in the $15\mu m$ CO_2 spectral region with application to climate sensitivity studies. *J. Atmos. Sci.*, **40**, 2183-2192.

[9] Cunnington, C. and P.R. Rowntree, 1986: Simulations of the Saharan atmosphere-dependence on moisture and albedo. *Q. J. Roy. Meteorol. Soc.*, **112**, 971-999.

[10] Darnell, W.L., W.F. Staylor, S.K. Gupta, N.A. Ritchey, and A.C. Wilber, 1995: A global long-term data set of shortwave and longwave radiation budget. *GEWEX News*, Vol. 4, No. 3, 1-8.

[11] Delworth, T.L., and S. Manabe, 1988: The influence of potential evaporation on the variabilities of simulated soil wetness and climate. *J. Climate*, **1**, 523-547.

[12] Dickinson, R.E., A. Henderson-Sellers, P.J. Kennedy, and M.F. Wilson, 1986: Biosphere-Atmosphere Transfer Scheme (BATS) for the NCAR Community Climate Model. *NCAR/TN-275+STR*, 68pp.

[13] Druyan, L.M., and S. Hastenrath, S., 1991: Modelling the differential impact of 1984 and 1950 sea-surface temperatures on Sahel rainfall. *Int. J. Climatol.*, **11**, 367-380.

[14] Eltahir, E.A.B., 1992: Drought frequency analysis of annual rainfall series in central and western Sudan. *Hydrological Sciences Journal*, **37**(3), 185-199.

[15] Eltahir, E.A.B., 1996: The role of vegetation in sustaining large scale atmospheric circulations in the tropics. *J. Geophys. Res.*, **101**, No. D2, 4255-4268.

[16] Eltahir, E.A.B., and C. Gong, 1995: Ocean-Atmosphere-Land Interactions and Rainfall in the Sahel. *EOS, Transactions of the American Geophysical Union*, Vol. 74, No. 46, F91.

[17] Eltahir, E.A.B., and C. Gong, 1996: Dynamics of wet and dry years in West Africa. *J. Climate*, **9**(5), 1030-1042.

[18] Emanuel, K.A., 1986: An air-sea interaction theory for tropical cyclones. Part I: Steady state maintenance. *J. Atmos. Sci.*, **43**, 585-604.

[19] Emanuel, K.A., 1991: A scheme for representing cumulus convection in large-scale models. *J. Atmos. Sci.*, **48**, 2313-2335.

[20] Emanuel, K.A., 1994: *Atmospheric Convection*. Oxford University Press, New York, 580pp.

[21] Emanuel, K.A., 1995: On thermally direct circulations in moist atmospheres. *J. Atmos. Sci.*, **52**, 1529-1534.

[22] Emanuel, K.A., J.D. Neelin, and C.S. Bretherton, 1994: On large-scale circulations in convecting atmospheres. *Q. J. Roy. Meteorol. Soc.*, **120**, 1111-1143.

[23] Farmer, G., and T.M.L. Wigley, 1985: *Climate Trends for Tropical Africa*. Research report for the Overseas Development Administration, Climate Research Unit, University of East Anglia, 136pp.

[24] Flohn, H., D. Henning and H.C. Korff, 1965: Studies on the water-vapour transport over Northern Africa. *Bonner Meteorol. Abhand.*, **6**.

[25] Folland, C.K., T.N. Palmer, and D.E. Parker, 1986: Sahel rainfall and worldwide sea temperatures, 1901-85. *Nature*, **320**, 602-607.

[26] Glantz, M.H., R.W. Katz, and N. Nicholls (Eds.), 1991: *Telecommunications Linking Worldwide Climate Anomalies*. Cambridge University Press, Cambridge, United Kingdom, 535pp.

[27] Gong, C. and E.A.B. Eltahir, 1996: Sources of moisture for rainfall in West Africa. Submitted to *Water Resources Research*.

[28] Giorgi, F., M.R. Marinucci, and G.T. Bates, 1993a: Development of a Second-Generation Regional Climate Model (RegCM2). Part I: boundary-layer and radiative transfer processes. *Mon. Wea. Rev.*, **121**, 2794-2813.

[29] Giorgi, F., M.R. Marinucci, and G.T. Bates, 1993b: Development of a Second-Generation Regional Climate Model (RegCM2). Part II: convective processes and assimilation of lateral boundary conditions. *Mon. Wea. Rev.*, **121**, 2814-2832.

[30] Gornitz, V., 1985: A survey of anthropogenic vegetation changes in West Africa during the last century. *Climatic Change*, **7**, 285-325.

[31] Gutman, G., G. Ohring, and J.H. Joseph, 1984: Interaction between the geobotanic state and climate: a suggested approach and a test with a zonal model. *J. Atmos. Sci.*, **41**, 2663-2678.

[32] Hadley, G., 1735: Concerning the cause of the general trade winds. *Phil. Trans., Roy. Soc. London*, **39**, 58-62.

[33] Hahn, D.G., and S. Manabe, 1975: The role of mountains in the South-Asian monsoon circulation. *J. Atmos. Sci.*, **32**, 1515-1541.

[34] Halley, E., 1686: An historical account of the trade winds and the monsoons, observable in the seas between and near the tropics, with an attempt to assign the physical cause of the said winds. *Phil. Trans., Roy. Soc. London*, **16**, 153-168.

[35] Held, I.M., and A.Y. Hou, 1980: Nonlinear axially symmetric circulations in a nearly inviscid atmosphere. *J. Atmos. Sci.*, **37**, 515-533.

[36] Hendon, H.H., and B. Liebmann, 1990: A composite study of onset of Australian summer monsoon, *J. Atmos. Sci.*, **47**, 2227-2240.

[37] Holton J.R., 1976: A semi-spectral numerical model for wave-mean flow interactions in the stratosphere: application to sudden stratospheric warming. *J. Atmos. Sci.*, **33**, 1639-1649.

[38] Holton, J.R., and W.M. Wehrbein, 1980: A numerical model of the zonal mean circulation of the middle atmosphere. *PAGEOPH*, **118**, 284-306.

[39] Huffman, G.J., R.F. Adler, B. Rudoff, U. Schneider, and P.R. Keehn, 1995: Global precipitation estimates based on a technique for combining satellite-based estimates, rain gauge analysis and NWP model precipitation estimates, *J. Climate*, 8(2), 1284-1295.

[40] Hulme, M., 1994: Century-scale series of regional rainfall anomalies in Africa, pp.964-973. In T.A. Boden, D.P. Kaiser, R.J. Sepanski, and F.W. Stoss (Eds.). *Trends (93): A Compendium of Data on Global Change.* ORNL/CDIAC-65. Carbon-Dioxide Information Analysis Center, Oak Ridge National Laboratory, Oak Ridge, Tenn., U.S.A.

[41] Joseph, J.H., W.J. Wiscombe and J.A. Weinman, 1976: The Delta-Eddington approximation for radiative flux transfer. *J. Atmos. Sci.*, 33, 2452-2459.

[42] Kidson, J.W., 1977: African rainfall and its relation to the upper air circulation. *Q. J. Roy. Meteorol. Soc.*, 103, 441-456.

[43] King, M.D., and Harshvardhan, 1985: Comments on "The parameterization of radiation for numerical weather prediction and climate models". *Mon. Wea. Rev.*, 113, 1832-1833.

[44] Kitoh, A., K. Yamazaki, and T. Takiota, 1988: Influence of soil moisture and surface albedo changes over African tropical rainforest on summer climate investigated with MRI-GCM-I. *J. of the Meteorol. Soc. of Japan*, 66(1), 65-85.

[45] Krishnamurti, T.N., 1971: Tropical east-west circulations during the northern summer. *J. Atmos. Sci.*, 28, 1342-1347.

[46] Krishnamurti, T.N., 1985: Summer monsoon experiment — a review. *Mon. Wea. Rev.*, 113, 1590-1626.

[47] Krishnamurti, T.N., 1987: Monsoon models, pp467-522. In *Monsoons*, edited by Fein, J.S., and Stephens, P.L., John Wiley & Sons, Inc., 632pp.

[48] Krishnamurti, T.N. and Y. Ramanathan, 1982: Sensitivity of the monsoon onset to differential heating. *J. Atmos. Sci.*, **39**, 1290-1306.

[49] Lacis, A.A., and J.E. Hansen, 1974: A parameterization for the absorption of solar radiation in the Earth's atmosphere. *J. Atmos. Sci.*, **31**, 118-133.

[50] Lamb, P.J., 1978a: Case studies of tropical Atlantic surface circulation patterns during recent sub-Saharan weather anomalies: 1967 and 1958. *Mon. Wea. Rev.*, **106**, 482-491.

[51] Lamb, P.J., 1978b: Large-scale Tropical Atlantic surface circulations patterns associated with sub-Saharan weather anomalies. *Tellus*, **30**, 240-251.

[52] Lamb, P.J., 1983: West African water vapor variations between recent contrasting Subsaharan rainy seasons. *Tellus*, **35A**, 198-212.

[53] Lamb, P.J., and R.A. Peppler, 1991: West Africa. In *Teleconnections Linking Worldwide Climate Anomalies*. Glantz, M.H., R.W. Katz, and N. Nicholls (Eds.). Cambridge University Press, Cambridge, UK., 535pp.

[54] Lamb, P.J., and R.A. Peppler, 1992: Further case studies of Tropical Atlantic surface atmospheric and oceanic patterns associated with sub-Saharan drought. *J. Climate*, **5**(5), 476-488.

[55] Lindzen, R.S., and A.Y. Hou, 1988: Hadley circulations for zonally averaged heating centered off the equator. *J. Atmos. Sci.*, **45**, 2416-2427.

[56] Liu, Z., and S. Xie, 1994: Equatoward propagation of coupled air-sea disturbances with application to the annual cycle of the Eastern Tropical Pacific. *J. Atmos. Sci.*, **51**, 3807-3822.

[57] Lough, J.M., 1986: Tropical sea surface temperature and rainfall variation in sub-Saharan Africa. *Mon. Wea. Rev.*, **114**, 561-570.

[58] MaClatchey, R.A., R.W. Fenn, J.E.A. Selby, F.E. Volz, and J.S. Garing, 1972: Optical properties of the atmosphere. Air Force Cambridge Research Laboratories. Environmental Research Papers, No. 411.

[59] Manabe, S., 1969: Climate and the ocean circulation: I. The atmospheric circulation and the hydrology of the earth's surface. *Mon. Wea. Rev.*, **97**, 739-774.

[60] Mitchell, T.P., and J.M. Wallace, 1992: The annual cycle in equatorial convection and sea surface temperature. *J. Climate*, **5**, 1140-1156.

[61] Murakami, T., R.V. Godbole, and R.R. Kelkar, 1970: Numerical experiment of the monsoon along 80°E longitude, pp39-51. In *Proceedings of the Conference on the Summer Monsoon of Southeast Asia*, Navy Weather Research Facility, Norfolk.

[62] Murakami, T., 1987: Orography and monsoons, pp331-364. In *Monsoons*, edited by Fein, J.S., and Stephens, P.L., John Wiley & Sons, Inc., 632pp.

[63] Myers, N., 1991: Tropical forests: present status and future outlook. *Climatic Change*, **19**, 3-32.

[64] Newell, R.E., J.W. Kidson, D.G. Vincent, and G.J. Boer, 1972a: *The General Circulation of the Tropical Atmosphere*, Volume 1. The MIT Press, Cambridge, Massachusetts, 258pp.

[65] Newell, R.E., J.W. Kidson, D.G. Vincent, and G.J. Boer, 1972b: *The General Circulation of the Tropical Atmosphere*, Volume 2. The MIT Press, Cambridge, Massachusetts, 371pp.

[66] Newell, R.E., and J.W. Kidson, 1984: African mean wind changes between Sahelian wet and dry periods. *J. Climatology*, **4**, 27-33.

[67] Nicholson, S.E., 1988: Land surface atmosphere interaction. *Progress in Physical Geography*, **12**, 36-65.

[68] Nicholson, S.E., 1994: Century-scale series of standardized annual departures of African rainfall, pp.952-962. In T.A. Boden, D.P. Kaiser, R.J. Sepanski, and F.W. Stoss (Eds.). *Trends (93): A Compendium of Data on Global Change.* ORNL/CDIAC-65. Carbon-Dioxide Information Analysis Center, Oak Ridge National Laboratory, Oak Ridge, Tenn., U.S.A.

[69] Nicholson, S.E., and D. Entekhabi, 1986: The quasi-periodic behaviour of rainfall variability in Africa and its relationship to the southern oscillation. *Arch. Meteorol. Geophys. Bioclim.*, Ser. A, **34**, 311-348.

[70] Nicholson, S.E., and I. Palao, 1993: A reevaluation of rainfall variability in the Sahel. Part I. Characteristics of rainfall fluctuations. *Int. J. Climatol.*, **13**, 371-389.

[71] Nicholson, S.E., M.B. Ba, and J.Y. Kim, 1996: Rainfall in the Sahel during 1994. *J. Climate*, **9**(7), 1673-1676.

[72] Owen, J.A., and C.K. Folland, 1988: Modelling the influence of sea surface temperatures on tropical rainfall. In *Recent Climate Change — a Regional Approach.* S. Gregory (Eds.). Belhaven Press, London, 326pp.

[73] Owen, J.A., and M.N. Ward, 1989: Forecasting Sahel rainfall. *Weather*, **44**, 57-64.

[74] Parker, D.E., C.K. Folland, and M.N. Ward, 1988: Sea-surface temperature anomaly patterns and prediction of seasonal rainfall in the Sahel region of Africa. In *Recent Climate Change — a Regional Approach.* S. Gregory (Eds.). Belhaven Press, London, 326pp.

[75] Palmer, T.N., 1986: Influence of the Atlantic, Pacific and Indian Oceans on Sahel rainfall. *Nature*, **322**, 251-253.

[76] Palmer, T.N., C. Brankovic, P. Viterbo, and M.J. Miller, 1992: Modelling inter-annual variations of summer monsoons. *J. Climate*, **5**, 399-417.

[77] Plumb, R.A. and A.Y. Hou, 1992: The response of a zonally symmetric atmosphere to subtropical thermal forcing: threshold behavior. *J. Atmos. Sci.*, **49**, 1790-1799.

[78] Powell, D.P., and C. Blondin, 1990: The influence of soil wetness distribution on short range rainfall forecasting in the West African Sahel. *Q. J. Roy. Meteorol. Soc.*, **116**, 1471-1485.

[79] Ramage, C.S., 1971: *Monsoon Meteorology*. New York, Academic Press, 296pp.

[80] Rasmusson, E.M., 1972: Seasonal variation of the tropical humidity parameters, Chapter 5 of Newell *et al.* (1972).

[81] Reynolds, R.W., 1988: A real-time global sea surface temperature analysis. *J. Climate*, **1**, 75-86.

[82] Reynolds, R.W. and D.C. Marsico, 1993: An improved real-time global sea surface temperature analysis. *J. Climate*, **6**, 114-119.

[83] Reynolds, R.W. and T.M. Smith, 1994: Improved global sea surface temperature analyses. *J. Climate*, **7**, 929-948.

[84] Rodgers, C.D., 1968: Some extension and applications of the new random model for molecular band transmission. *Q. J. Roy. Meteorol. Soc.*, **94**, 99-102.

[85] Rodriguez-Iturbe, I., D. Entekhabi and R.L. Bras, 1991: Nonlinear dynamics of soil moisture at climate scales: 1. stochastic analysis. *Water Resources Research*, **27**, 1899-1906.

[86] Rowell, D.P., C.K. Folland, K. Maskell, J.A. Owen, and M.N. Ward, 1992: Modelling the influence of global sea surface temperatures on the variability and and predictability of seasonal Sahel rainfall. *Geophys. Res. Lett.*, **19**, 905-908.

[87] Rowell, D.P., C.K. Folland, K. Maskell, and M.N. Ward, 1995: Variability of summer rainfall over tropical north Africa (1906-92): Observations and modelling. *Q. J. Roy. Meteorol. Soc.*, **121**, 669-704.

[88] Schneider, E.K., 1983: Martian great dust storms: Interpretive axially symmetric models. *ICARUS*, **55**, 302-331.

[89] Schneider, E.K., 1987: A simplified model of the modified Haldey circulation. *J. Atmos. Sci.*, **44**, 3311-3328.

[90] Schneider, E.K., and R.S. Lindzen, 1977: Axially symmetric steady-state models of the basic state for instability and climate studies. Part I: Linearized calculations. *J. Atmos. Sci.*, **34**, 263-279.

[91] Semazzi, F.H.M., V. Mehta, and Y.C. Sud, 1988: An investigation of the relationship between sub-Saharan rainfall and global sea surface temperatures. *Atmos.-Ocean*, **26**, 118-138.

[92] Srinivasan, J., S. Gadgil, and P.J. Webster, 1993: Meridional propagation of large-scale monsoon convective zones. *Meteorol. Atmos. Phys.*, **52**, 15-35.

[93] Stephens, G.L., and P.J. Webster, 1979: Sensitivity of radiative forcing to variable cloud and moisture. *J. Atmos. Sci.*, **36**, 1542-1555.

[94] Sud, Y.C., and M.J. Fennessy, 1984: Influence of evaporation in semi-arid regions on the July circulation: A numerical study. *J. Climatology*, **4**, 383-398.

[95] Sud, Y.C., and A. Molod, 1988: A GCM simulation study of the influence of Saharan evapotranspiration and surface albedo anomalies on July circulation and rainfall. *Mon. Wea. Rev.*, **116**, 2388-2400.

[96] Walker, J., and P.R. Rowntree, 1977: The effect of soil moisture on circulation and rainfall in a tropical model. *Q. J. Roy. Meteorol. Soc.*, **103**, 29-46.

[97] Washington, W.M., and S.M. Daggapaty, 1975: Numerical simulation with the NCAR general circulation model of the mean conditions during the Asian-African summer monsoon. *Mon. Wea. Rev.*, **103**, 105-114.

[98] Webster, P.J., 1983: Mechanisms of monsoon low-frequency variability: surface hydrological effects. *J. Atmos. Sci.*, **40**, 2110-2124.

[99] Webster, P.J., 1987: The elementary monsoon, pp3-32. In *Monsoons*, edited by Fein, J.S., and Stephens, P.L., John Wiley & Sons, Inc., 632pp.

[100] Webster, P.J., and L.C. Chou, 1980a: Seasonal structure of a simple monsoon system. *J. Atmos. Sci.*, **37**, 354-367.

[101] Webster, P.J., and L.C. Chou, 1980b: Low-frequency transitions of a simple monsoon system. *J. Atmos. Sci.*, **37**, 368-382.

[102] Xue, Y., K.N. Liou, and A. Kasahara, 1990: Investigation of biogeophysical feedback on the African climate using a two-dimensional model, *J. Climate*, **3**, 337-352.

[103] Xue, Y., and J. Shukla, 1993: The influence of land surface properties on Sahel climate, Part I: Desertification. *J. Climate*, **6**, 2232-2245.

[104] Yeh, T.-C., S.H. Dao, and M.T. Li, 1959: The abrupt change change of circulation over the Northern Hemisphere during June and October, pp249-267. In *The Atmosphere and the Sea in Motions*, Rossby Memorial Volume, New York, The Rockefeller Institute Press.

[105] Yeh, T.-C., R.T. Wetherald, and S. Manabe, 1984: The effect of soil moisture on the short-term climate and hydrology change — a numerical experiment. *Mon. Wea. Rev.*, **112**, 474-490.